Characterization and Optimization of Composite/Metallic

Adhesively Bonded Joints Subjected to Thermal Fatigue

by

Mbarka Mohamed

Submitted in partial fulfilment of the requirements
for the degree of Doctor of Philosophy

Dalhousie University

Halifax, Nova Scotia

March 2019

DEDICATION

In loving memories of my father, Mahmud and my youngest sister, Hana

Loved Always, Sadly Missed

Table of Contents

List of Tables

List of Figures

Abstract

Adhesively bonded joints (ABJs) are widely used to mate two or more structural elements. Therefore, to ensure their durability and safe performance, such joints must be carefully designed, especially when they are subjected to harsh environmental conditions. Traditionally, ABJs have been designed using a variety of stress-based approaches. In recent years, however, the use of fracture mechanics (FM) has become increasingly popular for design and analysis of bonded joints. FM offers several approaches for design and analysis of ABJs made of similar or dissimilar materials, and those used in repair of damaged structural components.

A summary of an investigation aimed to characterize the response of composite/metallic bonded joints subjected to thermal fatigue by a FM approach is presented. Specifically, the main goal is to quantify the degradation mechanism of such joints by examining the adhesive/adherend interface cracking mechanism. Therefore, a coupled finite element/experimental analysis framework is designed to explore the degradation and failure of the joints. The parameters that actually govern the performance of joints that comprise of fiber-reinforced laminated composite adherends were explored. In addition, an optimization technique has been proposed for improving the longevity and performance of such joints, especially when exposed to cyclic thermal loads. Finally, the use of a relatively inexpensive nanomaterial for enhancing the performance of ABJs is explored and presented.

List of Abbreviations and Symbols Used

ABJ	Adhesively bonded joint
BK	Benzeggagh-Kenane damage evolution criterion
CBT	Corrected beam theory
CBBM	Compliance based beam method
CDM	Continuum damage mechanics
CIM	Coefficient of mutual influence
CFRP	Carbon fiber reinforced polymer
CPU	Computer processing unit
CZM	Cohesive zone model
CCZM	Cyclic cohesive zone modeling
D	Damage variable
DAQ	Data-acquisition system
DCB	Double cantilever beam
ECM	Experimental compliance method
ENF	End notched flexure
FEA	Finite element analysis
FM	Fracture mechanics
FRP	Fiber reinforced polymer
FPZ	Fracture process zone
GFRP	Glass fiber reinforced polymer
GNPs	Graphene nanoplatelets
LEFM	Linear elastic fracture mechanics
MBT	Modified beam theory method
MCC	Modified compliance calibration method
PR	Poisson's ratio
SBT	Simple beam theory
SDEG	Scalar stiffness degradation damage index
SDV	Scalar degradation due to thermal fatigue
SEM	Scanning electron microscopy
SLB	Single leg bending
SOM	Stereo optical microscopy
UD	Unidirectional
UTS	Ultimate tensile strength
US	Ultimate strain
a	Crack length
a_0	Initial crack length
A_{ij}	In-plane stiffness matrices
B	Width of the specimen
B_{ij}	Axial bending stiffness matrices
D	Scalar damage variable ranging between 0 and 1
$D(t)$	Total damage at time t
D_{cyc}	Progressive cyclic degradation of the interface damage parameter

D_{ij}	Bending stiffness matrices
D_m	Mechanical damage
D_{th}	Thermal fatigue damage
D_{tot}	Total damage
E	Modulus of elasticity of the adherends
E_a	Modulus of elasticity of the adhesive
E_f	Modulus of elasticity of the strap
E_s	Flexural modulus of elasticity
E_1	Modulus of elasticity of the adherend in the X-direction
E_2	Modulus of elasticity of the adherend in the Y-direction
E_3	Modulus of elasticity of the adherend in the Z-direction
I	Identity matrix
F	Correction factor for large displacements
G	Strain energy release rate
G_c	Critical strain energy release rate
G_{Ic}	Critical strain energy release rate in mode-I
G_{IIc}	Critical strain energy release rate in mode-II
G_T	Fracture Toughness for lap strap joint
G_{12}	In-plane shear modulus
G_{23}, G_{13}	Through-thickness shear moduli
h	Thickness of the adherend
K	Crack tip stress intensity factor
$\bar{Q}$	Stiffness matrix of each ply
L_{CZ}	Length of the cohesive zone
l_e	Element dimension in the direction of crack propagation
l_0	Size of the elastic zone ahead of the cohesive zone
L'	Width of one-half of the loading block
M	multiplier
N	Correction factor for large displacements
N_e	The minimum number of elements required for CZM
n	Number of thermal cycles; also, the exponent parameter in BK equation
P	Applied load
r	Distance measured from crack tip
S	Interface strength (peak tractions in strength)
t	Time
t_a	Thickness of the adhesive layer
t_l	Thickness of the lap adherend
t_s	Thickness of the strap adherend
T	Temperature
T_g	Glass transition temperature
w	Specimen width
Z_k	Distance measured from bottom of each play to the mid-plane
Z_{k-1}	Distance measured from top of each play to the mid-plane
υ	Poisson's ratio

$\sigma_{max,0}$	Initial maximum stress in the cohesive zone (when D=0)
σ	Stress; also, current cohesive stress state.
ε	Strain
δ	Load point deflection (i.e., relative displacement of the interface)
δ_0	Damage initiation coefficient
β	Mode mixity coefficient
υ_{12}	In-plane Poisson's ratios
$\upsilon_{23}, \upsilon_{13}$	Out-of-plane Poisson's ratios
υ_{xy}	Poisson's ratios
τ_0	Peak traction/stress
α	Thermal expansion coefficient
Δ	Correction value in (CBT) equation
ξ	fitting parameter
γ_{xy}	In-plane shear strain
$\eta_{xy(x)}$	Coefficient of mutual influence

Acknowledgement

I would like to sincerely thank my supervisor, Professor Farid Taheri. This research would not have been possible without his continued support, supervision and encouragement during the whole period of my PhD program; I want to thank him for his wisdom, care, patience, understanding, constructive suggestions and positive attitude during the difficult situations, which in turn made my research achievements possible. I am also thankful to him for all the time he expended to review the manuscript of my thesis critically, and his dedication to my success. Without him, the journey would not have been as enjoyable as it was.

I would like to thank Dr. Rajamohan Ganesan of Concordia University, Dr. Fadi Oudah and Dr. Kevin Plucknett of Dalhousie University for their role in my supervisory committee, and for reviewing my PhD thesis and providing constructive technical feedback.

I would also like to thank my colleagues, friends and the department's staff for their generous help and assistance. Special thanks go to our lab technicians: Brian Kennedy, Jesse Kean and Blair Nickerson for their assistance and technical support throughout my experimental works. Also, I would like to thank Dr. G. Mazzanti and O. AL Qatami for their help in operating the DSC instrument. My special thanks also go to Professor M. A. White and M. Johnson for their helpful assistance in carrying out the Raman experiments, interpreting the results and helpful relevant discussions.

My thanks also go to all my friends, colleagues and current and ex-officemates at Dalhousie University, Drs. Ramadan Ahmed, Shiva Eslami, Shahin Shadlou, Morteza Mehrzadi, Babak Ahmadi, Meisam Asgari, Zohreh Asaee, and misters Ibtesam Ahmed, Davide De Cicco, and Babak Soltannia for their support, friendship and understanding.

Last, but not least, my special appreciation goes to the Ministry of Higher Education and Scientific Research of government of Libya for a fully-funded scholarship, without which I would not be able to pursue my studies in Canada. Also, I would also like to thank my colleagues in the National

Chapter 1: Introduction

1.1 Adhesively Bonded Joints

Adhesively bonded joints (ABJs) are widely used to mate two or more structural elements. To ensure durability and safe performance of ABJs, the joints must be carefully designed and assembled, especially when they are used in applications that experience harsh environmental loading conditions. In this dissertation, the term 'adhesive' refers to a material that when applied to surfaces of two mating materials, would hold them together and resists their separation by means of surface tension. Such a material may be a filler material, a nonmetallic, or a polymer. The materials being joined are commonly referred to as substrates or adherends, and the force at the bond line between the adhesive and the substrate is referred to as 'adhesion'. The strength of this interface is called the interface strength, while 'cohesive strength' is a commonly used terminology that refers to the internal strength of the adhesive. ABJs can be in one of many configurations as shown in Figure 1-1 (Adams, 2005; da Silva et al., 2011; He, 2011; Wahab, 2015).
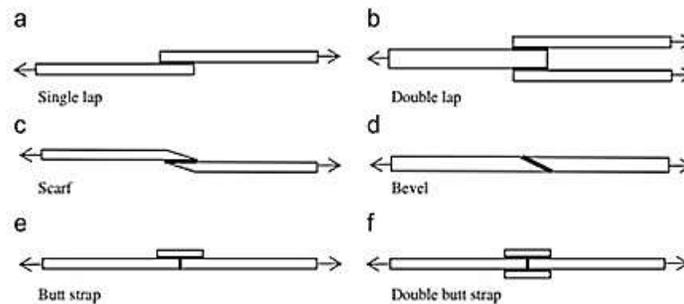
Figure 1-1 Configuration of commonly used adhesively bonded joints (He, 2011)

The lap joint is the most common joint configuration, as it is most practical means for mating thin materials, thus, it is the most studied joint. There are various external factors that cause strength reduction in ABJs. Examples would be fatigue caused by cyclic mechanical loads, degradation of the adhesive/adherend interface caused by exposure to elevated or cryogenic temperatures, humidity, water, and other chemicals and liquids. In addition, internal stresses caused by adhesive

shrinkage and mismatch in the coefficients of thermal expansion of adherends and adhesives could also affect the strength of ABJs significantly (Broughton and Mera, 1997; Dillard, 2010). While different failure mechanisms could be developed in ABJs as a result of the stated anomalies, they can essentially be categorized into three different modes (see Figure 1-2), as follows:

1. Structural failure: characterized by the internal failure of adherend materials in locations near the joint overlap. Common examples would be tearing of fiber-reinforced polymer composite (FRP) adherends and their potential delamination.

2. Interfacial failure: characterized by separation of one of the substrates from the adhesive layer. This type failure can arise from a faulty interface primarily caused due to poor surface preparation.

3. Cohesive failure: characterized by internal failure within the adhesive layer, mainly caused when the cohesive strength of the adhesive is exceeded.
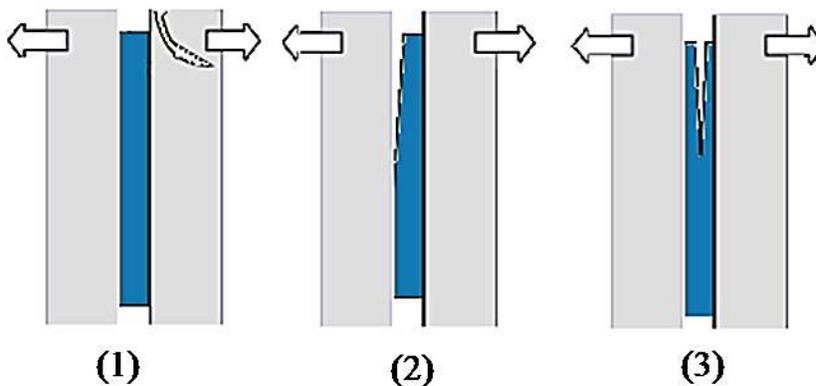
Figure 1-2 Possible failure modes in adhesively bonded joints
(www.theadhesivesexpert.com , 2018)

The adhesives' market share is approximately 21 billion dollars within the global industry, serving many applications and end markets (Dunn, 2003). In other words, adhesives occupy approximately 6% of the global fastening market as illustrated pictorially in Figure 1-3. Moreover, new bonding methodologies and advancements in polymer development are continually increasing the growth of adhesives in the global market (www.DPNA International, 2017).

Figure 1-3 Global picture of assembly and fastening market (www.DPNA International, 2017)

1.2 Thermal Fatigue

The change of volume due to change in temperature is called thermal expansion (Carden, 1963). If a solid is restrained such that it cannot expand or contract freely, then temperature change would give rise to thermal stresses. The term 'thermal fatigue' is applied to failures caused by cyclic thermal stresses. Halford and Manson (1976), and Spera (1976) defined the thermal fatigue as the gradual deterioration and eventual cracking of a material instigated by alternate heating and cooling during which free thermal expansion/contraction is partially or completely constrained. Constraint of thermal expansion causes thermal stresses, which in turn may eventually initiate and propagate fatigue cracks. Thermal fatigue may be classified under the more general heading of low-cycle fatigue, because thermal fatigue usually becomes apparent in less than 50,000 cycles (typically less than 1000 cycles are considered as low cycle thermal fatigue and more than 1000 cycles are high-cycle thermal fatigue). In addition, thermal fatigue usually causes significant inelastic strains. Thus, Spera (1976) suggested the use of two terminologies for defining this category of low-cycle fatigue; (i) thermal fatigue, if the fatigue causing temperature is not constant with time; and (ii) isothermal fatigue, otherwise. In other words, thermal fatigue might be caused by starting and stopping of the movement of a machinery piece used in an equipment operated at a high temperature, while isothermal fatigue might arise as a consequence of vibration during steady-state operation of mechanical systems.

3

In a thermal fatigue analysis, the most crucial material property is the coefficient of thermal expansion; therefore, significant problems can be created when bonded materials undergo thermal cycles. The mismatch of the coefficients of thermal expansions of the mating materials could cause thermal stresses. In an isotropic material, the principal mechanical properties that influence the magnitude of the stresses are the elastic constants (i.e., modulus of elasticity E and Poisson's ratio υ), the temperature and time- dependent flow strength (in a cyclic state), material's ductility and fracture toughness. Since it is desirable to keep the thermal stresses low, thus a material with a low modulus of elasticity would be desirable, which may not be a suitable choice in a given practical situation. If yielding occurs during a thermal cycling event, then it is desirable to select a material with high yield strength so to minimize the inelastic component of the stress (Humfeld Jr, 1997).

Fatigue fracture is one of the major causes of failure of engineering components and structures; therefore, its investigation is warranted. It is caused by the growth of initial flaws to cracks and their eventual growth under a cyclic loading. Harsh environments such as high temperatures can increase the propagation rate. Flaws, cracks or micro-structural features are unavoidably inherent in most joints' interfaces. The situation becomes further exacerbated when the temperature of the solid fluctuates repeatedly. Thermal cycling, as a source of damage in material systems, has also been reported as a significant cause of failure in a wide variety of structural components and configurations (e.g., in solder joints, thermal barrier films, ABJs, bridge decks, large storage tanks, and oil and gas pipelines).

Environmental factors, such as temperature and moisture oscillations, are known to impose degrading effects on the mechanical properties and performance of ABJs, Viana et al., (2017), Ray and Rathore (2014). The challenge becomes even more significant when a joint is subjected to combined effects of environment and mechanical loadings. Marques et al. (2015) have provided a comprehensive review of various mechanisms and factors affecting the performance of adhesives under extreme temperatures. Mechanisms such as shrinkage and thermal expansion, adhesive properties, and design techniques leading to optimized joints are some of the topics comprehensively discussed in the mentioned reference.

1.3 Motivations, Objectives and Contributions

1.3.1 Motivations

One of the critical considerations concerning is to investigate the use of ABJs in harsh environmental conditions, especially their long-term performance and durability under cyclic thermal loading. Harsh loading states could cause degradation of the stiffness and strength of adherends and adhesives. Less attention has been paid in the literature on the effect of thermal loading fluctuations on degradation and durability of ABJs. Also, the majority of the relevant research has considered ABJs subjected to monotonic loads, while in many practical applications, mechanical fatigue and thermal fatigue are the prevalent loading states. Therefore, exploring reliable methodologies that provide accurate damage assessment of ABJs, thus, enabling one to predict the durability of ABJs under such conditions is of paramount importance.

1.3.2 Objectives

The objectives of this research are trifold.

i.   To investigate the performance of ABJs mating fiber-reinforced polymer composites to metallic adherends, subjected to cyclic thermal loading by conducting appropriate experiments.

ii. To establish a robust computational framework, using the finite element method, by which the performance of ABJs subject to both cyclic thermal and the subsequent mechanical loads could be predicted with a reasonable accuracy.

iii. To optimize performance and durability of ABJs by inclusion of nanoparticles, as well as incorporation of a design optimization procedure by which a joint's thermal mismatch is minimized, thus minimizing the magnitude of dominant stresses that cause failure of ABJs.

1.3.3 Contributions

In this subsection, the author's specific contributions made to the current state-of-the-art on the influence of thermal fatigue on the performance of ABJs mating dissimilar materials are outlined, thereby fulfilling the objectives of this thesis project.

i.   An experimental investigation is conducted to characterize the response of a widely used neat epoxy and ABJs made using the same epoxy, subject to cyclic thermal loading and the subsequent mechanical loading.

ii.   A robust finite element analysis (FEA) framework, using the cohesive zone methodology is developed by which the fracture response of the ABJs is traced. The results produced by the proposed FEA methodology are compared against the experimental results, thus establishing the integrity of the proposed methodology. The numerical approach will be demonstrated to be a robust approach capable of simulating ABJs' response during the applied thermal cycling phase, as well as the subsequent applied mechanical loading, within a single analysis. The predicted results are accurate, and the approach is computer processing unit (CPU) efficient.

iii.   A strategy is introduced for improving the performance of the ABJs under the thermal fatigue and subsequent mechanical loading by reducing the stresses within the adhesive and interfaces of ABJs. The parameters that are hypothesized to be responsible for aggravating the peel and shear stresses in the bonded joints are identified, and their effects are assessed by a coupled experimental and numerical approach. A simple remedy is introduced by which the peel and shear stresses are alleviated significantly.

iv.   Finally, an approach used by our research group to enhance the performance of ABJs under mechanical loading is used in this study to evaluate its utility in improving the performance of ABJs under thermal cyclic loading. This approach uses a cost-effective nanoparticles to enhance ABJs performance.

1.4 Thesis Layout

The work carried out to achieve the set goals are presented within seven chapters in this thesis, with its first chapter including the current introductory sections. Chapter 2 presents a summary of the literature reviewed in regard to applications of ABJs, with a special emphasis put on the topic of cyclic thermal loading. The chapter also outlines the studies that have investigated the response of ABJs under different loading conditions, including thermal fatigue. The chapter also covers the literature related to various finite element approaches that have been used to simulate the response of ABJs. In addition, an overview of the cohesive zone model (CZM), its various models and its implementation in a commercially available finite element software (ABAQUS) are presented. Chapter 3 presents details of the experimental investigation designed to examine the response of ABJs to cyclic and mechanical thermal loadings. Chapter 4 provides details of the computational framework used to simulate the response of the experimentally tested specimens. Finite-element models are constructed using the commercial finite-element code ABAQUS, by incorporating the CZM. The chapter provides the details of how the parameters required by the CZM are established and implementation of the CZM in ABAQUS. Chapter 5 outlines the approach used to minimize the stresses causing debonding of composite/metal ABJs subjected to combined cyclic thermal and mechanical loads. This is done by optimizing the stacking sequence of FRP adherend, and thereby minimizing the overall joint stresses. The enhancement of joint performance is augmented by inclusion of nanoparticles, as presented in Chapter 6. Finally, Chapter 7 presents the summary and overall conclusions of the study, followed by providing recommendations for future research.

Chapter 2: Literature Review

2.1 Summary

This chapter aims to review and summarize the pertinent literature related to the fracture mechanics (FM) based approaches used for assessing the response of differently configured ABJs, subjected to different loading conditions. In order to summarize the literature review on ABJs and present a comprehensive overview of the current state-of-the-art published works, the reviews are summarized into four sections. First, a summary of the notable studies on the effect of different loading conditions on adhesives and FRP composites is presented. Then the notable studies concerning Mode I fracture of ABJs are reviewed, followed by the studies concerning Mode II and mixed mode fracture of ABJs. Finally, the notable studies related to adhesively bonded lap strap joints are reviewed. Since the finite element (FE) simulation constituted an important part of this thesis, the last section in this chapter will review the FE approaches that have been used for simulating the response of ABJs, with a concentration on details of CZM technique.

Traditionally, the design of ABJs has been carried out based on a variety of stress-based approaches. In recent years, however, the use of FM has become increasingly popular in the design and analysis of ABJs. While the FM offer several approaches for assessing the performance of ABJs (Ashcroft et al. 2010), accurate evaluation of life-cycle and long-term performance of ABJs remains a challenge. Historically, the theoretical basis of the FM approach was introduced at the beginning of the 20th century, with its first real industrial applications being developed in the 80s. From the late 90s onward, FM has been commonly used in design and analysis of ABJs. It should be noted that the original FM-based approach was well-suited for joints with brittle behaviour. Figure 2-1 shows the most common failure modes of fracture (Anderson, 2017).
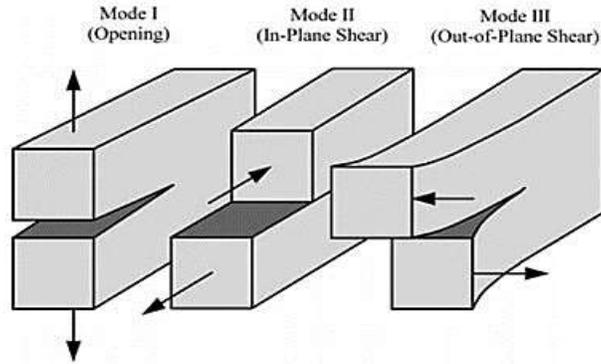
Figure 2-1 Various fracture modes (Anderson, 2017)

FM-based methodologies establish the locus of failure, crack initiation and propagation behaviour, relating crack extension occurring in two different cracked bodies (i.e., a laboratory standard specimen and an engineering structure), based on the similarity of the respective near crack tip stresses and deformation fields. In this regard, the most important parameters in FM are the strain energy release rate (G) and crack tip stress intensity factor, K. Parameter G represents the amount of elastic energy released when the defect/crack grows one unit of area. The critical value of G is considered as a material property (G_c). Fracture toughness properties of different material systems are evaluated by fracture toughness tests conducted on specimens under fracture modes. Several experimental methods exist for evaluating the different fracture mode energies. The most common procedures available for the quantitative evaluation of fracture toughness are the double cantilever beam (DCB), for Mode I; the end notched flexure beam (ENF), for Mode II; and the single-leg beam (SLB), for mixed-mode, as illustrated schematically in Figure 2-2 (Anderson, 2017). It should be noted that the single leg beam specimen configuration is also referred to as the mixed-mode beam configuration. It is noted that polymeric resins are generally ductile and other methods such as the J-integral, crack-tip opening angle (CTOA) and crack-tip opening displacement (CTOD) could better represent their fracture response. However, tests involving calculation of the strain energy release rate are commonly used for assessing the fracture response and toughness of resins (and adhesives) their toughness of resin and adhesives.
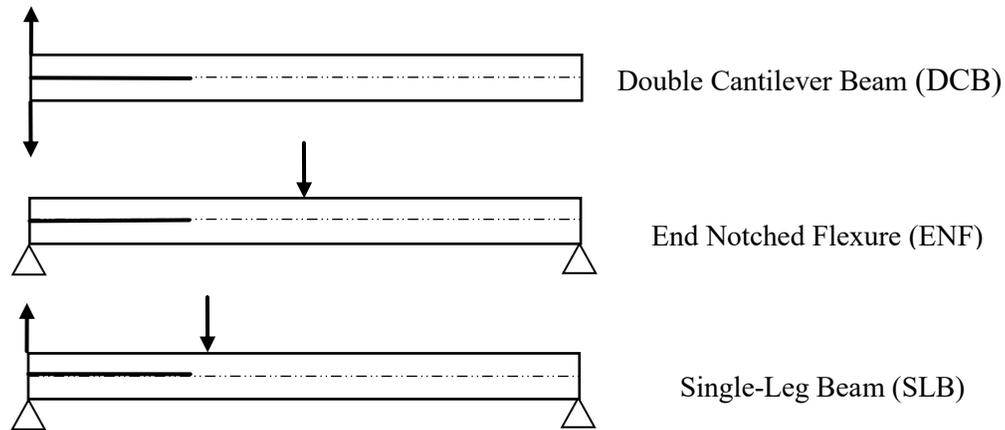
Figure 2-2 Common fracture mechanics test method for evaluating Mode I, II and mixed-mode fracture toughness values (Anderson, 2017)

2.2 Literature Review on Adhesively Bonded Joints

Several investigators have examined the response of various configurations of ABJs subjected to different loading conditions, experimentally and numerically. This section presents a brief review of some of the relevant works available in open literature.

2.2.1 Notable studies on the effect of different loading conditions on adhesives and FRP composites

Several researchers have investigated the influence of thermal cycling and different loading conditions on mechanical response of epoxy resins and FRP (Wicaksono and Chai, 2013). For instance, Bascom and Cottington (1976) investigated the effect of temperature on an elastomeric-modified epoxy resin. They found that the bulk fracture toughness of the resin increased sharply when the test temperature neared glass transition temperature (T_g) of the resin, similar to what was observed in the case of their unmodified resin. It was also observed that the adhesive's fracture energy broadened and shifted with increasing temperature when thicker bond lines were used. Kumar et al. (2002) investigated the degradation of an IM7/997 carbon fiber-reinforced epoxy exposed to ultraviolet radiation and condensation. They concluded that matrix-dominated properties were affected the most, with the transverse tensile strength decreasing by 29% after only 1000 hours of cyclic exposure to UV radiation and condensation. However, their FRP's longitudinal fiber-dominated properties were not affected by the exposure durations.

10

Da Silva and Adams (2005) evaluated the mechanical response of structural epoxy adhesives in tension and shear over a wide range of temperature (i.e., −55 to 200 °C). They examined three different adhesives; a bismaleimide adhesive formulated for use at high temperatures and two paste-form epoxies, for use at low temperatures. They concluded that the combination of bismaleimide and one of the paste adhesives (i.e., Supreme 10HT), produced the most resilient joint with an excellent carrying load capacity in the selected temperature range. Also, Fiedler et al. (2005) studied the influences of stress state and temperature (over a temperature range of −50 to 180 °C) on the continuum and fracture responses of five different epoxy resin. One of the considered epoxies was L135i, a room-temperature cured epoxy resin, similar to the resin used in our study. The results of their mechanical tests conducted to evaluate the compressive, tensile, and shear strengths, and their fractographic study of the fracture surfaces were correlated with the stress state-dependent strength of the resin. It should be noted that the tensile strength of all bulk resins becomes affected by the in-service temperature, as well as their inherent T_g. Moreover, it has been observed that brittle epoxy resins exhibit an extended plastic deformation response before fracturing when subjected to a combined shear loading state and elevated temperature.

Grohs (2007) compared bulk and in-situ constitutive properties of a structural adhesive. He concluded that shear test provided a straightforward and an accurate mean for predicting the in-situ performance of bulk adhesives throughout both the linear and nonlinear regimes. It was also concluded that prediction of the yield strength and plastic deformation of the in-situ adhesive was not possible by using the conventional failure criteria that generally utilize the properties that are obtained based on testing bulk adhesives. The examined criteria, however, did not consider any void effects, stress singularities, or loading eccentricities that could occur during testing. Eslami et al. (2012) also studied the effects of aging on the flexural stiffness and bending capacity of perforated E-glass fiber-reinforced epoxy composite tubes subjected to combined moisture and elevated temperatures (60% humidity and temperatures of 40, 60 and 80°C). Their results indicated that increase in temperature reduced the diffusion coefficient of the material, thus facilitating increased moisture absorption. As a result, the flexural stiffness and bending capacity of the FRP was degraded markedly.

In reference to investigations that evaluated the performance of fiber-reinforced composites under fluctuating temperatures, Hawileh et al. (2015) evaluated degradation in the elastic modulus and tensile strength of E-glass FRP, carbon FRP, and their hybrids, exposed to different temperature ranges (from 25 to 300 °C) for 45 min. The decrease in the mechanical properties of the E-glass FRP and carbon FRP sheets was more severe than that of the hybrid composite sheets. Reductions in the elastic modulus of the composites when exposed to 250 °C compared to those measured at room temperature were approximately 28%, 26%, and 9%, respectively, while the tensile strength degradation levels were at 42%, 31%, and 35%, respectively. Furthermore, brittle rupture failure mode of fibers was observed in the specimens that were tested in low-temperature ranges (i.e., 100–150 °C), while splitting failure mode was observed in specimens tested in high-temperature ranges (i.e., 200–250 °C). It should be mentioned that at 300 °C, the epoxy adhesives were burned out and the specimens failed by rupture of the fibers. In another notable study, Ou et al. (2016) investigated the effect of strain rate and temperature on mechanical properties of a unidirectional glass fiber-reinforced polymer. They presented the stress–strain response of the FRP at varying strain rates and elevated temperatures. The Weibull model was used to quantify the degree of variability in the tensile strengths, generating the parameters that could be used in future engineering applications of the FRP.

In another study, Grammatikos et al. (2016) studied the effects of hygrothermal aging on the durability of a pultruded flat FRP sheet immersed in distilled water at 25, 40, 60 and 80 °C for 224 days. The tensile properties remained practically unaffected by the aging, whereas the matrix dominated shear properties experienced an initial decrease. Spectroscopy analysis showed no chemical degradation incidents on the fiber reinforcement surfaces, and infrared spectroscopy revealed superficial chemical alteration in the aged matrix. Furthermore, in another work, Grammatikos and his coworkers (2016) investigated the effects of thermal cycles on the structural integrity of a pultruded glass-FRP. The study investigated sets of dry and soaked FRP specimens conditioned in distilled water for 224 days, subjected to different temperatures, for a total of 300 cycles. Results showed a significant degradation of the tensile and shear strengths of their soaked specimens, while a negligible degradation was observed in the dry samples' mechanical properties. Moreover, Dogan and Atas (2016) experimentally investigated the effects of hygrothermal aging

12

on the mechanical properties and impact behavior of unidirectional glass-epoxy composites. Their specimens were conditioned at a constant temperature of 95 °C and a constant humidity of 70% for different periods of times, ranging from 0 h to 1200 h. The properties evaluated were the modulus of elasticity, longitudinal and transverse strengths, shear strength, and Poisson's ratio. They concluded that the most influenced (degraded) property was the modulus of elasticity in the transverse direction, while the least affected one was the shear modulus. Moereover, the perforation threshold of the composite materials also decreased with the increase of conditioning time. Recently, Viana et al. (2017) also studied degradation of the mechanical response of epoxy adhesives as a function of temperature. Aged and unaged dogbone tensile specimens of two epoxy adhesives were tested under different environmental (temperature and moisture) conditions. It was observed that the tensile properties of both adhesives were not affected by aging time; however, they were affected by temperature and moisture. Moisture causes plasticization of resins, thereby adversely affecting their strength, stiffness, and increasing their ductility.

2.2.2 Notable studies concerning Mode I fracture of ABJs

Several researchers have investigated Mode I fracture of resins and ABJs. Alfano et al. (2007) studied Mode I fracture in ABJs by modeling a pre-cracked bonded DCB specimen using an intrinsic piece-wise linear cohesive surface relationship. FE implementation of their CZM was accomplished by means of the user element (UEL) subroutine in ABAQUS. The sensitivity of the parameters used in their CZM (i.e. fracture strength and critical energy release rate) in predicting the overall mechanical response was examined. Subsequently, Alfano et al. (2009) explored various CZMs in order to characterize cleavage fracture in ABJs. A Mode I cohesive model was defined, which correlated the tensile traction and displacement jump (i.e., crack faces opening) along the fracture process zone.

It should be noted that in order to determine the traction-separation relation, the main fracture parameters, namely the cohesive strength and the fracture energy and their variation as a function of crack opening parameters, had to be evaluated and specified. However, the evaluation of these parameters involves onerous and time-consuming experimental investigations. To overcome the

difficulties associated with the direct measurement of the fracture parameters and establishment of the cohesive strength, researchers have often used the numerical-tuning concept. To do so, a series of trial numerical simulations using a reasonable range of the fracture energy and crack-opening load-displacement curves are used to simulate the response of an ABJ (often used in analysis of the DCB configuration in the literature). Then, the properties are varied (or "tuned"), such that the response of ABJ simulated numerically is matched to that obtained experimentally. This strategy will be discussed in more detail in Chapter 4.

Using the abovementioned strategy, Li et al. (2005a) used a CZM approach to model Mode I fracture of ABJs formed by polymer matrix composite adherends. It was concluded that there is a distinction between the characteristic strength at the interface associated with the toughness and the intrinsic cohesive strength of the interface. Note that the intrinsic cohesive strength is also required to analyze some geometries that have very small characteristic dimensions or crack lengths. In another paper, Li and his coworkers (2005b) presented a two-parameter CZM model, which included a characteristic toughness and a characteristic strength, for predicting the fracture response of notched or cracked specimens. They determined that the engineering response (i.e., strength, deformation, and energy dissipation) could be well-described by their two-parameter model; however, when considering laminated composites, additional parameters (e.g., the matrix cracking strength), had to be incorporated into their model in order to obtain accurate results.

Several other investigators have also incorporated CZM to investigate Mode I delamination initiation and its growth under quasi-static loading and fatigue by using the damage tolerance concept. For instance, Khoramishad et al. (2010) constructed a framework based on the strain-fatigue damage model in conjunction to CZM to simulate the deleterious influence of fatigue loading on ABJs. Moreover, Banea et al. (2011) conducted experimental and numerical investigations to study the influence of temperature on Mode I fracture toughness of ABJs. They noted, as adhesives' mechanical properties changed under various temperatures, so did their fracture toughness. They conducted Mode I fracture test using the DCB specimen configuration in order to evaluate the effect of the temperature on the adhesive Mode I fracture toughness of high-temperature epoxy adhesive. In their numerical study, they incorporated a CZM that was based on

the bilinear traction separation model. Their numerical predictions of the response of the joint subjected to various temperatures agreed closely to their experimental results. The sensitivity of various CZM parameters used in their model for predicting the overall mechanical response was also examined. In addition, the mesh sensitivity issue was also explored in detail to ensure that the results obtained were mesh-independent.

An example of the CZM's application for simulation of the effect of cyclic loading on ABJs can be seen in the work of Banea et al. (2011). They investigated the variation of Mode I fracture toughness of an ABJ as a function of temperature, both experimentally and numerically. The response of the adhesive as a function of temperature was examined using DCB specimens. They used CZM by incorporating a bilinear traction separation model, and the ABJ's crack mouth opening response was predicted as a function of the applied temperature. They obtained good agreement between their predicted and experimental results. The sensitivity of their selected CZM's parameters, as a function of temperature, was also examined. They concluded that the accuracy of their numerical results was essentially controlled by the input value of the fracture toughness. In other words, the parameters representing the cohesive strength of the adhesive layer did not have any significant influence on the results, except when low values of cohesive strength were used in their simulations. Hu et al. (2013) introduced an environmental degradation factor into a CZM to predict degradation in strength of a single lap joint as a result of cyclic thermal loading.

2.2.3 Notable studies on Mode II and mixed mode fracture of ABJs

Several studies have examined Mode II and mixed mode fracture response of ABJs. Some of the more relevant ones are briefly noted in this section.

Xie and Waas (2006) and Lee et al. (2010) developed systematic procedures for determining the parameters that were required by their adopted CZM technique for characterizing the response of Single Leg Bending (SLB) test specimens under mixed-mode (I/II) dominant fracture state. They also proposed an optimization technique for the system. They could successfully predict the failure

response of their SLB joints with their CZM approach with good accuracy. One of the very few studies that evaluated the performance of CZM for simulating the response of thermally loaded ABJs is that conducted by Banea et al. (2012). In that study, the variation of Mode II fracture toughness of an ABJ as a function of temperature was studied both experimentally and numerically. The response of the adhesive as a function of temperature was examined using the ENF test specimen. They used the CZM by incorporating a bilinear traction-separation law, and ABJs load-displacement response was predicted as a function of the applied temperature.

Azevedo et al. (2015) used CZM for evaluating Mode II fracture response of ABJs by modeling the response of the End-Notched Flexure (ENF) specimens formed by aluminum adherends, mated with three different types of adhesives. The adhesives used were Araldite AV138, Araldite 2015 and SikaForce 7752, which have different degrees of ductility. They demonstrated CZM could predict the strength of the ABJs in the shear mode with good accuracy. In another notable study, Khoramishad et al. (2016) proposed a direct CZM technique for evaluating the traction–separation models (TSMs) used for characterizing Modes I, II and mixed-mode fracture using a single mixed-mode bending (MMB) specimen. Their methodology was based on a two-step mixed-mode test. In essence, they tested the same MMB specimen under two different mixed-Mode ratios and incorporating the compliance-based beam method's equations for Modes I and II when calculating the compliance of their mixed-mode compliance. They obtained good agreement between the traction-separation relationship obtained by their proposed method, and those obtained through the DCB and ENF tests.

In another study, de Moura and Gonçalves (2014) investigated the performance of CZM by developing a model for predicting the response of ABJs that had been subjected to high-cycle fatigue under mode II loading. They incorporated a damage parameter that was based on degradation of the material under both static and fatigue loadings. The damage parameter was used to account for the material's stiffness deterioration as a function of the number of applied loading cycles. They also proposed a data-reduction scheme for monitoring the variation of the energy release-rate that is observed in a typical DCB fatigue test. This was achieved by incorporating the equivalent crack concept. In a follow-up study, de Moura et al. (2016) characterized the

Fatigue/fracture of ABJs made of composite adherends subjected to Mode I, Mode II and mixed-mode (I/II) loadings.

2.2.4 Notable studies on adhesively bonded lap strap joints

Hybrid joints made of FRP adherends have gained considerable attention in recent years. One of the earliest studies on such joints was conducted by Butkus (1997) who evaluated the environmental durability of adhesively bonded aircraft joints using FM and the strain energy release rate concept. He investigated performance of joints fabricated with three aerospace material systems (i.e., aluminum, graphite-epoxy and boron-epoxy), mated with three different adhesives (two epoxies (FM73 and AF191), and a polyimide-based adhesive). DCB and ENF configured joints were subjected to as high as 10,000 hours of isothermal and thermal cyclic conditions, simulating aircraft service environments. Increased degradation in fracture toughness (i.e., Mode I, Mode II, and mixed mode values) was observed when joints were subjected to monotonic environmental exposure. He also found that the environmental exposure caused reductions in the failure strain, strength, and toughness, of the adhesive specimens; it also adversely affected the toughness and fatigue threshold of the ABJs. In another study, Ashcroft et al. (2001) investigated the effect of environment and pre-conditioning fatigue behavior of carbon-epoxy lap–strap joints. They concluded that the fatigue resistance of the lap strap joints did not vary significantly until the T_g, was approached, at which point a considerable reduction in the fatigue threshold load was observed.

A follow-up study by Wahab et al. (2001) analyzed the fatigue strength of the ABJs, using a nonlinear stress analysis and FM. The analysis was performed to predict the strength of the joints under different hostile environmental conditions, in which several threshold criteria were also investigated. A criterion based on the principal stress was found to facilitate accurate prediction of the threshold within a small plastic deformation regime. They also demonstrated that the use of maximum principal strain, von Mises strain, von Mises stress and the maximum shear stress criteria could produce the fatigue thresholds of the joints that had experienced large plasticity with good accuracy. Liljedahl et al. (2007) also investigated the long-term behavior of single- and

17

double-lap composite/aluminum ABJs under different environment conditions. Both aluminum-aluminum and CFRP-CFRP joints were considered in the study. They considered various combined environments (i.e., 80% RH /70 °C, 96% RH /50 °C), as well as immersion of their specimens in de-ionized and tap water, both at 50°C. They also took account of their water conductance. The specimens were conditioned for a relatively long period of 78 weeks so to characterize their creep response. In addition, they conducted the X-ray photoelectron spectroscopy (XPS) analysis to determine any evidence of charge carrying potential that could lead to corrosion within the joint and further degradation of bonding surfaces. They also modeled the failure of the joints using a CZM approach with 2D and 3D modelling approaches. They obtained the input parameters of their CZM model by conducing FM tests. Overall, the prediction of their unsaturated specimens' failure with CZM approach was in good agreement with the results observed experimentally. However, CZM overestimated the results for the saturated joints. They attributed the overestimation to the large residual stresses that could have developed as a result of the infusion, which was not accounted for by their model. In addition, they used the XPS to investigate the failure surface degradation.

Later, Ashcroft et al. (2008) studied the mixed-mode crack growth in epoxy bonded CFRP lap-strap joints under two loading conditions. First, the joints were subjected to the standard fatigue loading, with the load amplitude equaling 60% of the average quasi-static failure load of the joint. In another set of experiment, the joints were subjected to repetitive impact loading generated by a pendulum. The strain gauges were mounted on both free surfaces of the specimens (referred to back face strain technique); standard gauges were used for monitoring cracks in the specimens subjected to standard fatigue loading, and piezoelectric strain gauges were used to monitor the strain response of impacted fatigue joints. They observed higher crack propagation rates in joints subjected to the impact fatigue than those that were subjected to standard fatigue loading, even when the maximum load was significantly lower than the load causing failure of the specimens that were subjected to quasi-static loading.

The response of doubler ABJs made of FRP/aluminum adherends, subjected to thermal cycling with temperature variation of -40 °C to +25 °C was investigated by Baftechi (2008), both

numerically and experimentally. Specifically, E-glass-epoxy and carbon-epoxy formed the FRP adherends that were bonded to an aluminum substrate. Baftechi used 3D FE models to establish the optimal lamination sequence that would produce the least thermal stress mismatch in the joints. Various ply sequences (i.e., unidirectional, angle ply, cross-ply and quasi-isotropic) were considered. The numerical results were compared with experimental results. The results indicated that the thermal cycling induced the most significant degradation in joints formed with cross-ply carbon-epoxy. It was observed that after 80 cycles, the joint would retain only 69% of its original strength, while under similar thermal loading, the unidirectional glass-epoxy ABJ lost only 9% of its original strength. The study concluded that doubler joints made of unidirectional glass-epoxy/aluminum adherends would be the optimal configuration for service in a cyclic thermal environment. In another study, Gutwinski and Schauble (2009) performed numerical and experimental investigations to study the effect of shock and continuous thermal cycling on a laterally closed CFRP foam-core sandwich structure. The specimens were exposed to temperature range of -55 °C and 80 °C, simulating the thermal cycles occurring in a typical commercial flight. Specimens were exposed to 10, 100, 500 and 1000 thermal cycles and then mechanically tested under four-point bending test and compared with non-cycled reference specimens. Also, a heat transfer numerical simulation was carried out using the FE program MSC-Marc. It was concluded that the failure was more pervasive in specimens that were subjected to thermal shock as opposed to those subjected to the continuous cycles. Interestingly, the specimens that were subject to 500 cycles exhibited higher strength compared to the baseline specimens, while those undergoing 1000 cycles exhibited comparatively less strength.

In addition, Nguyen et al. (2012) conducted tensile tests to establish the degradation in strength and stiffness of steel/CFRP double strap joints specimens that were exposed to various environmental conditions. They also developed an analytical model to predict the mechanical degradation of the joint. In that, they exposed several ABJs to various environmental conditions (i.e., simulated sea-water at 20 °C and 50 °C, combined constant temperatures at 50 °C and 90% RH and combined fluctuating temperatures (between 20 °C and 50 °C) and 90% RH). They found that the strength and stiffness of the joints that were exposed to simulated sea-water degraded the most, while the joints that were exposed to the combined temperature and humidity showed the

least degradation. Their developed model's predicted degradation in strength and stiffness of the joints exposed to sea-water agreed closely to their experimental results, thus validating the integrity of their model. In another notable study by Sugiman et al. (2013c), ABJs were aged in deionized water at 50 °C for up to two years. The test results showed that the fatigue life degraded with increasing moisture content and tended to level off when approaching saturation. Han et al. (2014) also investigated the residual static strength of ABJs after long-term exposure to a combined mechanical-hygro-thermal environment both experimentally and numerically. Following the aging phase, a CZM approach was used to conduct a progressive damage FE analysis of the quasi-statically loaded joints. The predicted and experimentally-measured quasi-static responses of the aged adhesive joints were found to be in good agreement.

In another notable study, through a dual experimental and numerical investigation, Heshmati (2017) studied the mechanical response of aged FRP/steel joints, assessing their durability and long-term performance. ABJs were subjected to various temperature ranges and humidity levels and cycles. The experimental results showed that the mechanical performance of joints degraded after exposure to hygrothermal ageing conditions. The results of his FE simulations showed that the failure modes could be predicted fairly accurately, and the sequentially coupled moisture diffusion–fracture analysis was found to provide reasonable predictions of the mechanical behavior of his environmentally aged joints. In another recent study, Al-Ramahi (2018) studied the distribution of stresses in a single-lap joint subjected to mechanical and thermal loading numerically. 2D and 3D models were considered, and the nonlinearity of the joint materials and the geometrical nonlinearity were both accounted for in their simulation. The responses of three different types of single lap joint with similar and dissimilar (hybrid) materials were investigated (i.e., metal/metal; composite/composite and composite/metal). Results showed that the residual thermal stresses reduced the maximum magnitudes of the shear and peel stresses. It was also demonstrated that the stacking sequence of the composite adherends had a notable effect on the variation of stresses within the adhesive. For instance, the peel at the ends of the overlap region was reduced by approximately 60-70% when a 0-degree ply was placed adjacent to the adhesive in comparison to the case when a 90-degree ply was adjacent to the adhesive (the angles are with respect to the longitudinal axis of the joints).

2.3 Fracture Analysis and Simulation using the Cohesive Zone Approach

Development of an analytical solution that could predict the response of ABJs under various loading conditions, especially those subject to thermal cycles, is a complex and challenging task. The emergence of recent computational advances, however, has enabled researchers to depict the performance of such ABJs with a reasonable accuracy. A relatively recent numerical method that has been utilized for such tasks is the CZM methodology, (Elices et al., 2002), (Tabiei and Zhang, 2018). In this section, a brief background to CZMs is presented. In addition, the procedure used to establish the required parameters by ABAQUS, a commercially available finite element software, is also discussed.

2.3.1 Cohesive or damage zone models overview

It was the original work of Dugdale (1960) in consideration of a notched material that introduced the association between fracture and strength criteria, which is the foundation of CZM. He introduced the concept that stresses in a notched material are limited by the yield stress and that a thin plastic zone is generated ahead of the notch. In order to solve the problem of equilibrium, Barenblatt (1962) subsequently considered the cohesive forces on a molecular scale in elastic bodies with cracks. These two researchers were therefore the pioneers who applied the concept of the cohesive stress in modeling of fracture process, recognizing the fact that a yielded zone at the tip of a crack would result in a reduction in the stress singularity (see Figure 2-3). It would therefore be fair to refer to CZM as the Dugdale-Barenblatt model (Elices et al., 2002). The application of the concept of Dugdale-Barenblatt approach was subsequently extended and used in conjunction with the finite element method by Hillerborg for assessing fracture in concrete (Hillerborg, 1991; Hillerborg et al., 1976). This approach became known as the Hillerborg fictitious crack model. The model has also been referred to as the CZM. The latter model is similar to Barenblatt's model, but Hillerborg's model assumes that the stress displacement behavior (σ-δ) observed in the damage zone of a tensile specimen is a material property (Anderson, 2017), while Hillerborg's model considered the growth of an existing crack. The interesting and significant contribution of it was that it also considered the initiation of new cracks. Since then, CZM has become widely used to solve various problems involving crack initiation and growth. It is by using and combining

a suitable strength criterion, and an energy dissipation criterion that a single model could account for both failure causing phenomena (i.e., crack initiation and growth).
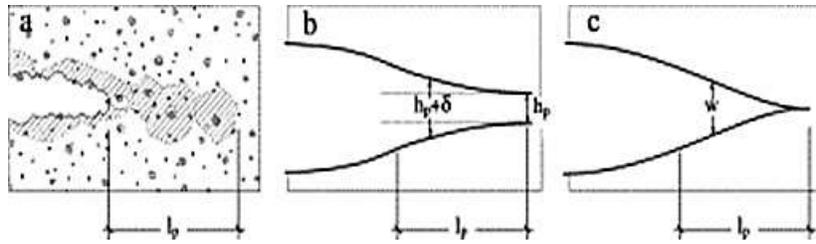
Figure 2-3 (a) Sketch of the process zone PZ (shaded area), (b) Sketch of a cohesive band process zone and (c) Sketch of a cohesive crack process zone (Elices et al., 2002)

Therefore, the relative ease of application of CZM has rendered it as a very practical and effective approach for assessing cracked bodies. By implementing CZM within a suitable finite element formulation, one can predict and simulate the initiation of a non-existing crack, and its propagation (Schwalbe et al., 2013). This approach can also account for crack tip plasticity and creep, crazing in polymers, and simulate the response of ABJs, delamination in composites and multilayered materials, to name a few. Another advantage of a combined CZM and FEA approach is the fact that the analysis can be done with a relatively coarse mesh. This is because unlike the conventional finite element approach, the analysis does not have to simulate crack tip singularity, and that the amount of absorbed energy is not very sensitive to the mesh density. Moreover, CZM can predict initiation and growth of cracks in cracked and non-cracked geometries under monotonic or cyclic loading conditions. In essence, CZM relates crack front traction to the sudden variation in the displacement of the interface where a crack may occur and propagate, as graphically illustrated in Figure 2-4. Moreover, damage initiation is related to the interfacial strength that is embedded in the traction-displacement relation. When the area under the traction-displacement relation equals to the fracture toughness (G_c) of the material, then a new crack surface is created within the material, and the traction is reduced to zero (Turon, 2006). In the case of an isotropic material, the model would have three elements: (i) the critical energy release rate, (ii) the critical or limiting maximum stress, and (iii) the shape of the traction-separation curve.
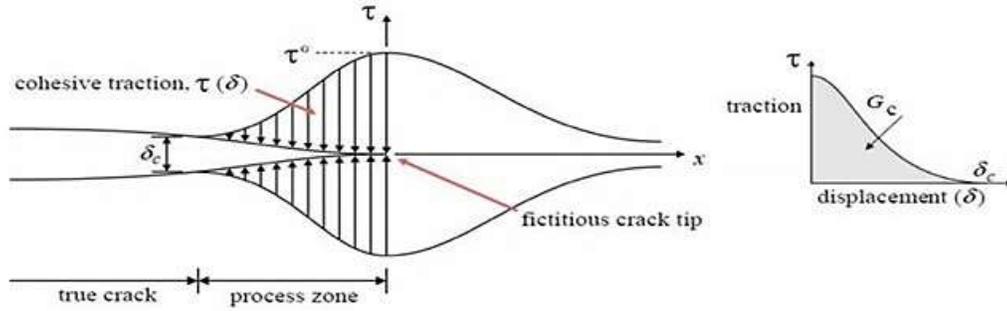
Figure 2-4 Traction in the cohesive zone in crack tip region (Turon, 2006)

2.3.2 Evaluation of cohesive parameters required by ABAQUS

Numerical formulations of CZM are implemented in numerous FE codes. This is essentially done by slightly modifying the actual material's physical traction separation response (as schematically illustrated in Figure 2-5(a)) by the one shown in Figure 2-5(b), so the problem could be solved numerically. In other words, the actual model is changed slightly to include a rather very stiff initial elastic region, mimicking the pre-damage initiation response of the material. In this way, the standard interface elements can be used within FE codes to handle CZM.
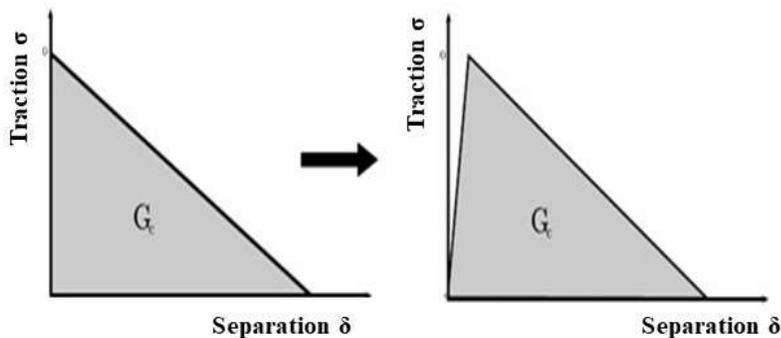
Figure 2-5 Comparison of the (a) actual physical and (b) numerical cohesive models (Turon, 2006)

There are various CZM models that have been developed to describe the pre- and post-fracture states of materials. All the models are essentially based on the energy principle and a traction-separation law, which are used to idealize the mechanism involved in two separating surfaces. These models are distinguished essentially based on the basic functions used to define the traction-

separation response of the material (e.g., bilinear, multilinear, polynomial, trigonometric, and exponential), as schematically illustrated in Figure 2-6.
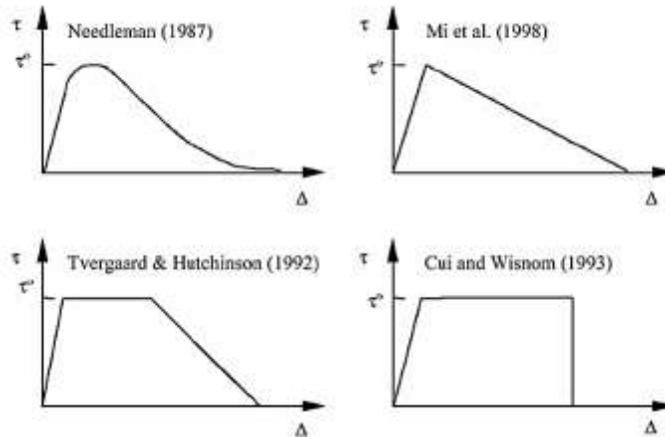
Figure 2-6 Traction-relative displacement curves employed in various models in the literature (Zou et al., 2003)

When analyzing an ABJ, the use of cohesive elements facilitates detailed modeling of the adhesive constituent. According to the available literature, the most widely used traction-separation relationships (or models) are the bilinear, linear-parabolic, trapezoidal and exponential cohesive models (as illustrated in Figure 2-7). One of the original studies that incorporated CZM for analyzing ABJs was that conducted by Alfano (2006).He investigated and examined the influence of the shape of the most commonly used interface traction-separation models by analyzing an interface crack of the selected interface model, pure Mode I and Mode II; on the numerical performance and accuracy of the predicted results. In his study, the trapezoidal model gave the worst results both in terms of numerical stability and convergence of the FE solution compared to the exact solution. The exponential model was found to produce the most accurate results, while the bilinear model was proved to produce the most optimal solution based on a compromise between CPU time and accuracy.
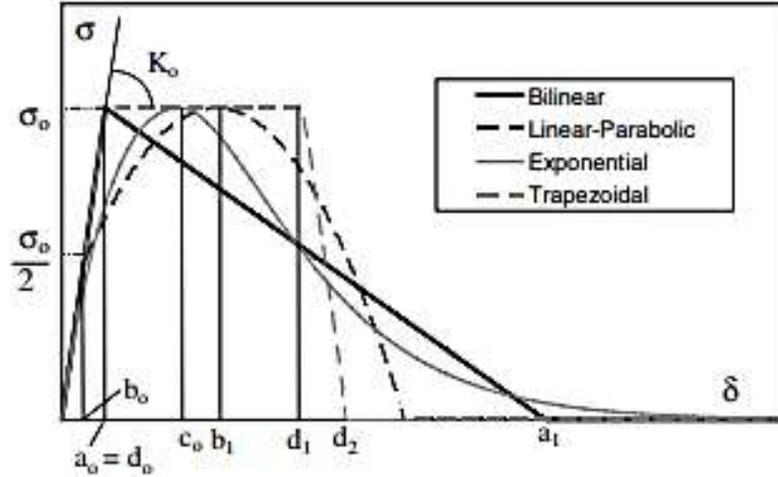
Figure 2-7 Traction-relative displacement curves of studied interface (Alfano, 2006)

As a result, the linear elastic/linear softening, commonly referred to as the bilinear cohesive model is used in the analyses that will be discussed in this dissertation. In the bilinear cohesive model, the stress increases linearly as a function of advancing displacement until the cohesive strength (critical traction) of the material is reached, after which the stress decreases linearly to zero traction, which coincides to the critical opening. The initial elastic range is means of tracing the resulting displacements and multiplying them by the stiffness terms (K_{ij}) of the material. The bilinear cohesive model, as implemented in ABAQUS (2014), is represented by the following mathematical relationship:

$$\sigma = \begin{Bmatrix} \sigma_n \\ \sigma_s \\ \sigma_t \end{Bmatrix} = \begin{bmatrix} K_{nn} & K_{ns} & K_{nt} \\ K_{ns} & K_{ss} & K_{st} \\ K_{nt} & K_{st} & K_{tt} \end{bmatrix} \begin{Bmatrix} \delta_n \\ \delta_s \\ \delta_t \end{Bmatrix} = \mathbf{K}\delta \qquad \text{2-1}$$

where σ is tractions, K_{ij} are the cohesive layer interface stiffness parameters with subscripts n, s and t refer to the normal (out-of-plane), and first and second in-plane shear directions, respectively, and δ is the separation displacement of the cohesive model. (see Figure 2-7 for identification of the symbols).

25
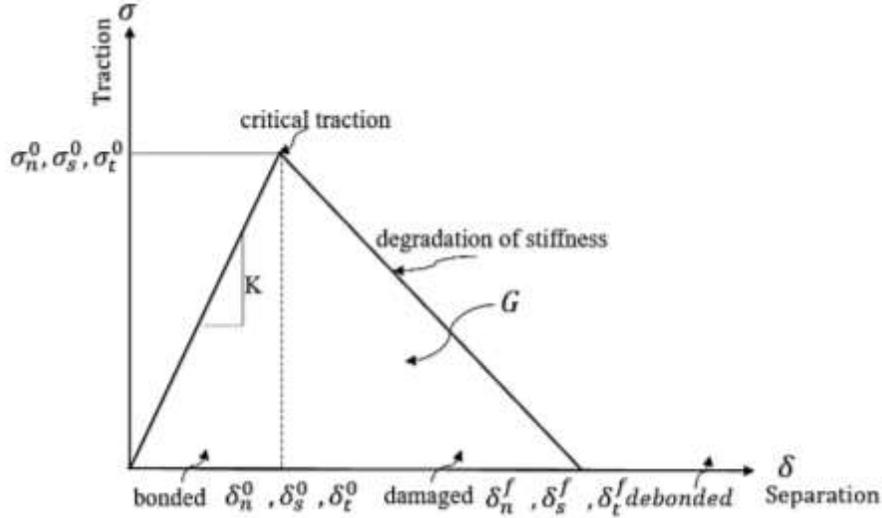
Figure 2-8 Graphical representation of the parameters of the bilinear cohesive model

Based on the graphical representation shown in Figure 2-8, the constitutive relation of the bilinear cohesive traction separation, in the normal direction, can be presented as follows:

(i) For $0 \leq \delta < \delta_n^0$ $\Longrightarrow$ $\sigma = \dfrac{\sigma_n^0}{\delta_n^0} \delta$ 2-2

(ii) For $\delta_n^0 \leq \delta < \delta_n^f$ $\Longrightarrow$ $\sigma = \dfrac{\sigma_n^0 \left(\delta_n^f - \delta\right)}{\left(\delta_n^f - \delta_n^0\right)}$ 2-3

(iii) For $\delta > \delta_n^f$ $\Longrightarrow$ $\sigma = 0$ 2-4

As for the selection of the damage criterion, a large number of damage initiation and evolution failure criteria are available in ABAQUS. The equations representing the most popular damage initiation criteria are briefly noted below. The presence of damage within the material is established once the equality stated by the selected damage initiation criteria is satisfied.

1- Maximum nominal stress criterion

$$Max \left\{ \frac{\langle \sigma_n \rangle}{\sigma_n^0}, \frac{\sigma_s}{\sigma_s^0}, \frac{\sigma_t}{\sigma_t^0} \right\} = 1$$ 2-5

2- Maximum nominal strain criterion

$$Max \left\{ \frac{\langle \varepsilon_n \rangle}{\varepsilon_n^0}, \frac{\varepsilon_s}{\varepsilon_s^0}, \frac{\varepsilon_t}{\varepsilon_t^0} \right\} = 1$$

2-6

3- Quadratic nominal stress criterion

$$\left\{ \frac{\langle \sigma_n \rangle}{\sigma_n^0} \right\}^2 + \left\{ \frac{\sigma_s}{\sigma_s^0} \right\}^2 + \left\{ \frac{\sigma_t}{\sigma_t^0} \right\}^2 = 1$$

2-7

4- Quadratic nominal strain criterion

$$\left\{ \frac{\langle \varepsilon_n \rangle}{\varepsilon_n^0} \right\}^2 + \left\{ \frac{\varepsilon_s}{\varepsilon_s^0} \right\}^2 + \left\{ \frac{\varepsilon_t}{\varepsilon_t^0} \right\}^2 = 1$$

2-8

In above equations, $\langle \; \rangle$ is a Macaulay bracket.

In the same vein, one of the following damage evolution criteria can be used to establish the evolution of damage and its final fracture/failure of the material:

i)　Power Law

$$\left(\frac{G_I}{G_{IC}} \right)^\alpha + \left(\frac{G_{II}}{G_{IIC}} \right)^\alpha + \left(\frac{G_{III}}{G_{IIIC}} \right)^\alpha = 1$$

2-9

or

ii)　BK (Benzeggagh and Kenane, 1996)

$$G_{IC} + (G_{IIC} - G_{IC}) \left(\frac{G_{shear}}{G_T} \right)^\eta = G_{TC}$$

2-10

where:

$$G_T = G_I + G_{shear} \qquad\qquad 2\text{-}11$$

and

$$G_{shear} = G_{II} + G_{III} \qquad\qquad 2\text{-}12$$

Once the initiation criterion is met, the analysis is followed and addressed the damage by adopting an evolution failure criterion. The constitutive equation representing the damage evolution in the normal direction is represented by:

$$\sigma_n = (1 - D)\overline{\sigma_n} \qquad\qquad 2\text{-}13$$

where D is the damage variable. This variable represents the rate at which the material stiffness is degraded once the selected initiation criterion is reached. The value of D is zero initially, and it increases upon further loading and initiation of damage, increasing up to a value of unity, at which the complete failure of the material is realized. In the above equation, $\overline{\sigma_n}$ is the stress component predicted by the elastic traction separation behavior for the material in its undamaged state. Figure 2-9 graphically illustrates the variation of the damage response variable in the cohesive model.
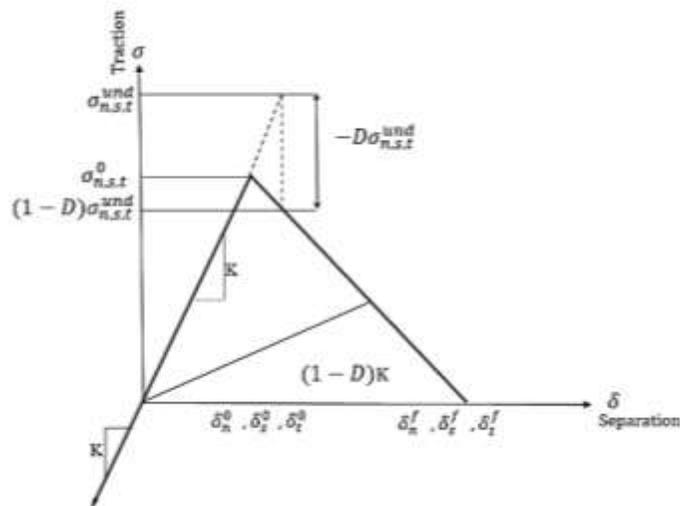
Figure 2-9 Variation of the damage response variable in the bilinear cohesive model

28

ABAQUS can also evaluate the damage evolution (D) under a mixed mode condition according to the schematic shown in Figure 2-10, using the following mathematical relationship.

$$D = \frac{\delta_n^0 \left(\delta_n^f - \delta \right)}{\delta_n^f (\delta_n^f - \delta_n^0)} \qquad \text{2-14}$$
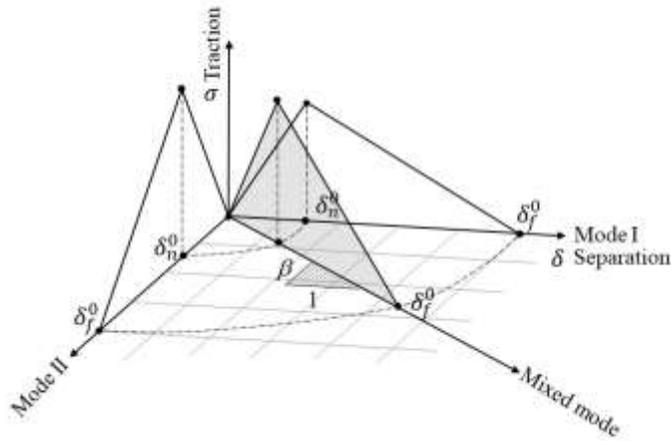
Figure 2-10 Graphical illustration of the mixed mode traction separation interaction implemented in ABQUS

where β in Figure 2-10 represent the "mode-mixity", defined as $\beta = \frac{\delta_{Mode\,II}}{\delta_{Mode\,I}}$.

In most FE codes, CZM is implemented as either element-based and/or surface-based. In our case, ABAQUS, a commercially available FE package, was used to conduct the simulations. Regardless of the code used, the accurate evaluation of the specific CZM that would be used to simulate the response of a material is critical in order to conduct accurate simulation and strength prediction. This would entail the establishment of the elastic and fracture properties, and selection of a suitable damage initiation and evolution criteria. When conducting CZM analysis within ABAQUS, the software outputs a scalar damage variable (SDEG) defining the value of scalar stiffness degradation, a variable that is established based on the selected damage evolution model. (more details will be discussed in Chapter 4).

Chapter 3: Experimental Investigation on Adhesively Bonded Joints Subjected to Thermal Fatigue

NOTE: A major portion of this chapter has been published in Open Journal of Composite Materials (OJCM), Vol.9 No. 2. (Mohamed et al., 2019).

3.1 Introduction

Response of differently configured ABJs subjected to thermal fatigue are investigated experimentally. In addition, the influence of thermal cycles on the performance of a neat epoxy resin and GFRP produced using the same resin is also evaluated experimentally. The DCB, ENF and SLB configurations are used to conduct the investigations. Specimen preparation and testing procedures are presented in detail in this chapter, and results are reported and discussed for all different ABJ configurations. The chapter is finalized by a brief conclusion.

3.2 Problem Statement and Objectives

This investigation was motivated by our long-term objective of better understanding the influence of thermal cycling on the performance of ABJs in which one or more adherends are a fiber-reinforced polymer composite. Specifically, ABJs formed with a room-cured epoxy resin are of interest. In this study, the adherends are made of an E-glass/epoxy fiber reinforced laminate composite (GFRP), and the adhesive is the same as the resin used for manufacturing the adherends (Mohamed et al., 2019). As stated, various joint configurations (i.e., DCB, ENF and SLB specimens) were used throughout the investigation. All specimens were first subjected to heating/cooling thermal cycles, then subjected to mechanical load, as explained hereafter.

3.3 Specimen Preparation

In this section, details on fabrication and manufacturing of each of the test specimens are presented.

3.3.1 Neat epoxy adhesive and unidirectional GFRP specimens

The widely used West System 105 epoxy resin and 206 hardener (Bay City, MI) were used in this investigation. This resin can be cured under a wide temperature range. At room temperature, it would cure in 24 hours. The resin has a minimum T_g, of 60 °C (see Appendix B for more details) Typical dog-bone shape coupons with dimensions of 95x10x5 mm were prepared by pouring the resin into a mold, followed by degassing the resin by vacuum. In addition, eight-ply laminated plates were also fabricated using a unidirectional E-glass stitched-cloth and the same resin by vacuum-assisted hand lay-up technique (for more details see (Mazumdar, 2001)). The plates were cut into 250x25 mm rectangular specimens, with an average thickness of 3.5 mm. The two type specimens, as illustrated in Figure 3-1, conform to ASTM D638 (2008).
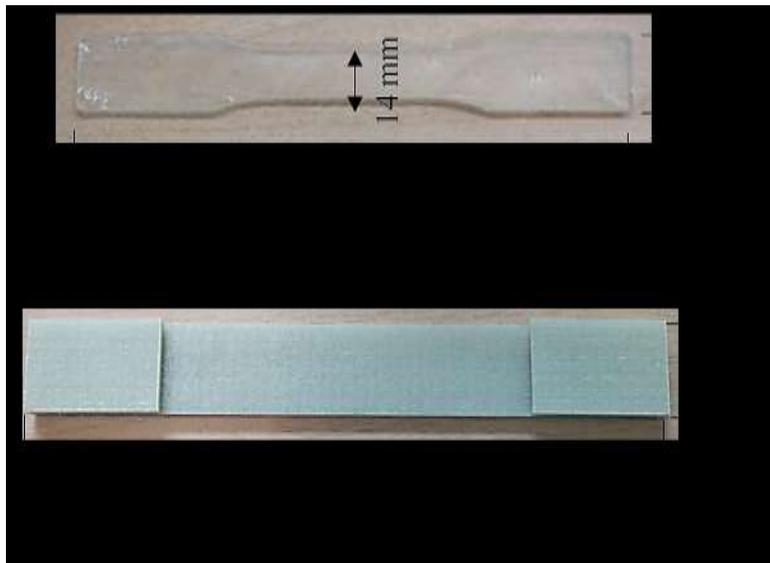
Figure 3-1 (a) Dog-bone tensile neat-resin specimen and (b) tabbed-unidirectional GFRP specimen

3.3.2 DCB test specimens

The composite adherends of the DCB specimens were fabricated using the hand lay-up technique. The composite plates were constructed with eight layers of unidirectional E-glass fabric and the West System room-cured, two-part epoxy resin system. Once the composite plates were fabricated, the mating surfaces of the fiberglass-reinforced composite were roughened to promote optimal

mechanical bonding. The surfaces were sanded using 120 grit metallographic sandpaper. The surfaces were then cleaned by compressed air jet to remove dust, and then wiped lightly with acetone and let air-dry. The plates were then mated using the same two-part epoxy resin. It should be noted that the same resin that was used to fabricate the adherends was purposely used to bond the mating surfaces, as many non-aerospace fabricators follow this practice. Moreover, the degradation of the adhesive resin layer mating the two segments of DCB was evaluated by measuring the fracture toughness of the resin (i.e., G_{ic}).

Specimens' fabrication started by bonding two laminated composite plates with a layer of adhesive. Each adherend plate had an average thickness of 4 mm. A 25 μm thick Teflon film with a width of 50 mm was placed on one edge of each adherend plate to generate the disbond region. Afterward, the tip of disbond region was extended to a sharp crack to a total length of 55 mm following the procedure outlined in ASTM D5528 (2007). Seven layers of masking tape were stacked up and adhered along the other three edges of one of the adherend plates to facilitate the uniformity of the desired 0.2 mm thick interface bond mating the two plates. The adhesive was applied to the mating surface of each plate, and the plates were bonded together and left to cure at room temperature for at least four days, as per adhesive manufacturer's recommendation, under a total uniformly distributed weight of 20 kg. The assembled mated plates were then cut into a series of appropriate-size DCB specimens (i.e., 150 mm x 25 mm), using a water-cooled diamond saw. The fabrication of DCB specimens was finalized by adhering a pair of aluminum loading blocks to the pre-cracked end regions of each specimen, (see Figure 3-2).
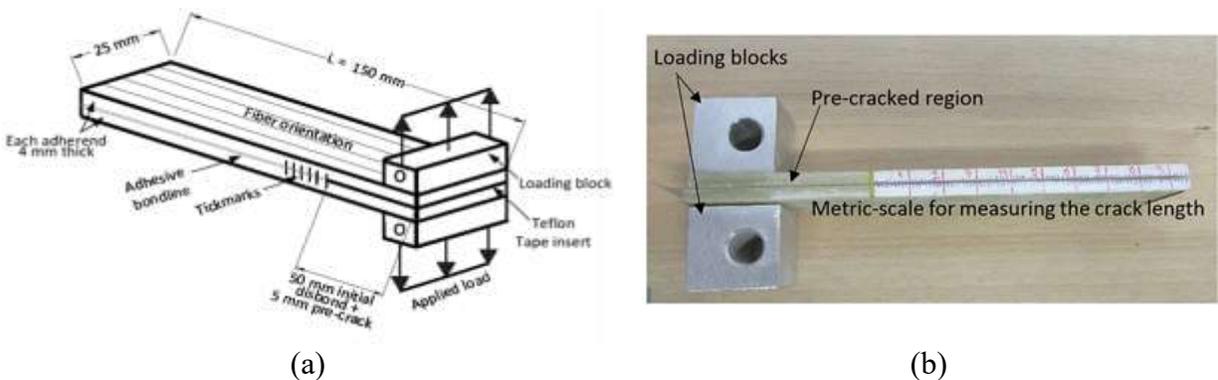
(a)   (b)
Figure 3-2 (a) and (b) DCB specimen' configuration and dimensions

32

3.3.3 ENF specimens

The composite adherends plates used in forming the End-Notched Flexure (ENF) specimens were fabricated using the described hand-layup technique. Note that the width of Teflon tapes was placed on one edge of each adherend plate to generate the disbond region was 70 mm. The assembled mated plates were then cut into the appropriate sizes thus generating the desired specimens, with dimensions shown in Figure 3-3.
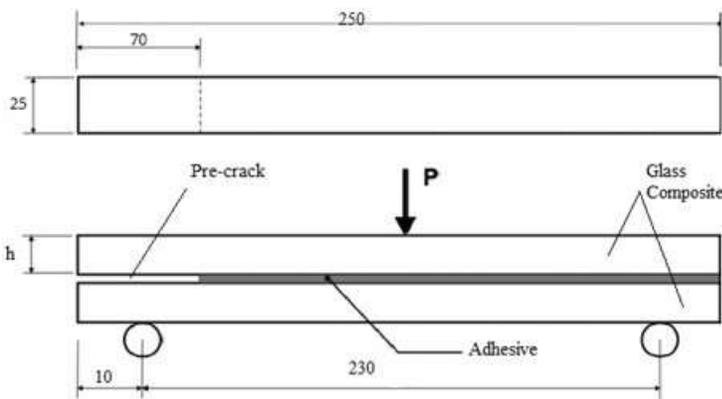
(a)   (b)
Figure 3-3 (a) ENF specimens' configuration and dimensions and (b) Mode II test setup
(units in mm)

3.3.4 SLB specimens

The composite plates used to produce the adherends of the Single Leg Bending (SLB) specimens were fabricated using the aforementioned hand-layup technique. The width of the Teflon tapes placed on one edge of each adherend plate to generate the disbond region was 50 mm. The assembled mated plates were then cut into the appropriate dimensions, thus generating the desired specimens, with dimensions shown in Figure 3-4.

(a)	(b)
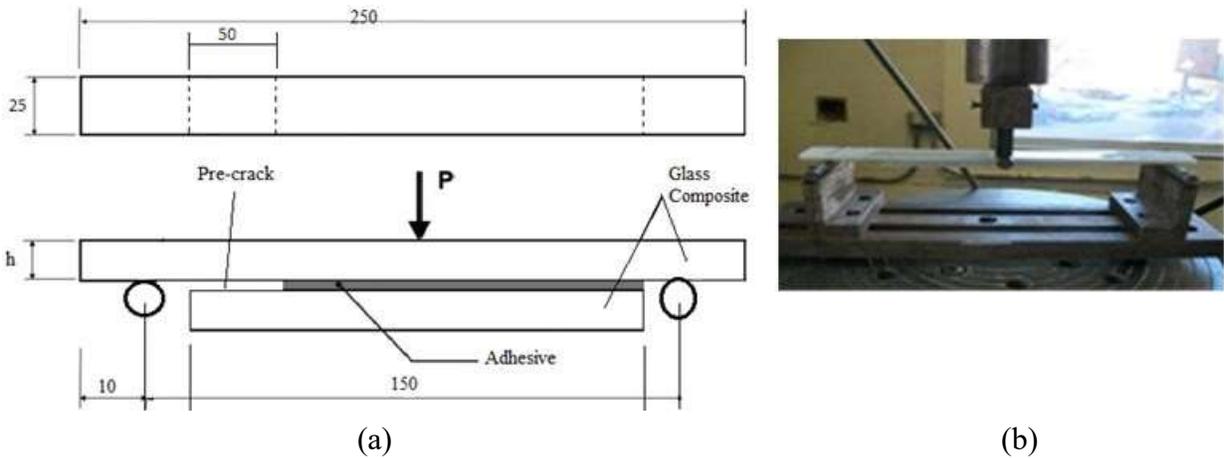
Figure 3-4 (a) SLB specimens' configuration and dimensions and (b) mixed-mode test setup (units in mm)

3.4 Test procedures

In this section, the test procedure for each specimen type is discussed. The tests include the tensile testing of the neat epoxy adhesive and unidirectional GFRP, as well as the tests conducted for evaluating Mode I, Mode II and mixed mode fracture toughness.

3.4.1 Neat epoxy adhesive and unidirectional GFRP

The influence of thermal cycles on the stiffness, ultimate strength and strain of the materials was examined by conducting tensile tests on the adhesive and GFRP after being subjected to thermal cycling. The Fourier transform-Raman spectroscopy (FT-Raman) was also conducted to investigate the influence of the thermal cycles on the curing degree and any chemical changes that could have occurred in the adhesive and composite. In addition, the Differential Scanning Calorimetry (DSC) analysis was performed to investigate the variation in the T_g of the adhesive as a function of the applied thermal cycles.

3.4.1.1 Tensile testing of neat epoxy adhesive and unidirectional GFRP

All tensile tests conducted on the neat epoxy and unidirectional GFRP specimens were performed as per ASTM D638 (2008), using an Instron servo-hydraulic test machine (model 8500+),

equipped with a 100 kN load cell. A laser extensometer (model LE-05, Electronic Instrument Research, Irwin, PA) was used to record the strain in the specimens. Data from the load cell, displacement actuator, and laser extensometer were acquired through a data-acquisition system (DAQ) and stored in a personal computer. The tests were conducted under displacement-control, at a loading rate of 1.5 mm/min, with a data sampling rate of 0.05 kHz. The modulus of elasticity was calculated by using a special code written in Python language, in conjunction with MATLAB's Curve Fitting toolbox, which was used for fitting a line to the linear portion of the stress-strain curve.

3.4.1.2 Fourier transform-Raman spectroscopy analysis (FT-Raman)

Fourier Transform-Raman (FT-Raman) spectroscopy was used to investigate the curing level of the resin in each group of specimens, so to identify and understand the chemical changes that could have occurred within the epoxy resin and GFRP as a result of the thermal cycling. Using the FT-Raman, one can identify the types of chemical bonds by producing an infrared absorption spectrum of the material, similar to molecular "fingerprinting". A Nicolet NXR 9650 FT-Raman spectrometer equipped with a 1064 nm Nd:YVO$_4$ Laser and InGaAs detector was used. All spectra were collected with a 2 cm^{-1} resolution, and the laser power set to 0.5W. All FT-Raman spectroscopy evaluations were conducted at room temperature; however, as will be explained later, additional measurements were performed under various isothermal conditions to detect whether additional curing of the polymer took place as a result of the applied thermal cycles.

3.4.1.3 Differential scanning calorimetry (DSC)

DSC analysis was also conducted as per ASTM E1356-08 (2014), using a TA Instrument Q200 DSC, to evaluate the potential change in the T_g of the room-cured resin after having been subjected to various thermal cycles. The DSC analyses were conducted on approximately 10 mg samples, cut from the tested epoxy resin specimens. Each specimen underwent thermal cycles, with each cycle comprised of heating of the specimen to 150 °C and then cooling down to -45 °C, and again

heating to 150 °C, all at a rate of 10 °C per minute. Replicate samples were runs three times to ensure consistent T_g measurements.

3.4.2 Mode I fracture toughness evaluation

The DCB specimens were tested under Mode I fracture to establish the interlaminar fracture toughness, according to ASTM D5528 (2007). The specimens were loaded at room-temperature by a digitally controlled INSTRON universal testing machine (model 8500+), under displacement control, at a loading rate of 1.5 mm/min (Figure 3-4(a and b)). Each specimen was carefully aligned in the machine using a level. Specimens were loaded via the loading blocks (Figure 3-5 (a) Overview of the experimental setup, (b) close-up view of the test specimen and (c) a typical load-deflection curve generated by the DCB test2(b)). A LabVIEW code was used to control the test machine, and to record the applied load, as well as the actuator's displacement (i.e., the crack mouth opening displacement). The data were acquired through a data-acquisition system (DAQ) and stored in a personal computer. As stated in section 3.3.2, a sharp crack was generated prior to conducting the actual tests following the ASTM suggested procedure. Once the sharp crack was generated in each specimen, the specimen was unloaded prior to initiating the actual fracture toughness tests.
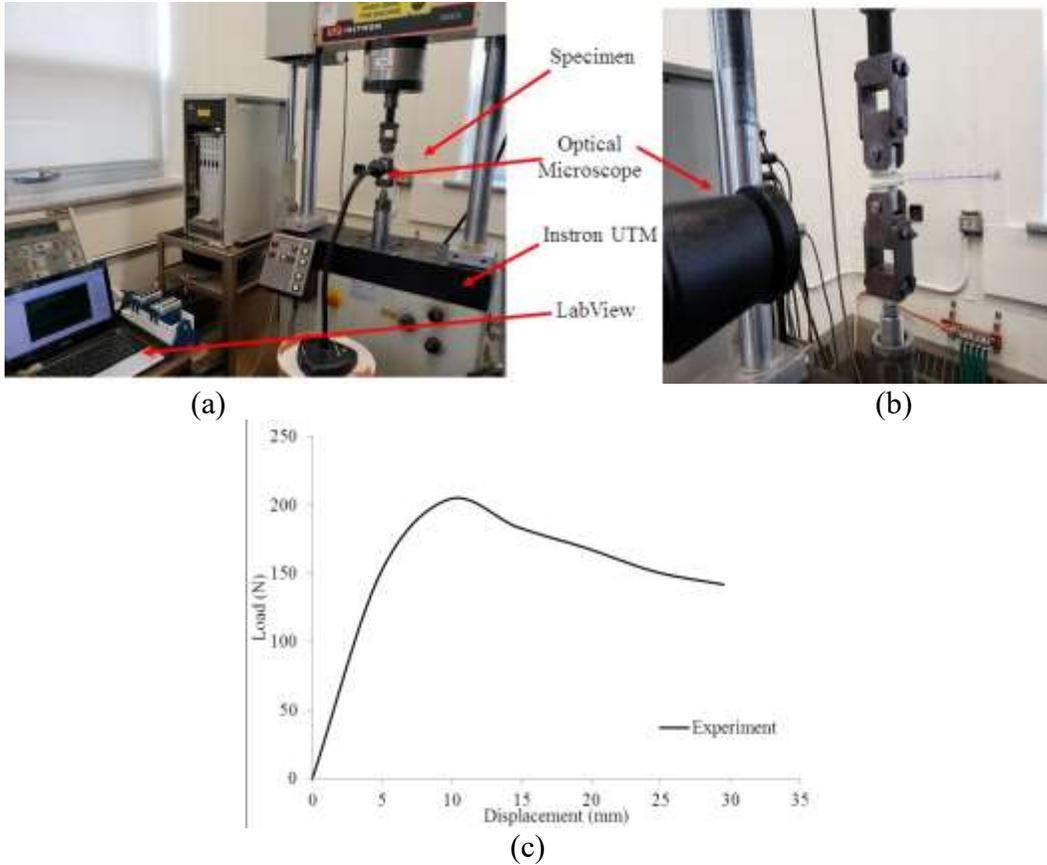
(a)   (b)

(c)

Figure 3-5 (a) Overview of the experimental setup, (b) close-up view of the test specimen and (c) a typical load-deflection curve generated by the DCB test

During the tests, an optical microscope was used to monitor the crack growth through the metric scale inscribed on the side of each specimen (see Figure 3-5 (a) Overview of the experimental setup, (b) close-up view of the test specimen and (c) a typical load-deflection curve generated by the DCB test). Loading on each specimen was continued until a quasi-static crack extension of approximately 5 mm was observed on both longitudinal edges of the specimen. The crack-tip opening displacement was obtained through the displacement data recorded by the INSTRON. A typical load versus crack-tip opening curve is shown in Figure 3-5. The optical microscope was also used to video record the entire event. The crack propagation was recorded almost at every 5-mm increment of its growth, up to the moment when the joint completely failed (i.e., the adherends separated).

37

ASTM D5528 (2007) outlines three methods for calculating Mode I interlaminar fracture toughness, G_{IC}. The methods are (i) the Modified Beam Theory (MBT), (ii) the Compliance Calibration (CC), and (iii) the Modified Compliance Calibration (MCC). Here, the MBT and MCC methods were employed to establish the value of G_{IC} of the adhesive. The MBT applies a correction to the original equation (which is based on the Euler beam theory), since the assumed restrained end of the DCB is not fully restrained in reality. Hence, the modified solution considers the influence of the potential rotation of the so-called cantilevered-end by adding Δ to the moving delaminated length, a (i.e., $a + |\Delta|$). Parameter Δ is determined through the least-square line that is fitted to the data points generated by plotting of the cube root of compliance, $C^{1/3}$, versus a. The following equation is then used to establish the value of Mode-I interlaminar fracture toughness (ASTM, 2004):

$$G_{IC} = \left(\frac{3P\delta}{2b(a + |\Delta|)} \right) \qquad \text{3-1}$$

In the above equation, P is the applied load, δ is the displacement at the location of the applied load; b is specimen's width.

In MCC, a least-square graph of the delamination length normalized by specimen thickness (a/h), as a function of the cube root of the compliance ($C^{1/3}$) is plotted using the advancing crack length (a). The slope of this line is designated as A_1. Mode I interlaminar fracture toughness is then calculated using the following equation (ASTM, 2004):

$$G_{IC} = \frac{3P^2 C^{2/3}}{2A_1 b \, h} \qquad \text{3-2}$$

3.4.3 Mode II and Mixed mode fracture toughness evaluation

The ENF and SLB specimens were loaded in a 3-point flexure by the same Instron 8500+ machine under displacement control loading regime, at a loading rate of 1.5 mm/min (see Figure 3-3 and Figure 3-4). The tests were performed at room temperature. In the ENF specimen, stress

distribution in the adhesive layer is essentially in a state of pure shear, except at the loading point, where some compressive stress would exist.

Mode II critical strain energy (or fracture toughness), G_{IIc}, and mixed-mode (I/II) fracture toughness, G_T (total strain energy release rate), of the adhesive are calculated by the following equations (De Moura, 2008; De Moura et al., 2011; de Moura and Gonçalves, 2014; Wang and Williams, 1992):

$$G_{IIC} = \frac{9\,P^2 a^2}{16\,E\,b^2 h^3} \qquad\qquad\qquad 3\text{-}3$$

$$G_{TC} = \frac{(21a^2 P^2)}{4\,Eh^3} \qquad\qquad\qquad 3\text{-}4$$

The terms appearing in above equations are as described earlier.

3.4.4 Cyclic thermal fatigue test

As discussed earlier, several researchers (e.g. Hu et al, 2013; Campilho, 2017) have identified the cyclic thermal loading as one of the most critical loading schemes that could affect the life-cycle of ABJs. In several engineering applications, ABJs often experience fluctuating temperatures (cold-warm and vice-versa). Several investigators have considered the cycle range of -35 °C to +45 °C (i.e., cold to warm cyclic temperatures) in their studies (Broughton et al., 1999; Johnson and Butkus, 1998). To the best of the author's knowledge, there is no standard or unified heating-cooling test procedure. Most works in this area have followed thermal cycle regimes that a given material would experience under a specific environmental condition of interest, in-service. The specific environmental condition of our interest was the GFRP rehabilitated pipelines. Therefore, the thermal range used in our work is aimed at covering the average high and low temperatures that a pipe would experience in North America (i.e., +45 °C in summers, and -35 °C in winters). In other words, temperature of -35 °C represents the average lowest temperature experienced in

most northern hemisphere climates, while +45 °C represents an average extreme value of service conditions in summers. Note that the elevated temperature is well below the T_g, of the resin, which is rated at a minimum of +60 °C. The cyclic thermal test was conducted within an environmental chamber (Associated Environmental Systems Model ZBHD-205, Benchtop humidity chamber). The chamber is designed to generate and control low and high-temperature environments in the range of -65 °C to +200 °C. The temperature within the chamber was monitored and recorded continually using a thermocouple, controlled by a data-acquisition system (DAQ), hosted by a PC. Figure 3-6 (a) shows the mechanical refrigerator chamber connected to a PC to record the running temperature profile and the real temperature via a thermocouple, and Figure 4-6(b) shows the data with graphic from THERMOLINK program.

Each heating-cooling cycle included four stages, with each stage of heating and cooling lasting 30 minutes. It should also be mentioned that each test started at room temperature as an initial step, and was then, taken to 45 °C, a stage that is not illustrated in the thermal cycle. A typical cycle's details are shown in Figure 3-6.
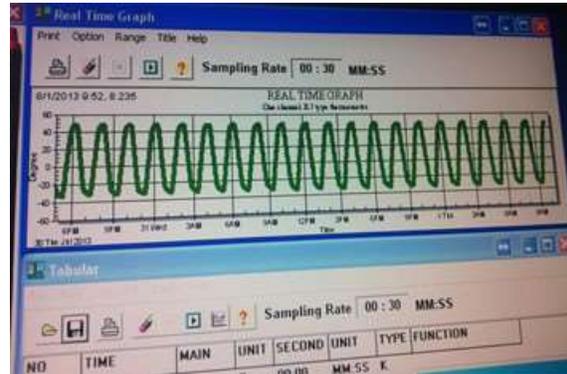
(a)   (b)
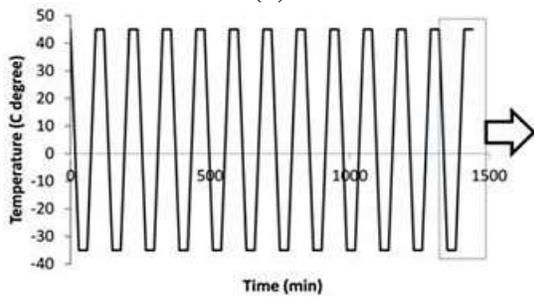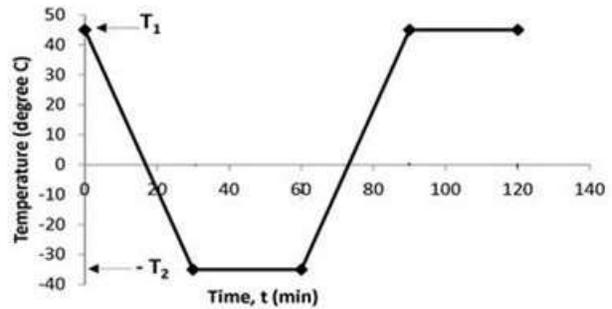
(c)   (d)

Figure 3-6 Test Setup (a) environmental chamber equipped with a PC to control and record the prescribed temperature profile via a thermo-couple, (b) graphic illustration of the data by THERMOLINK program, (c) the applied thermal cycles and (d) schematic of one complete cycle

In total, eight groups of specimens were tested, each having been subjected to a different total number of cycles , as reported in Table 3-1, and then subsequently subjected to mechanical loading (i.e., testing according to ASTM D5528 (2007)). Note that group No.1 includes the baseline specimens that were not subjected to thermal cycling and were later mechanically loaded, as will be further described. Moreover, the humidity was kept between 20% - 30%.

Table 3-1 Specimen groups ID

Group ID	1	2	3	4	5	6	7	8
Number of applied thermal cycles	Zero (baseline specimens)	150	300	450	600	750	900	1000

41

3.5 Experimental Results and Discussion

The experimental data was processed to obtain the degradation in selected material properties as a function of the applied thermal cycles. Stress-strain curves of the neat epoxy and GFRP specimens after having been exposed to the set thermal cycles were established. In addition, the Fourier transform-Raman spectroscopy (FT-Raman) and DSC were conducted on each group of specimens after having been exposed to the set thermal cycles.

3.5.1 Properties of neat epoxy adhesive and unidirectional GFRP

3.5.1.1 Influence of thermal cycles on the mechanical properties

Figure 3-7 and Figure 3-8 illustrate typical load-displacement and stress-strain curves of the neat epoxy and unidirectional E-glass-epoxy composite specimens, respectively.

(a)   (b)
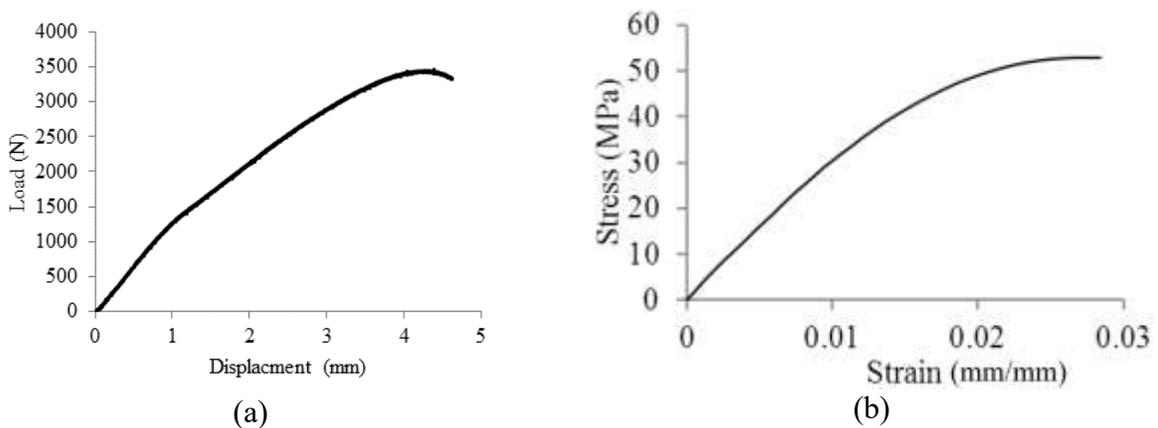
Figure 3-7 Typical (a) load-displacement curve and (b) stress-strain curve of the neat epoxy

(a)

(b)
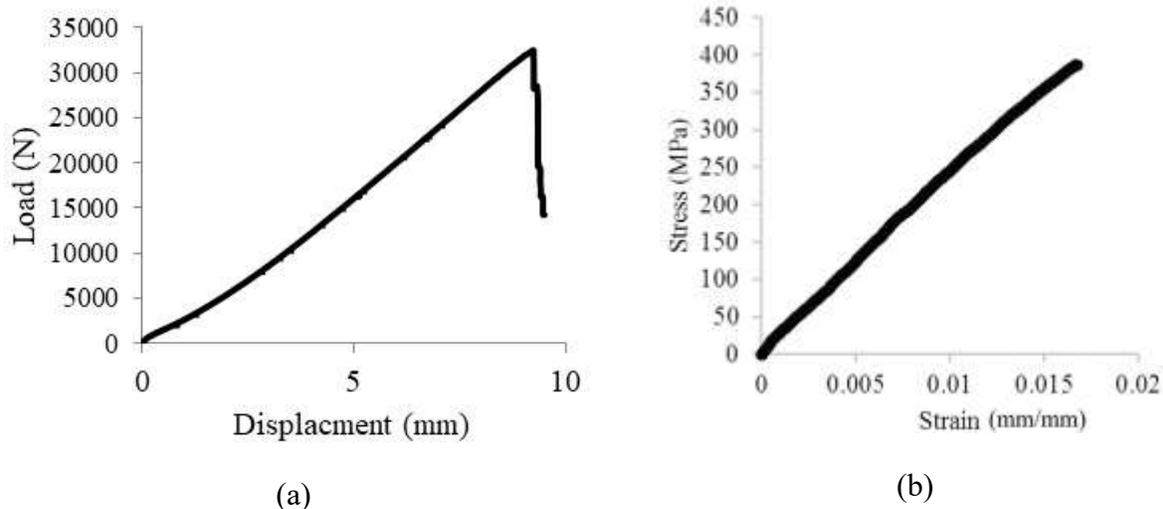
Figure 3-8 Typical (a) load-displacement curve and (b) stress-strain curve of the unidirectional GFRP

The influence of thermal cycling is examined through its effect on the modulus of elasticity, ultimate tensile strength and strain of the materials. Figure 3-9 and Figure 3-10 illustrate the summary of the degradation levels in the modulus of elasticity, ultimate tensile strength and strain corresponding to the ultimate strength, respectively, as a function of the total number of thermal cycles the neat resin and FRP were subjected to. Note that each bar-chart represents the average result of at least four tested specimens.

(a)

(b)
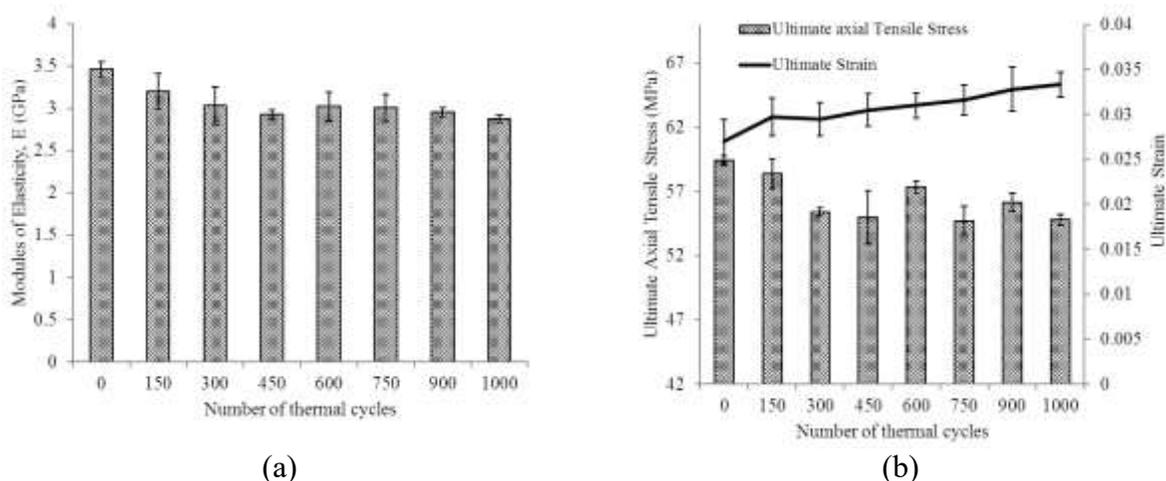
Figure 3-9 Degradation of the mechanical properties of the neat resin as a function of applied thermal cycles: (a) modulus of elasticity and (b) ultimate axial tensile stress and strain

43

(a)   (b)
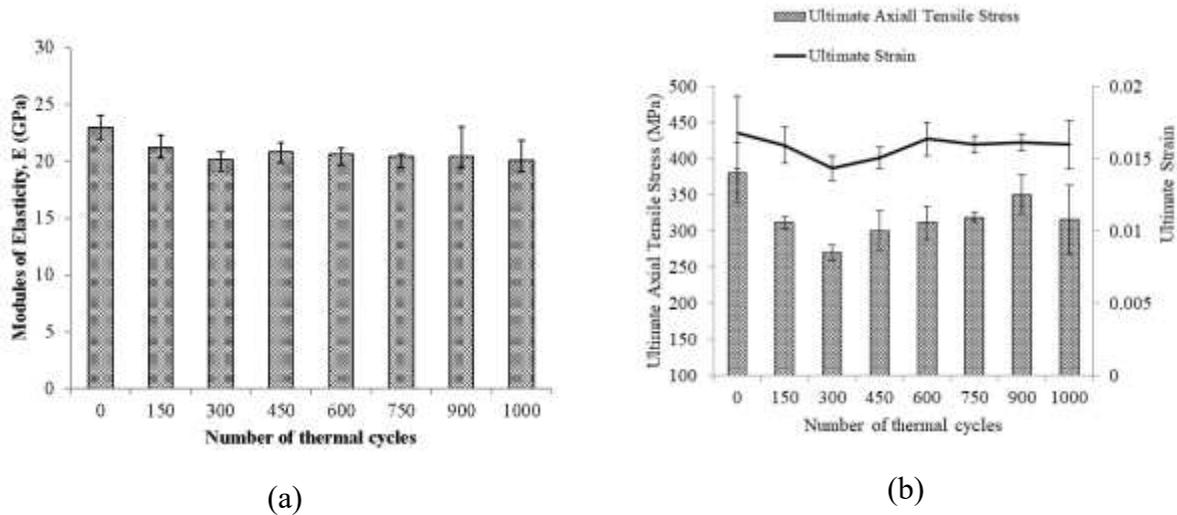
Figure 3-10 Degradation of the mechanical properties of GFRP as a function of applied thermal cycle: (a) modulus of elasticity and (b) ultimate axial tensile stress and strain

Notable degradations in the modulus of elasticity, and ultimate tensile stress and significant softening of the resin response are observed in both the resin and FRP. However, as expected, the decrease in the properties of the resin is more significant than that in FRP. This is because unidirectional FRP's strength and stiffness are fiber dominant properties, as opposed to being matrix dominant. Note that the modulus of elasticity and ultimate strength of the resin were decreased by approximately 17% and 8% after being exposed to the maximum number of applied thermal cycles (i.e., 1000). However, similar levels of degradation (i.e., 16% and 8%, respectively), took place in the specimens at much earlier stages of thermal cycling (at, i.e., 300-400 cycles). The apparent leveling off of the degradation, observable after 300 cycles, may be attributed to the fact that the resin may not have been fully cured, and that its ultimate curing occurring after a few thermal cycles curbed the rate of degradation of its mechanical properties. In other words, it appears that the polymer chains were strengthened after having been exposed to a certain number of cycles, thus becoming more resilient against the subsequent applied thermal cycles. This postulation will be discussed further in the following section.

Moreover, degradations in the modulus of elasticity and ultimate tensile strength of the E-glass FRP after 1000 cycles were approximately 12% and 13%, respectively. Similar to the resin's response, the FRP also experienced greater levels of degradation after 300 thermal cycles (by

44

approximately 12% and 29% in the modulus of elasticity and ultimate tensile strength, respectively) in comparison to those observed after 1000 thermal cycles. Furthermore, an apparent strain hardening of approximately 20% was observed as the number of thermal cycles increased, up to 300 cycles. However, after that stage, the strain capacity of the FRP softened markedly (as much as 25%). The failure modes of the unidirectional specimens were consistent, regardless of the number of thermal cycles the specimen had been exposed to.

3.5.1.2 Influence of the thermal cycles on degree of curing

The phenomenon of apparent improvement in the properties observed after the application of a certain number of thermal cycles is indeed consistent with the findings of an investigation that was conducted on the same resin within our research group a few years ago (see Baftechi, 2008). Moreover, it also corroborates with the findings reported by other investigators (see for instance Kumar et al., 2002; Vašková and Křesálek, 2011; Cabral-Fonseca et al., 2012; Hardis et al., 2013). To gain a better understanding of the effect of thermal cycles on the resin and its composite, and to further explore whether any change in the resin's chemistry was responsible for the observed phenomenon, further exploration was carried out using a Raman spectrometer. The Raman spectroscopy measures the rotational and vibrational transitions in molecules. These features can be used to detect and identify specific changes in chemical bonds of polymers, which could be developed as a result of exposure to thermal cycles. The relative intensity of Raman spectra peaks is directly proportional to the relative and proportional concentration of active molecules of the components of polymers (Ajiboye, 2012; Barbosa et al., 2015; Crawford et al.; Foulc et al., 2005).

Figure 3-10 and Figure 3-11 illustrate the typical variations in the signals obtained from FT-Raman spectroscopy of the epoxy resin and its FRP, respectively, after having been exposed to various numbers of thermal cycles. The spectra look similar for all specimens in the range of 500 to 4000 cm^{-1}, and they follow a similar trend. This would indicate that the chemical structure of the resin did not undergo any major changes after having been exposed to the cycles of heating and cooling. Moreover, all spectra peaks are consistent with those reported in the literature.

However, several peaks are observed in the spectra, which would indicate strong connections of resin's chemical components ⟨structure⟩ (McCreery, 2005). The changes observed in C=C stretching of the benzene ring at 1600 cm^{-1} (asym stretch) and the Raman line at 2860 cm^{-1} are very intense, corresponding to CH$_3$ symmetrical stretching. Also, the observed Raman shift absorption to increased degassing at ~3000 and ~3100 cm^{-1} (see Figure 3-11), is believed to be due to stretching vibration of the secondary amino group associated with the hardener when reacted with the resin. Accordingly, these peaks can be used as a reference for assessing the degree of cure of adhesive, which is indicated by the change in intensity of the peaks, attributed to the epoxide group.
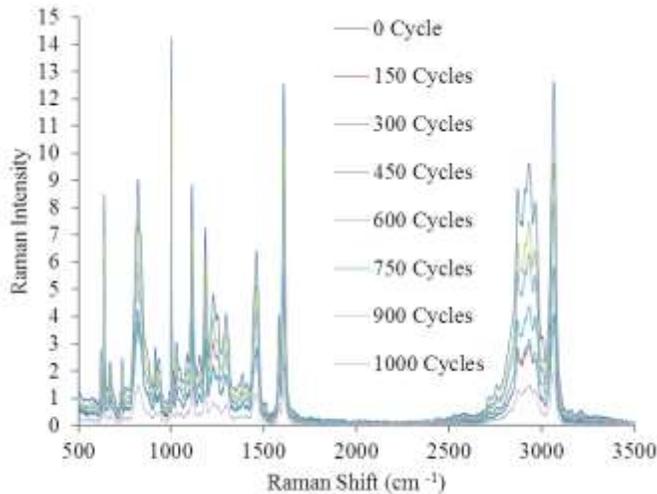
Figure 3-11 FT-Raman spectra of the epoxy resin specimens after having been subjected to various numbers of thermal cycles
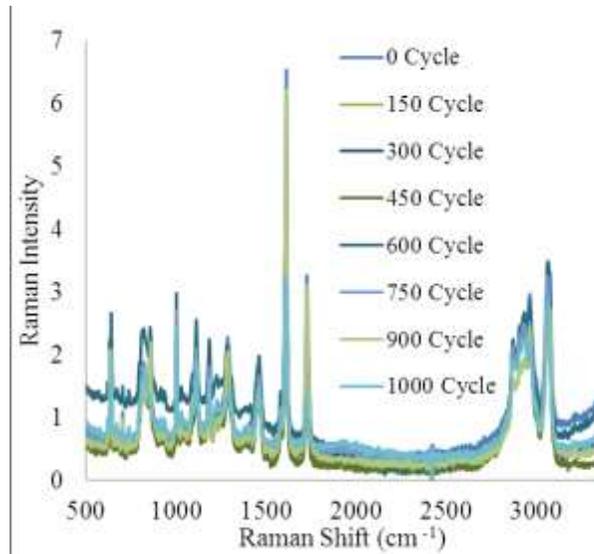
Figure 3-12 FT-Raman spectrometer of the GFRP specimens after having been subjected to various numbers of thermal cycles

Moreover, to explore any evidence of chemical degradation, the relative spectra intensities were also examined. For that, all spectra were scaled with respect to the maximum value (i.e., at 2860 cm^{-1}), as illustrated in Figure 3-13. As mentioned, the 2860 cm^{-1} shift was selected because it is very intense, so that the measurements could be done with high accuracy at that intensity. Moreover, it is not associated with the polymer backbone; therefore, it should not be changing the absolute intensity, even if chemical changes take place in the polymer.
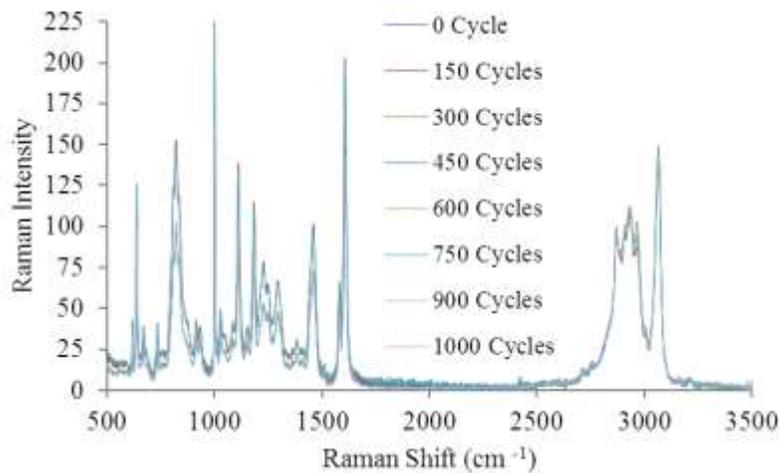
Figure 3-13 Raman spectra of the epoxy resin normalized with respect to line at 2860 cm^{-1}

47

Farquharson et al. (1994) showed that Raman shifts at ~1600 cm^{-1} are due to a polymer's backbone and that their intensity could be diminished as the polymer degrades. In our case, the line at ~ 1610 cm^{-1} does not follow a monatomic decrease as a function of thermal cycles. The signs of curing in such resins are identifiable by the existence of the Raman lines at ~1640 cm^{-1}, reflecting insufficient curing, and the lines at ~1610 cm^{-1}, indicating an increase in curing. Therefore, the variation in the peak ratios would be an indication of further curing of the resin. Examination of the spectra evidence no sign of the ~1640 cm^{-1} peaks as a function of increasing thermal cycles. Therefore, this would indicate that the original samples were already fully cured.

Despite the above-noted results, the nonlinear variation of the mechanical properties remains quite perplexing. To further explore the cause of such a variation, additional Raman spectroscopies were conducted. In this part of the examination, selected groups of GFRP specimens (i.e., groups 1, 5 and 8, those that were subjected to 0, 600 and 1000 thermal cycles), were further examined. The spectra of these specimens were obtained under the isothermal regimes of 20 °C, then heated up to 140 °C, and subsequently cooled to 55 °C, and then allowed to cool down to room temperature (20 °C). Note that the resin T_g was exceeded. The spectra for this part of the examination are illustrated in Figure 3-13. Evidence of very strong bonds are noted at the next shift peaks (i.e., at ~1610, 1720, 2970 and 3070 cm^{-1}).
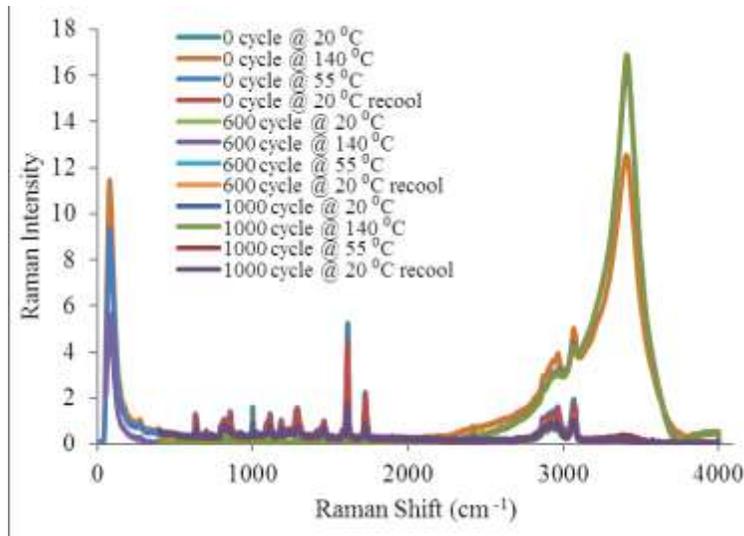
Figure 3-14 FT-Raman spectrum of the GFRP specimens having been initially exposed to various thermal cycles, obtained at various isothermal regimes

As it can be seen, one cannot decipher any significant conclusion from the plots. It should be noted that deciphering the data becomes even more challenging because the curves at each isothermal regime of the specimens subjected to the various thermal cycles virtually fall on top of one another. Nevertheless, C=C multiple bands stretching of phenyl rings are evidence at a strong bond at ~1610 cm^{-1}. As stated earlier, however, the shifts at ~1600 cm^{-1} are due to the backbone of the polymer, and it can diminish in intensity as the polymer degrades. The large emission observed at 140 ºC above ~ 3000 cm^{-1} is an artifact of heating emission from the variable temperature cell; this peak was also observed with no sample present at the same temperature.

To further enhance the variation of the Raman spectra, an attempt was made to show the peaks in a bar-chart format, as illustrated in Figure 3-15(a). Further clarification can be seen by our attempt in presenting the variation of the Raman intensity as a function of the applied thermal cycles, shown in Figure 3-15(b). There seems to be a clear evidence that a reaction (postulated to be due to further curing of the resin) occurred due to the application of thermal cycles (up to 600 cycles). This evidence is clear when considering the variation of the intensity at 1610 cm^{-1} shift, as well as the other selected shifts. This follows the trend observed in the curves illustrating the variation in mechanical properties, as illustrated in Figures 3-9 and 3-10.

(a)   (b)
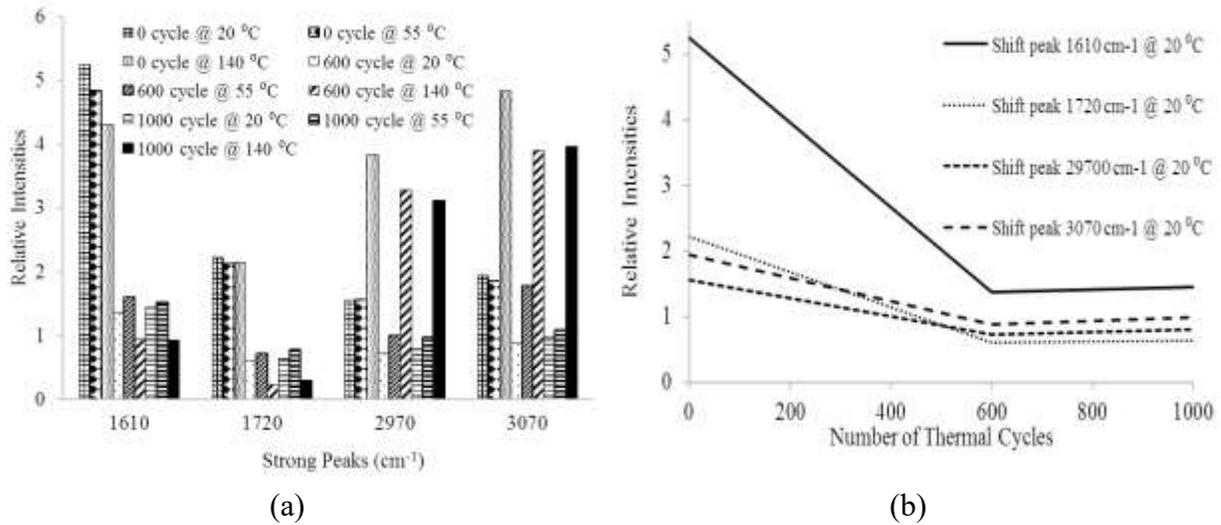
Figure 3-15 Variation of the Raman intensity in the thermally cycled GFRP specimens (a) under various isothermal regimes and (b) variation of the intensity at a specific isothermal regime

3.5.1.3 Influence of the thermal cycles on glass transition temperature (T_g)

The DSC data was processed using the Universal Analysis 2000 software (TA Instruments). Results obtained from DSC thermograms reveal the effect of thermal cycles on the T_g of the resin. The T_g temperatures are evaluated using the inflection point obtained during heating the sample. Figure 3-16(a) illustrates the resulting thermograms of the specimen at different thermal cycling numbers (i.e., the data obtained from the DSC instrument). In addition, Figure 3-16(b) illustrates the change in the T_g of the epoxy after exposure to various number of thermal cycles.
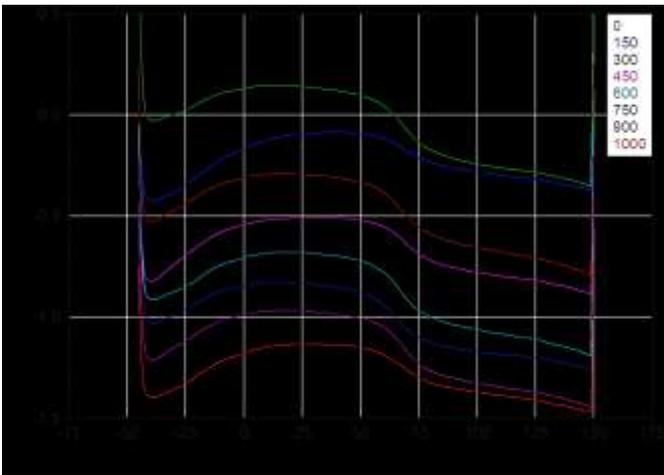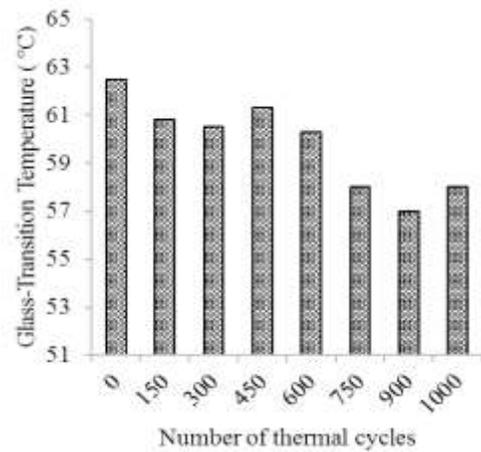
<center>(a)</center> <center>(b)</center>

Figure 3-16 Variation in (a) thermograms of the epoxy resin after undergoing thermal cycling and (b) glass transition temperature as a function of applied thermal cycles

As seen in Figure 3-16(a), thermograms of the epoxy resin after undergoing thermal cycling show a steady heat flow, regardless of the number of cycles applied to the specimens. Figure 3-16(b) shows the glass transition trend as a function of thermal cycles. We observe a slight decrease in T_g as the samples undergo thermal cycling. Interestingly after 450 cycles, there is an increase in T_g value and further reduction in T_g upon exposure to more thermal cycles. This variation is also in concert with the variation seen in the modulus of elasticity and ultimate strength of the resin, as shown in Figure 3-10. A maximum change of 9% in T_g is observed.

3.5.2 Influence of the thermal cycles on Mode I fracture toughness

The results of Mode I interlaminar fracture tests are presented in this section. The fracture failure mechanism and the microstructure of the fracture interface of DCB specimens are also reported and discussed.

3.5.2.1 Fracture toughness

The DCB test results were used to establish Mode I interlaminar fracture toughness, G_{Ic}, of the joint in each group of specimens as a function of the applied thermal cycles. A typical load-

<center>51</center>

deflection curve of one of the baseline specimens is illustrated in Figure 3-5. Mode I fracture toughness curves of two typical baseline specimens evaluated using the MBT and MCC methods are illustrated in Figure 3-17. Typical fracture toughness values obtained by the two method near the transition stage from the initial crack length to the following crack extension lengths are shown in Figure 3-17.
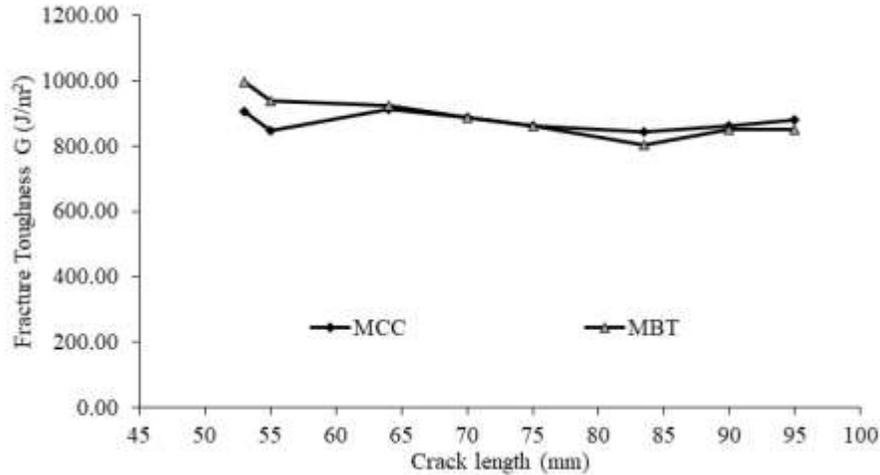
Figure 3-17 Comparison of Mode I fracture-resistance curve (R-curve) obtained from MBT and MCC method for the baseline specimens

As can be seen, results obtained by MBT and MCC methods reveal relatively steady-state crack advancements, with comparable values. The only difference produced by the two methods are the toughness values corresponding to the initial growth stage of the tests. Figure 3-18 illustrates the plateau portion of the crack resistance curves for a typical baseline specimen, and a specimen that was exposed to 600 and 1000 thermal cycles, respectively.
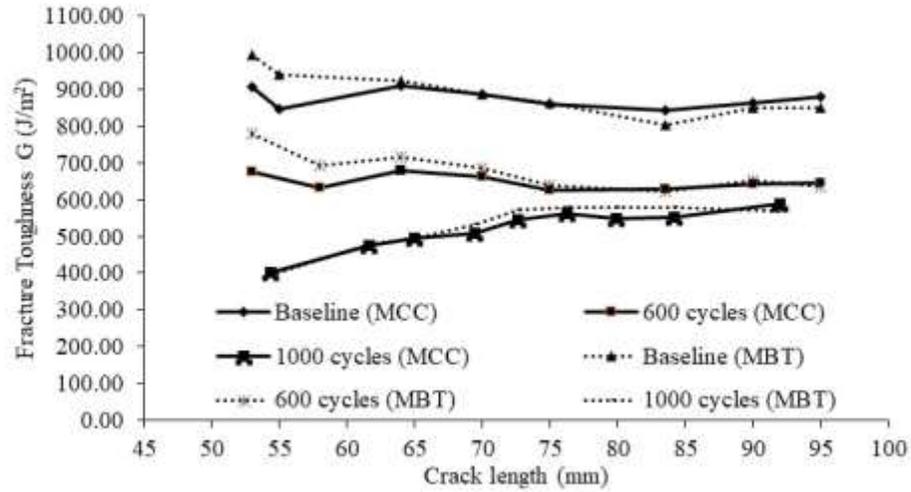
Figure 3-18 Mode I fracture toughness versus crack length obtained by MBT and MCC methods

The variation in Mode I interlaminar fracture toughness as a function of the applied thermal cycles is shown in Figure 3-19. Each bar represents the average value of four tests per specimen category obtained by the MBT.
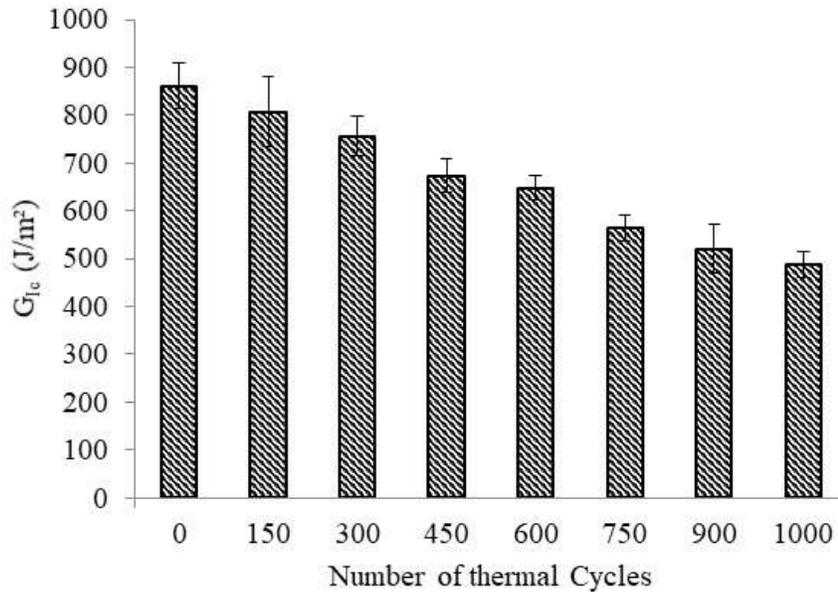
Figure 3-19 Degradation of Mode I interlaminar fracture toughness as a function of applied thermal cycles

As can be seen, the variation and the level of degradation of critical toughness values as a function of applied thermal cycles seems to follow a linear trend. Therefore, following the approach of Hu *et al.* (2013), a simple least-square linear equation is obtained by which one can establish the damage variable corresponding to an applied number of thermal cycles, N.

$$G_{IC} = 862.08 - 0.3801\ N$$

3-5

It should be noted that this fitted equation has a high R² value of 0.9939.

3.5.2.2 Fracture failure mechanism investigation

The investigation into the influence of thermal cycling on the microstructure of the interface was conducted to gain an insight into the resulting failure mechanism in each group of specimens. Several techniques are available for investigating the failure modes of ABJs. The following three techniques were utilized in this study: (i) visual, (ii) stereo optical microscope (SOM) and (iii) scanning electron microscopy (SEM). The resulting failure modes of ABJs are essentially categorized into three modes:

i) Structural failure, which constitutes the internal failure within adherend materials (e.g., actual delamination or fiber-breakage of adherends); in this study, this failure mode was observed to occur mainly in a region adjacent to the adhesive layer.

ii) Interfacial failure, resulting in the separation of one of the adherends from the adhesive layer.

iii) Cohesive failure of the adhesive, which involves the internal failure within the adhesive layer.

Failure of ABJs is desired to occur in the cohesive mode, but often interfacial failure modes are experienced. In this study, the DCB specimens that were exposed to cyclic thermal loading exhibited mainly interfacial type failure, primarily due to degradation of the adhesive's properties as a result of the applied heating and cooling cycles. In addition, it is also believed that the volatility

of the situation is further escalated due to the mismatch in the Poisson's ratios of the adhesive and GFRP adherends.

As for the visually observed failure modes, most of the baseline specimens and those specimens that were subjected to a relatively lower numbers of thermal cycles (150-600 cycles) failed in both cohesive and interfacial failure modes, almost in equal numbers. Specifically, in half of the specimens, the crack propagated cohesively, while in the other half, the crack initially started propagating cohesively, but then it changed its course and propagated within the GFRP/resin interface. On the remaining specimens, the crack started cohesively; however, in some of the specimens (especially those that had undergone a higher number of cycles), the same crack that started and propagated for a certain distance cohesively, diverted from its path and propagated into the interface, and sometime, after a short distance propagating within the interface, it changed its course and propagated into the adjacent GFRP layer (in some cases, even propagated into the second layer adjacent to the side interface.) This phenomenon might have been due to increased degradation of the resin and its effect on the possible voids that might have existed within the resin.

Typical fracture surfaces of the DCB specimens are shown in Figures 3-19 and Figure 3-20. The failure surface observed in the baseline specimen is also shown for comparison. Comparison of the fracture surfaces of the specimens subjected to various thermal cycles reveals an increase in the unevenness of the surfaces as a function of increasing thermal cycles. This unevenness is attributed to the degradation and sometimes disintegration of the resin (although difficult to capture by photography, the phenomenon can be discerned from Figure 3-20 (f) and (h)).
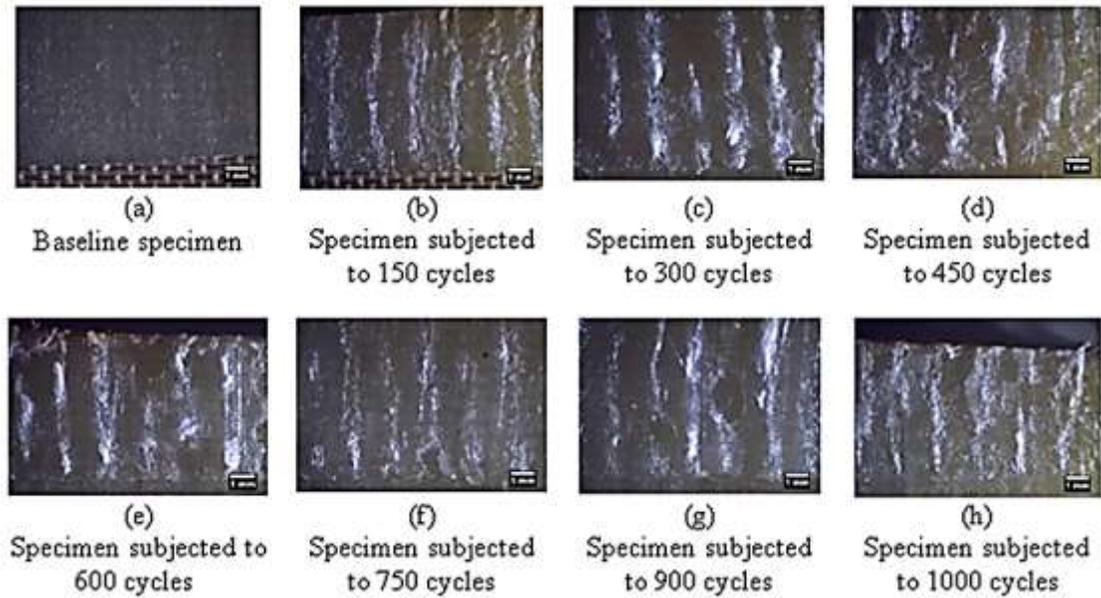
Figure 3-20 Stereo optical microscopy (SOM) images of the fracture surfaces

Figure 3-21 shows the SEM images of the failed surfaces. SEM images show a higher resolution of the fractured surfaces' topography. Various failure mechanisms, such as cohesive failure, interfacial failure, and delamination of the adherends (fibers pull-out and breakage) could be observed. The crack path can be traced by noticing the debonded fibers. Comparison of the failure surface of the baseline specimens (Figure 3-21 (a)) and that corresponding to the specimen that underwent 1000 thermal cycles (Figure 3-21 (d)) clearly reveals the disintegration of the adhesive due to thermal cycling. Moreover, relatively straight micro-cracks are observed at the failure surfaces of specimens that were subject to lower thermal cycles, while the microcracks were observed to be relatively much rougher on the surfaces of specimens that were subjected to higher thermal cycles.
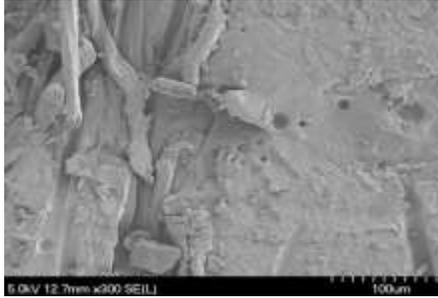
(a) Baseline specimen
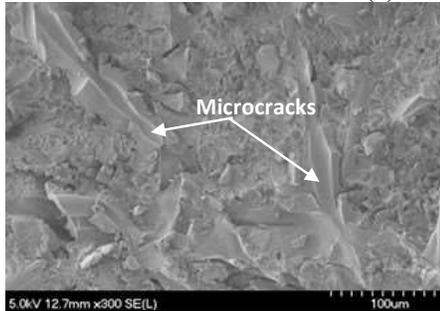
(b) Specimen subjected to 450 cycles

(c) Specimen subjected to 450 cycles
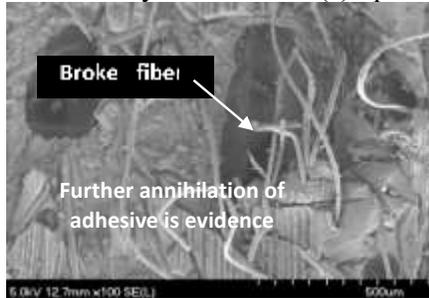
(d) Specimen subjected to 1000 cycles

Figure 3-21 SEM images of the fracture surface of various groups of tested DCB specimens

3.5.3 Mode II and mixed mode fracture toughness

The influence of thermal cycling is further examined through its effect on Mode II and mixed-mode fracture toughness values. The load-displacement curve results obtained from Mode II (ENF) and mixed-mode (SLB) fracture tests are illustrated in Figure 3-22.
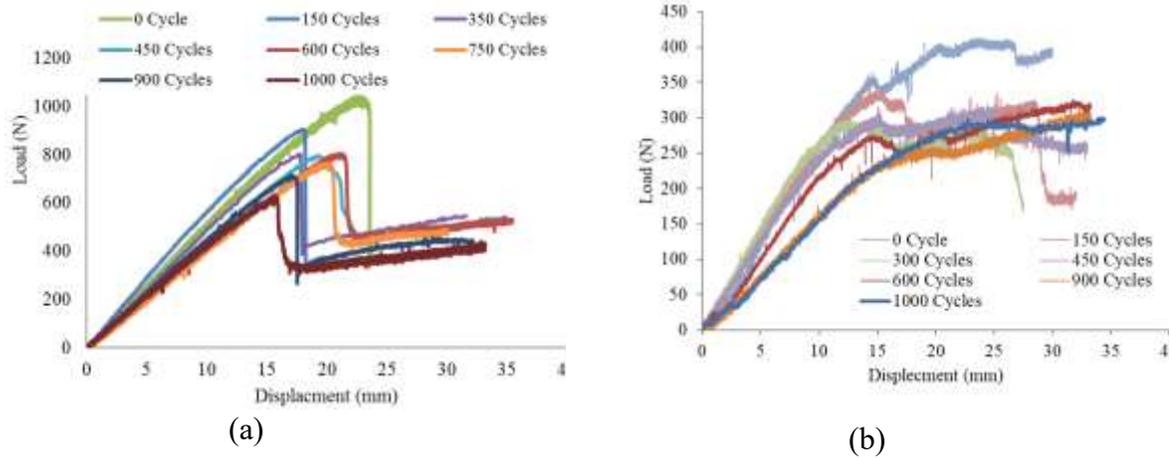
Figure 3-22 Load-displacement curves of (a) Mode II, ENF specimens and (b) mixed-mode I/II, SLB specimens

Equations 3-3 and 3-4 are used to establish the fracture toughness values, G_{IIc} and G_{Tc} for each group of specimens. The results, as a function of the applied thermal cycle numbers, are illustrated in Figure 3-23. Note that each bar represents the average value of a minimum of three tested specimens.
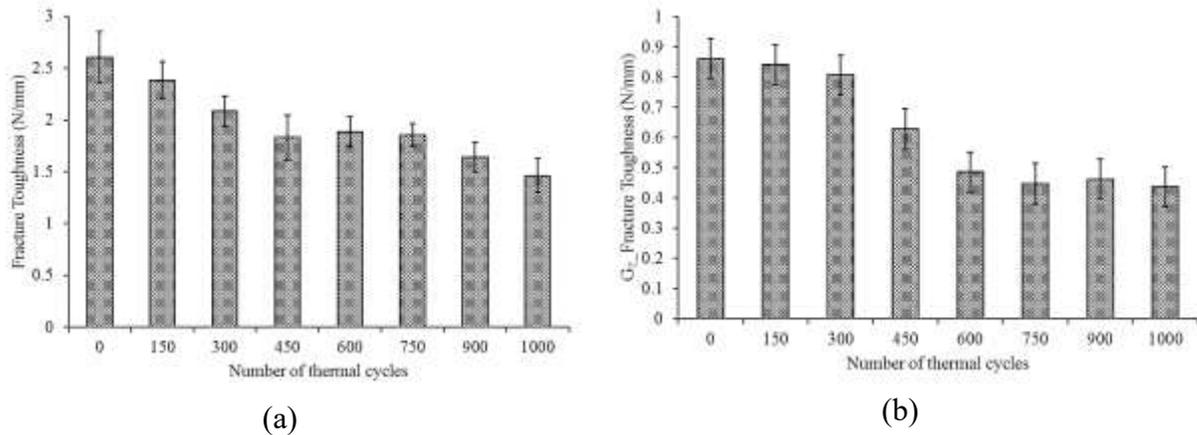
Figure 3-23 Degradation of the critical energy release rate as a function of loading cycles, (a) Mode II and (b) mixed-mode I/II

As can be seen, G_{IIc} and G_{Tc} of the ABJs have been significantly degraded as the applied thermal cycles are increased. The degradation of approximately 42% and 48% in G_{IIc} and G_{Tc}, respectively, are noted after exposure to 1000 cycles. As it can also be noted, the degradation in Mode II fracture toughness of the adhesive as a function of the increasing applied thermal cycles does not occur in

58

a linear fashion. Adhesive's fracture toughness degrades linearly up to reaching 450 cycles, after which the toughness remains undegraded. It is believed that this leveling off response is due to post-curing of the polymers as a result of the applied heating cycles. Once full during is achieved, the toughness becomes further impacted by the additional thermal cycles. Moreover, the mixed-mode fracture toughness degradation occurs in a relatively slow pace (up to further 300 exposure cycles), and then the degradation takes a relatively faster linear pace (up to 750 exposure cycles), after which it remains relatively unchanged as the number of thermal cycles is increased.

3.6 Summary and Concluding Remarks

An investigation was carried out to establish the influence of thermal cycles on the mechanical properties of a widely used epoxy resin, which is also used for bonding similar and dissimilar materials. For that, various ABJ configurations, namely DCB, ENF and SLB, were considered. The following conclusions are drawn based on the investigations conducted:

i. Exposure to thermal cycles caused notable degradations in the stiffness and strength of the epoxy resin. The modulus of elasticity and ultimate tensile strength of the resin were degraded by approximately 17% and 8%, respectively, after exposure to 1000 thermal cycles.

ii. While a resin's properties are not supposed to impact the axial strength and stiffness of the unidirectional fiber-reinforced composites that are formed by the resin significantly, that was not the case in this investigation. In fact, mechanical test results revealed degradations levels of 12% and 13%, respectively, in the modulus of elasticity and ultimate tensile strength of the unidirectional epoxy specimens that were investigated in this study. Interestingly, from the perspective of the effect on strain, the FRP's response slightly hardened as thermal cycles were increased (up to 300 cycles), after which its response softened significantly (by as much as 25%) as the thermal cycles increased.

iii. The FT-Raman spectra obtained for the resin specimens that were exposed to various numbers of thermal cycles showed similar characteristics. An in-depth investigation

conducted on some specimens tested under various isothermal regimes showed a variation in the intensity of the Raman spectra at lower thermal cycles; however, the intensity in resin specimens that were exposed to 600 and greater numbers of thermal cycles leveled off.

iv. A maximum decrease in the T_g of 9% was observed in the resin as a result of the applied thermal cycling. The change in T_g was in concert with the observed variation in the stiffness and strength of the resin.

v. The resulting degradation in the fracture toughness property as a function of the applied thermal cycles was observed to follow a linear trend. Therefore, a simple Equation 3-5 was developed by which the degradation in Mode I of the ABJs could be established.

vi. The resulting thermal degradation affected the crack propagation path developed as a result of the applied mechanical loading. In other words, the initial crack, which started propagating in a cohesive manner, altered its path in ABJs whose adhesive was degraded by the thermal cycles. As the number of applied thermal cycles increased (i.e., resin degradation increased), the crack changed its course and, in some cases, traveled into the adjacent plies, since the resin forming the adherends plies was also degraded as the result of the thermal cycling.

vii. Degradation of the resin led to fiber pull-out and fiber-breakage in the ABJs that were first thermally cycled and subsequently subjected to mechanical loading. At times, total disintegration of the resin was also observed through microscopic evaluation.

viii. Mode II fracture toughness of the adhesive was degraded more or less linearly as a function of the applied cycles. However, the mixed-mode fracture toughness degradation started at a relatively slower pace in specimens that were subjected up to 300 cycles. However, the degradation followed a linear trend in those specimens that were subject to the greater number of thermal cycles (up to 750 cycles). The degradation remained relatively unchanged in specimens that had undergone thermal cycles greater than 750 cycles.

Chapter 4: Numerical Analysis of the Response of Adhesively Bonded Joints under Thermal Fatigue

NOTE: A major portion of this chapter has been published in the Journal of Strain Analysis for Engineering Design, Vol.53,7: pp.504-516. (Mohamed and Taheri, 2018)

4.1 Introduction

This chapter presents details of a modeling strategy that is used to assess the response of ABJs (DCB, ENF and SLB specimens) to different number of thermal cycles, as well as the subsequent mechanical loading. More details on implementation of the CZM in ABAQUS are presented, and the results obtained from the FEA are discussed.

4.2 Problem Statement

The responses of the joints are simulated using the CZM approach, using the commercial FEA code, ABAQUS. The degradation of the joints is simulated as a function of time and applied thermal cycles number using a damage parameter that accounts for both static and thermal fatigue resulted in damages. Subsequently, the effect of mechanical loading on the degraded joints is simulated. The numerical results are compared against experimental results.

4.3 Finite Element Mesh and Boundary Conditions

ABAQUS FE software was used to simulate the response of DCB, ENF and SLB specimens that were subjected to the series of thermal cycles as described in Chapter 3. As briefly stated earlier, ABAQUS has many features and modules, effectively facilitating simulation of the response of ABJs, including the availability of several CZMs. A 2D plane-strain FE model was constructed to investigate the influence of the parameters that affect the fracture response of ABJs. Figure 4-1 shows the plane strain mesh configuration and boundary condition for (a) DCB, (b) ENF and (c) SLB model. For the DCB specimen, a vertical displacement was applied to the nodes corresponding to the locations, where the actual specimens were attached to the loading blocks during each test. The boundary conditions are shown in Figure 4-1 (a). The 2D four-node plane-

strain quadrilateral element with reduced integration and hourglass features (element CPE4R) of ABAQUS was used for modeling the adherends. The elements forming the adherends were connected with four-node cohesive (COH2D4) elements, representing the bulk adhesive region.

(a)

(b)

(c)
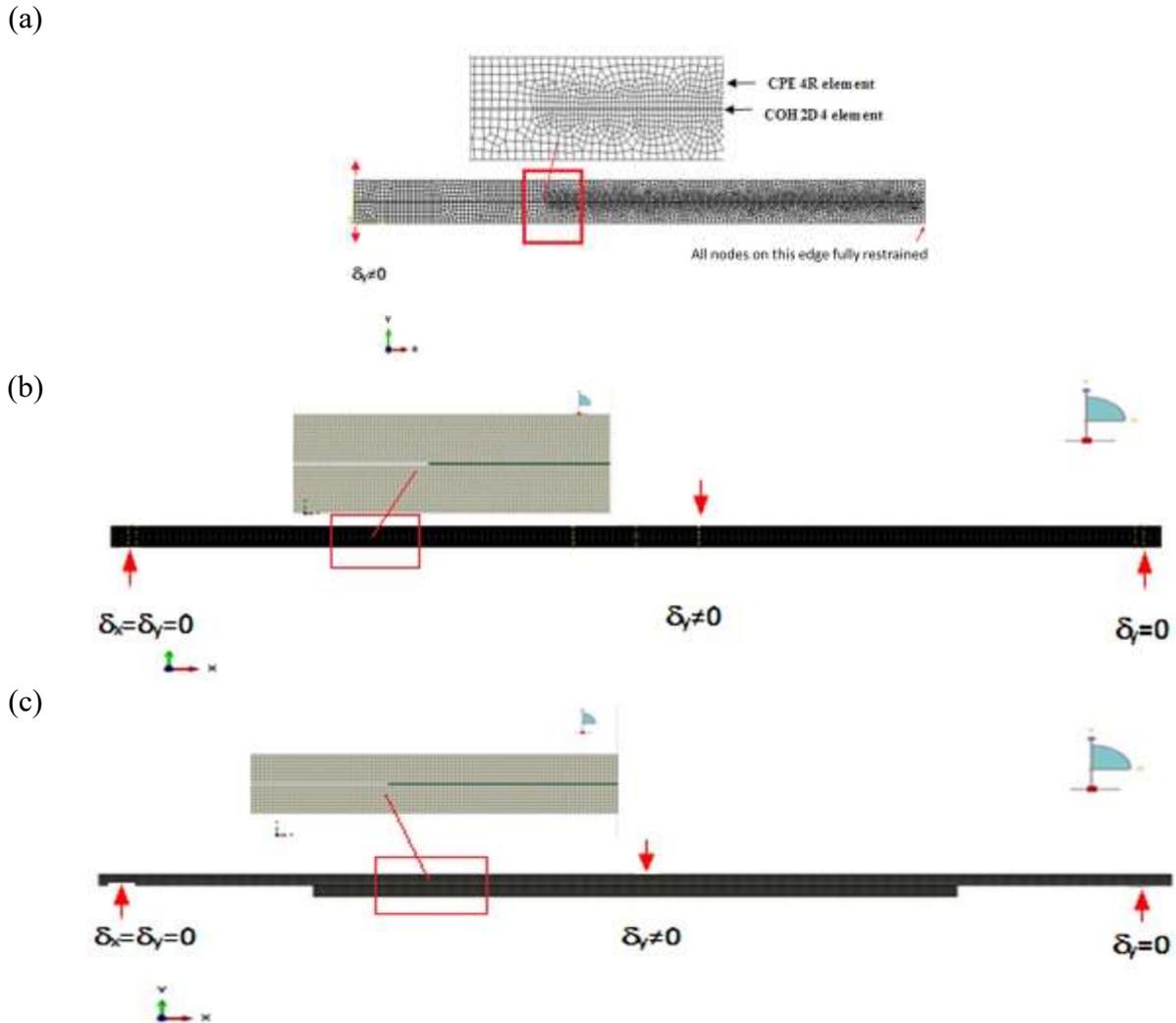
Figure 4-1 The plane strain mesh configuration and boundary condition for (a) DCB, (b) ENF and (c) SLB model

A mesh convergence study was carried out to establish a mesh that would result in reasonably accurate results, without expending huge CPU time. The mesh refinement ensured that the cohesive zone (CZ) elements had an optimal size, so that a converged toughness value could be attained along with a reasonable CPU time. The mesh shown in the figure was established after a series of mesh refinement to reach a convergent result. Note that the CZ (which modeled the

adhesive layer) was modeled by a single layer of cohesive elements through-the thickness. Detail of the size of the cohesive element will be discussed in the following section. The material properties of the adherend and adhesive used in the analyses are reported in Table 4-1. Note that the thickness noted in the table is that of each layer of FRP (lamina) forming the laminate (i.e., the thickness of one of the eight layers forming each adherend).

Table 4-1 Material properties of the adherends and adhesive

Material	Modulus of elasticity (GPa)		Poisson's Ratio		Shear Modulus (GPa)		Thermal expansion coefficient $(10^{-6}/\ ^\circ C)$	
	E_{11}	$E_{22}= E_{33}$	$\upsilon_{12} = \upsilon_{13}$	υ_{23}	$G_{12} = G_{13}$	G_{23}	α_1	$\alpha_2 = \alpha_3$
E glass/epoxy	23.5	5.6	0.25	0.428	3.7	3.28	6.34	20
laminate adherends	Ply thickness =0.4375 mm							
Epoxy	3.5		0.35		0.4		85	
adhesive	Epoxy thickness =0.2 mm							

Notes: the subscripts refer to the local axis used to identify fiber orientation →1- runs along the fibers, 2- runs orthogonal to the fibers, 3- runs through-the-thickness.

4.4 Use of the CZM in ABAQUS

ABAQUS provides users with options to input their own material properties and interfacial parameters within its CZM modeling environment. Once the user implements the related constitutive and/or interface models, they then become an integral part of ABAQUS. A Flowchart of the finite element procedure and implementation of the CZM in ABAQUS is shown in Figure 4-2.
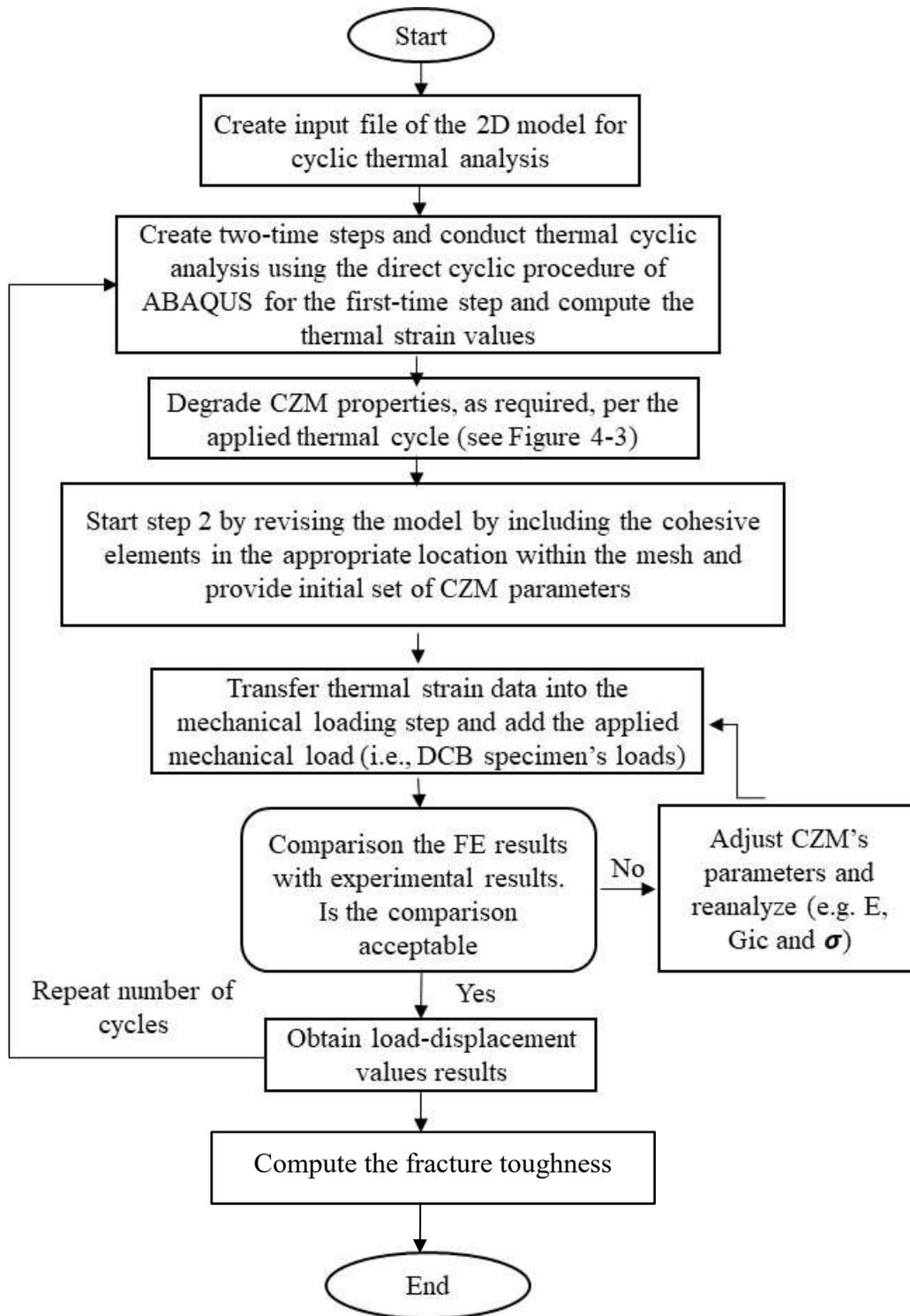
Figure 4-2 Flow chart of the finite element procedure and the method implementation of the CZM in ABAQUS

It should be noted that despite the fact that the entire length of an adhesive interface in the DCB specimen is discretized by the cohesive element, nonetheless, one must first establish the length of the CZ, l_{cz}. This length establishes the distance from the crack tip to the point where the maximum cohesive traction is attained. This length usually spans between one to two millimeters long (in some cases, it could be even shorter). The following equation has been used by several researchers for establishing the length (Turon et al., 2007):

$$l_{cz} = M \cdot E \frac{G_c}{\tau_o^2}$$

4-1

where M is a multiplier parameter that depends on the CZ theory that is used; E is the Modulus of elasticity of the adhesive; G_c is the critical strain energy release rate of adhesive, and τ_o is the peak traction/stress of the adhesive. The value of M ranges from 0.21 to 1.0, as used by various researchers. In this work $M=1$ has been assumed (Turon et al., 2007). Several investigators (Ashcroft et al., 2010; Turon et al., 2007) have shown that the CZ length established accordingly could produce accurate overall results. Moreover, as also suggested by the researchers, a minimum of three elements should be used to discretize the zone.

Following the suggested schemes, two sets of CZ mesh sensitivity analyses were conducted. The first set examined the influence of the CZ length, while the second set of analyses investigated the optimal size of the elements that should be used within the CZ to obtain the best results. The above equation produced a CZ length of 0.86 mm; however, for simplicity, CZ lengths of 1 mm, 1.5 mm and 2 mm were investigated. Various element lengths (i.e., 0.3 mm, 0.5 mm, 1 mm and 2 mm) were considered within each selected CZ length. Our results indicated that element size of 0.5 mm within a 2-mm long CZ could provide accurate results in an optimal manner. Therefore, these values were used to construct the mesh used in all FE analyses reported in this study.

As alluded to earlier, the accurate evaluation of the cohesive parameters and material properties measured by testing of the bulk adhesive are essential for accurate modeling of the response of

ABJs. A suitable damage evolution law, which could describe the rate of degradation of a material's stiffness upon initiation of the damage, is required when implementing a CZM. Therefore, one would also require a suitable damage initiation criterion. Among the CZM models, the linear elastic/linear softening (bilinear) model is the simplest and also the most commonly used one. This model is relatively straightforward to use, and it has been demonstrated to produce fairly accurate results. Moreover, the most commonly used relationship for predicting the development of a fracture is the power law relationship, represented mathematically by Kenane and Benzeggagh (1996, 1997) , which is used here to represent the damage growth:

$$\left(\frac{G_I}{G_{IC}}\right)^{\alpha} + \left(\frac{G_{II}}{G_{IIC}}\right)^{\alpha} + \left(\frac{G_{III}}{G_{IIIC}}\right)^{\alpha} = 1 \qquad \text{4-2}$$

Mode II fracture energy of the epoxy used in this investigation was also evaluated. Note that if the crack tip experiences Mode I fracture only, then by default Mode II and III toughness values would be null, and the equation would be used accordingly, the exponent α value set as 2. The critical strain energy density values are then input into ABAQUS. The cohesive baseline properties of the interface used in the CZM were calibrated based on the experimental results.

The calibration was done by adjusting the effective parameters of the model (e.g. K, G_C and $\boldsymbol{\sigma}$), such that the FE-simulation results matched those of the experiments (ABAQUS, 2014).

In the bilinear cohesive model ABAQUS require the following input parameters

1- Undamaged elastic response, E_{nn}, E_{ss} and E_{tt}
2- Damage traction separation for the initiation, criterion $\boldsymbol{\sigma}_{nn}$, $\boldsymbol{\sigma}_{ss}$ and $\boldsymbol{\sigma}_{tt}$
3- Damage evolution failure, mixed mode behavior= BK, Power =η G_{IC}, G_{IIC} and G_{IIIC}.
4- The adhesive thickness h_{eff}.

An isotropic behavior was assumed to simplify the analysis; in other words, the values of the above-mentioned parameters were kept unchanged during the analysis.

In summary, the value of interfacial strength for a given fracture mode corresponds to the peak traction value obtained for that fracture mode. The value of interfacial strength governs the onset of damage. Considering a Mode I fracture, once the damage is initiated, the joint stiffness is gradually reduced as the damage propagates. In a general state, the elastic stiffness of the interface in the normal and two tangential directions can be related to the elastic stiffness and thickness of the neighboring substrates. The damage evolution procedure adopted in ABAQUS is as follows. First, a scalar damage variable, D, is used to represent the overall damage scale in the material, monotonically. This variable also captures the combined effects of all active load-induced mechanisms. This variable initially takes a value of zero, and evolves after the initiation of damage, and increases to 1.0, at which stage the complete failure of the ABJ is assumed to have occurred. Thus, the post-initial damage response (or the so-called "current stress state"), can be represented by the following equation Campilho (2017), ABAQUS, (2014):

$$\sigma_{max} = (1 - D)\, \sigma_{max}^0 \qquad\qquad \text{4-3}$$

where σ_{max}^0 and σ_{max} are the tractions (strengths) in the virgin (i.e., D=0) state and at any (i[th]) cycled state, respectively, as pictorially illustrated in Figure 4-3.

The approach adopted in this study is based on degrading the material parameters used in the CZM, which is done as a function of increasing number of thermal cycles. In other words, the material is assumed to degrade gradually as it endures increasing thermal cycles, which is what happens in reality (Sugiman et al., 2013c). Material degradation is achieved by adjusting (degrading) the fracture toughness of the resin according to the regimes shown in Figure 4-3.
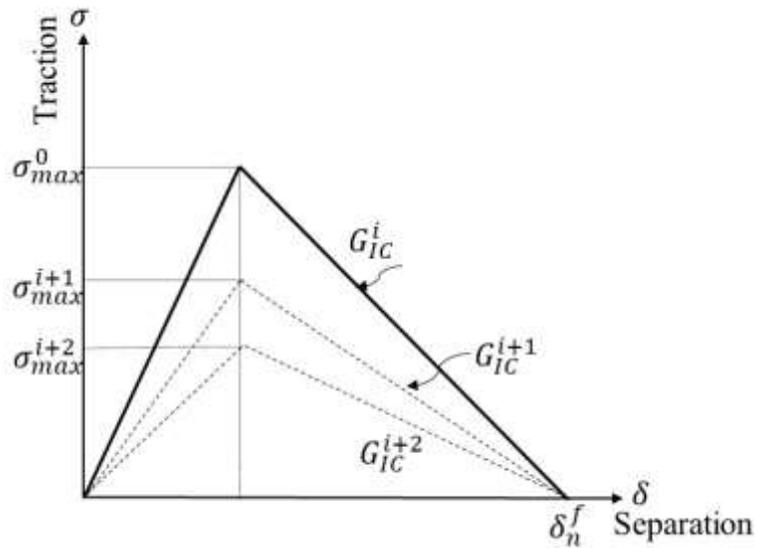
Figure 4-3 Schematic of degradation regimes of the interface properties of an ABJ due to cyclic thermal loading

Sugiman et al. (2013a, 2013b, 2013c) demonstrated the ability to take account of the effects of the damages caused by the thermal cycling and that arising as a result of the mechanical loading on the CZM parameters. Accordingly, the overall combined damage variable can be represented by the following relationship (Yang et al., 2004):

$$D_{tot} = D_{th} + D_m$$
4-4

where D_{tot} is the total damage variable, D_{th} and D_m are the damage variables associated with the thermal cycles (fatigue) and the applied mechanical load (i.e., during DCB toughness testing), respectively.

There are various approaches for defining the damage parameters; an effective method commonly used is degrading the interface strength or stiffness in a rational manner. Here, we assume that the cohesive interface properties (i.e., the stiffness and strength) are degraded as a function of the applied thermal cycles and increase in the mechanical loading, as schematically illustrated in

Figure 4-3. In the figure, σ_i (in which i = 1, 2, 3 . . .), refers to the interface strength at various stages of degradation, and G_c^i represents the value of the critical strain energy release rate at each stage. In ABAQUS, the field output terminology, SDV, is used to represent the thermal fatigue damage, while SDEG denotes the overall scalar stiffness degradation resulting from the damage induced by the mechanical load. As illustrated in the flowchart shown in Figure 4-2, the fatigue damage law was implemented in ABAQUS, and it was used for all specimens that underwent thermal cycles.

The overall damage variable is also accompanied by an evolution law that accounts for the gradual damage that occurs during the thermal cycling stage. Several formulations have been proposed for accounting for such physical degradations; here, the traction-separation response is incorporated to quantify the evolution of interface degradation (see Figure 4-3 for a graphical presentation of the phenomenon). In other words, the evolution process is accounted for by implementing a damage parameter, $\frac{dD}{dN}$, representing the rate of change of damage (D) per cycle N in the adhesive, which is expressed by the following equation (ABAQUS, 2014)

$$\frac{dD}{dN} = \left(1 - \frac{\sigma_{max}}{\sigma_{max}^0}\right) \qquad \text{4-5}$$

Where σ_{max}^0 and σ_{max} stand as defined previously. It should be noted that the simulations were conducted in two steps but within a single FE run. The first step entailed the application of the cyclic thermal load to the FE model using the direct cyclic technique of ABAQUS (Du et al., 2006; Maitournam et al., 2010). This was followed by the application of the mechanical loading, mimicking the DCB test. The procedure followed is briefly described below.

The variation of temperature within each thermal cycle (as illustrated in Figure 3-5) was provided to the software in a tabular form. The resulting stresses calculated by ABAQUS were stored so that they could be superimposed to the stresses caused by the displacements that were imposed on the specimen during the DCB test. In the first step of the analysis (i.e., the thermal analysis), the

69

quasi-static analysis scheme of ABAQUS was used, which included a combination of Fourier series and time integration. The direct cyclic procedure with a fixed time increments of 0.25 sec., was used (thus, resulting in a total of 120 increments describing each segment of the thermal cycles shown in Figure 3-5(d)). The number of terms for the Fourier series and the maximum number of numerical iterations was set at 40 and 100, respectively. The second step, which constituted the mechanical loading portion of the analysis, consisted of applying the equivalent displacement that was implemented in the DCB test to the model, and superimposing the resulting stresses to those that were the outcome of the cyclic thermal loading, which was stored earlier.

4.5 Finite Element Predicted Results

4.5.1 Mode I fracture response (DCB specimen)

The comparison of the load-displacement response of a typical specimen (in this case, the baseline specimen), obtained by FE simulation is compared to the experimental results, as illustrated in Figure 4-4. As can be seen, good comparisons are produced between the experimental and numerical results for both the baseline (virgin) specimens, as well as for the specimens subjected to the maximum number of thermal cycles. Comparison of the results exhibits the degree of accuracy of our FE simulation. Figure 4-5 illustrates the variation of damage index as a function of the thermal cycles. Please note that the damage indices include the effect of both the thermal and monotonic loads. As can be seen, the trend in degradation is also somewhat linear.
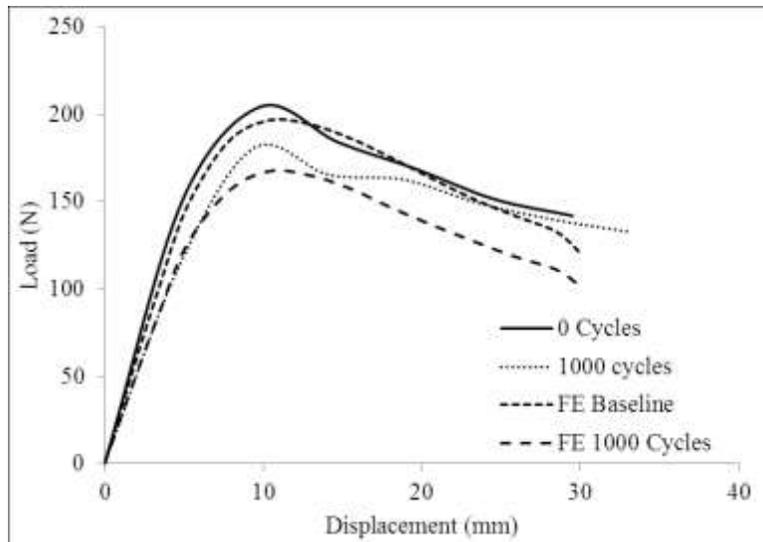
Figure 4-4 Comparison of the experimental and FE simulation results for baseline specimen
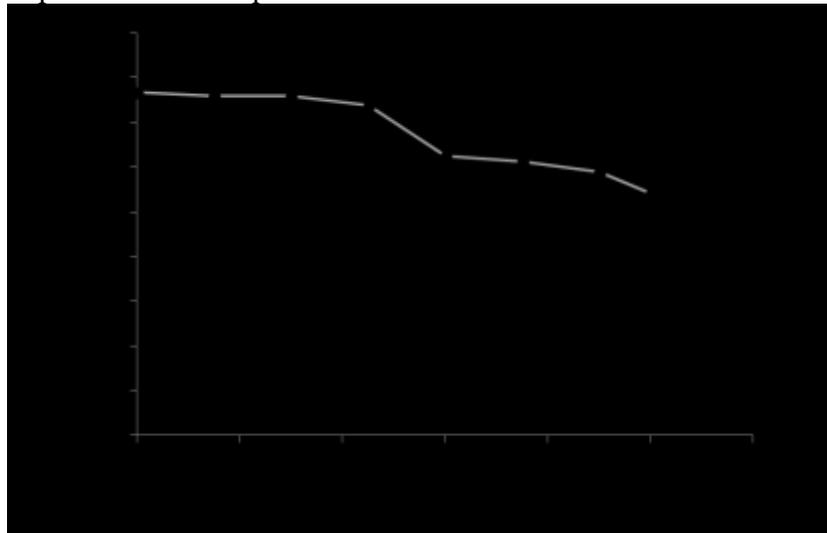
Figure 4-5 Damage index (SDEG) as a function of the thermal cycles

4.5.2 Mode II fracture response (ENF specimen)

The load-displacement curves obtained from the experiment and FE simulation are illustrated in Figure 4-6. Interestingly, the finite element results, which are usually stiffer than the actual response (i.e., experimental results), are less stiff in this case. Nevertheless, the total fracture energy (G_{IC}) calculated by the FE is very similar to that exhibited experimentally. It should be noted that in general, results obtained by the finite element method are stiffer than the actual response. However, in this case the response does not follow the usual trend. The results shown

71

in Figure 4-6 reveals good agreement between the FE and experimental results along the linear segment of the load-displacement curve; however, there is a sudden drop in the experimental curve, potentially due to a sudden cracking, which was not be captured by the simulation.
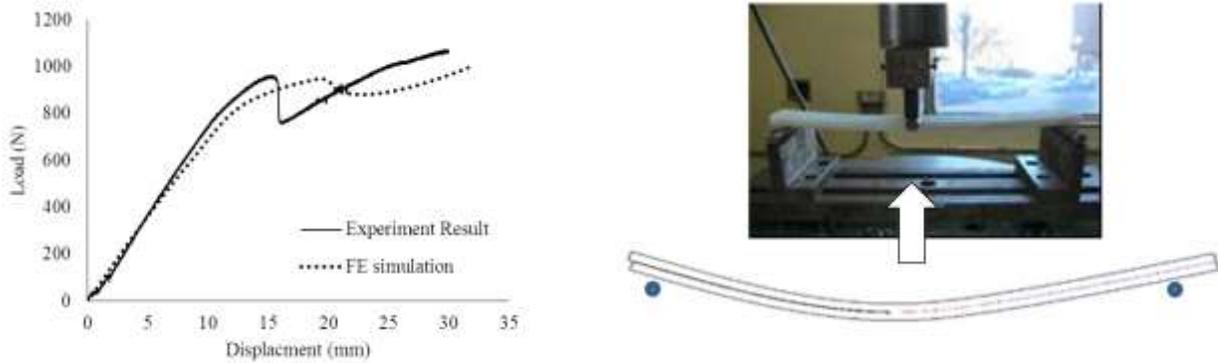
Figure 4-6 Comparison of the load-displacement results and dislocated shapes produced by the FE simulation and experiment for the ENF test

Distribution of the damage index (SDEG), which is the variable signifying development of failure in the adhesive interface, are shown in Figure 4-7 for the ENF specimen. SDEG's distribution within a modeled region identifies the failed segment, as well as crack propagation direction (see below).
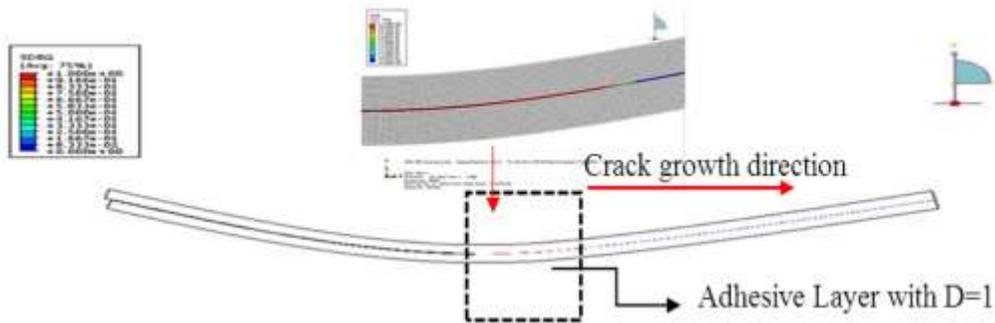
Figure 4-7 Contour variable distribution of damage index (SDEG) for ENF

Moreover, variation of SDEG's distribution within the bondline of ENF specimens that underwent various thermal cycles are shown in Figure 4-8. The SDEG signifies a scalar stiffness degradation of the cohesive elements. As stated earlier, the SDEG variable ranges from 0 to 1; 0 indicates no damage

is present, 1 signifies complete failure of the cohesive element, and a value in between signifies the relative level of damage. As can be seen in the figure, by increasing the number of thermal cycles from 0 cycle (i.e., the baseline specimen) to 1000 cycles, SDEG indices increase, each curve representing the result of degradation for a given cycled specimen, which is captured after the specimen was subjected to the ENF tests. A notable degradation is evident as the number of cycles increases.
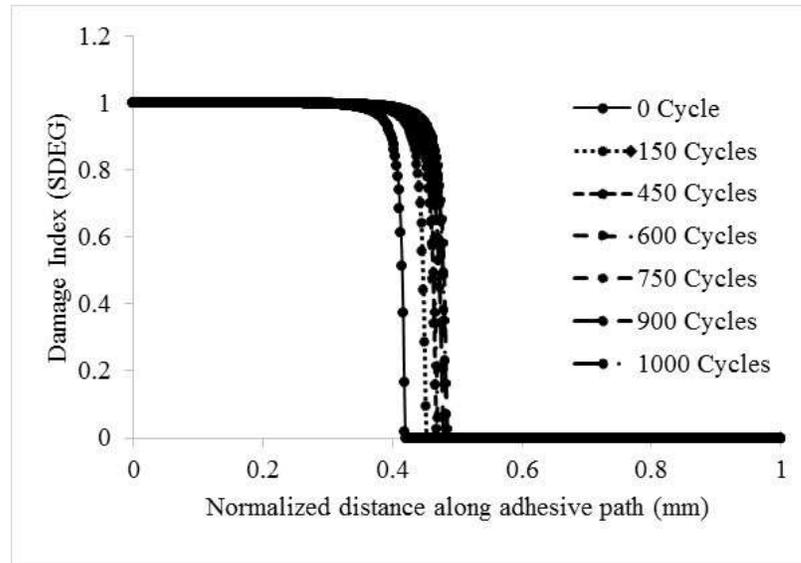
Figure 4-8 Scalar stiffness degradation SDEG curves at the bond line of the ENF specimens before and after having been exposed to various thermal cycles

Figure 4-9 shows essentially the same data, but this time as a function of time (hence the damage histories of the ENF specimens). The illustrated results give an indication of how quickly the stiffness is degraded and stabilized after a certain time. As can be seen, regardless of the number of thermal cycles an ENF specimen was exposed to, the resulting damage gets initiated at a very early stage of mechanical loading (i.e., virtually within the first 0.1 second), attaining its maximum value very quickly as well (within another 0.1 sec.). However, the results indicate that only the specimen that was pre-thermally cycled to 1000 cycles would actually face delamination in comparison with the baseline specimen.
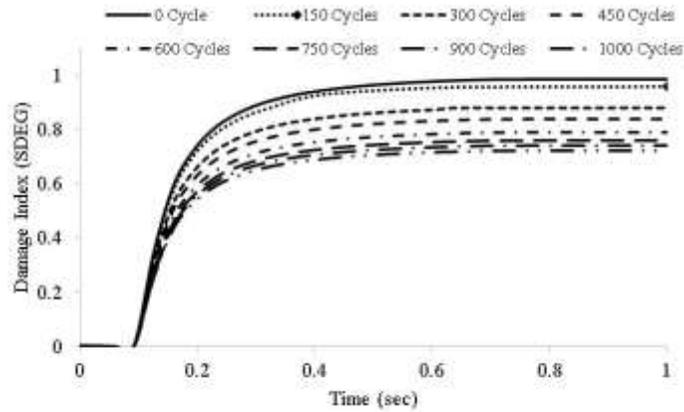
Figure 4-9 Damage history for ENF Specimen

4.5.3 Mixed mode fracture response (SLB specimen)

The load-displacement curves obtained from the experiment and FE simulation are illustrated in Figure 4-10. Under the mixed-mode state, the FE results match the experimental results, up to the state when the actual separation of the adherend occurred. In other words, the FE could not simulate the sudden unzipping that was observed during testing.
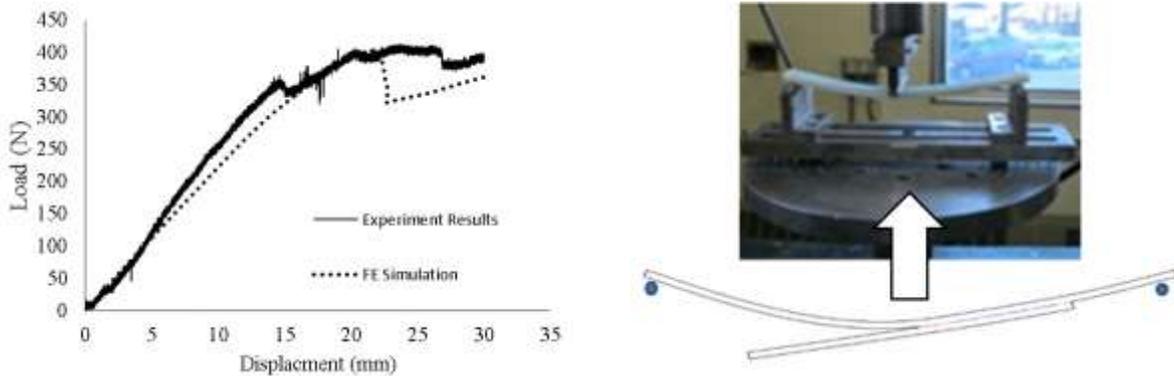
Figure 4-10 Comparison of the FE and experimental load-displacement results and deformed shapes for a typical SLB specimen

It should be noted that the boundary conditions in SLB configuration produce an uneven mixed modity with Mode I fracture dominating. Our FE analysis revealed a stress intensity factors ratio

(K_I/K_{II}) of 1.48 for the specimens used in this test. The contour distribution of the damage indices (SDEG) is shown in Figure 4-11.
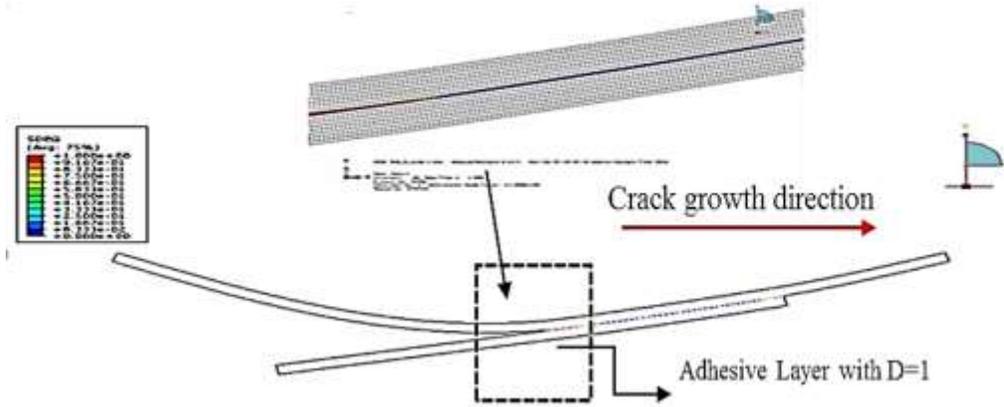
Figure 4-11 Contour variable distribution of damage index (SDEG) for SLB

Moreover, variations in distribution of SDEG for all thermally cycled SLB specimens are shown in Figure 4-12. As can be seen, a notable degradation can be observed as a function of increasing number of thermal cycles. However, the degradation rate is not a linear function of the applied thermal cycles.
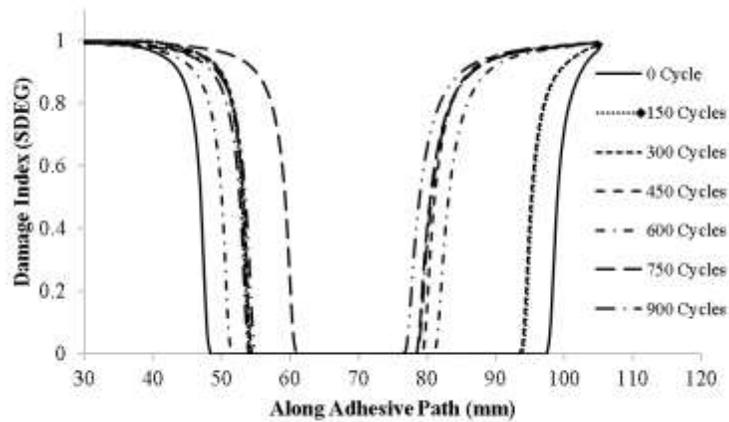
Figure 4-12 Scalar stiffness degradation SDEG curves at the bond line of the SLB specimens before and after having been exposed to various thermal cycles

Figure 4-13 shows variation of the SDEG variable as a function of time. In comparison to the response of ENF specimens, there appears to be an abrupt change in the damage variable as the number of applied cycles exceeds 300 cycles. This is interestingly in line with the somewhat strange degradation response phenomenon observed and discussed in the previous chapter.
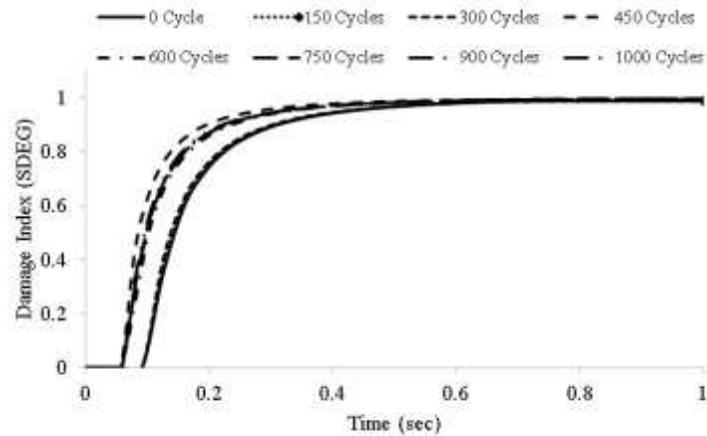
Figure 4-13 Damage history for SLB specimen

4.6 Summary and Concluding Remarks

In this portion of the study, the influence of thermal cycling on the performance of ABJs was examined numerically. Finite element simulation, using the CZM, was demonstrated to be an effective means for simulating the response of the specimens. An experimental investigation was carried out to establish the change in Mode I, II and mixed mode fracture toughness values as a function of applied thermal cycles. The integrity of a relatively straightforward and relatively simple CZM that can be used to simulate the fracture response of ABJs under Mode I, Mode II and mixed-mode (I/II) fracture states was established. The adopted numerical framework was capable of predicting the fracture response of the joints under combined thermal fatigue and monotonic mechanical conditions with good accuracy. Post-processing of the numerical results could exhibit the degradation levels developed within the adhesive as a function of the applied thermal cycles. The following conclusions are drawn based on the described investigations.

i.   It was revealed that only Mode I fracture toughness values degraded as a function of the applied thermal cycles with a relatively linear trend. Therefore, a simple equation was established relating the degradation in Mode I fracture toughness of the epoxy resins as a function of the applied thermal cycles.

ii.   The resulting thermal degradation affected the crack propagation path created by the applied mechanical loading. In other words, the initial crack, which started propagating in a cohesive manner, altered its path in the joints whose adhesive was degraded by the thermal cycles. As the degradation increased, the crack changed its path and, in some cases, traveled into the adjacent plies, since the resin forming the adherends' plies was also degraded as the result of thermal cycling.

iii.   The computational strategy, using the CZ modeling technique, proved to be an effective method for assessing the effect of thermal degradation and subsequent mechanical loading on ABJs. It was demonstrated that by using the simplest form of CZM, one could produce results with an acceptable accuracy. The finite element simulation's results indicate that this modeling strategy could be used to predict the performance of mode complexity configured ABJs subject to various loading conditions with a reasonable degree of confidence.

iv.   The computational strategy, using the CZ modeling technique proved to be an efficient method for assessing the effect of thermal degradation and subsequent mechanical loading on ABJs. Specifically, the use of the simplest form of CZM (i.e., the bilinear CZM), in conjunction with the finite-element method, was found to be adequate for producing a robust and fairly accurate means for simulating the progressive damage process caused by thermal cycling load in such ABJs.

Chapter 5: Minimization of Debonding Stresses in Composite/Metal Adhesively Bonded Joints subject to Combined Cyclic Thermal and Mechanical Loads

5.1 Introduction

Several optimization approaches have been developed to establish the optimum sequence of FRP layup and the layer fiber orientation of a given structural component in order to reduce the weight, yet maintaining the integrity of the component under the prescribed loading. For example, several investigators have used the single or multi-objective approach for the optimization (see for instance, Gürdal et al., 1999; Haftka and Gürdal, 1992; Hancox, 1998; Silberschmidt, 2016; Sonmez, 2017). Within these approach, any function (or target) can be set as the optimization objective(s), which in turn would be minimized or maximized, and the results are used to specify the required lamination fiber orientation and sequence. However, these sophisticated techniques often lead to fiber orientations that are usually impractical from manufacturing viewpoint. Moreover, while the resulting fiber orientations may be practical for fabrication of a single component, they may not be practical in certain cases where a component is to be mass-produced. Therefore, a more practical and intuitive approach is sought, with the emphasis on keeping the resulting fiber-orientation and ply sequencing practical, thus easily manufacturable. It should be emphasized that in this work, the proposed approach used for selecting the optimal FRP adherend layup does not follow the conventional optimization techniques as will be briefly reviewed in section 5.3.1. The optimization terminology used here is in the context of selecting the most optimum laminate that generates the lowest magnitude of peel and shear stresses in ABJs.

5.2 Problem Statement and Objectives

The ABJ of interest is the single lap-strap joint, as shown in Figure 5-1. The joint is made of composite and metallic adherends, representing the commonly used repair technique for rehabilitating various forms of damage in metallic substrates by FRP patching (see Duncan, 2010).
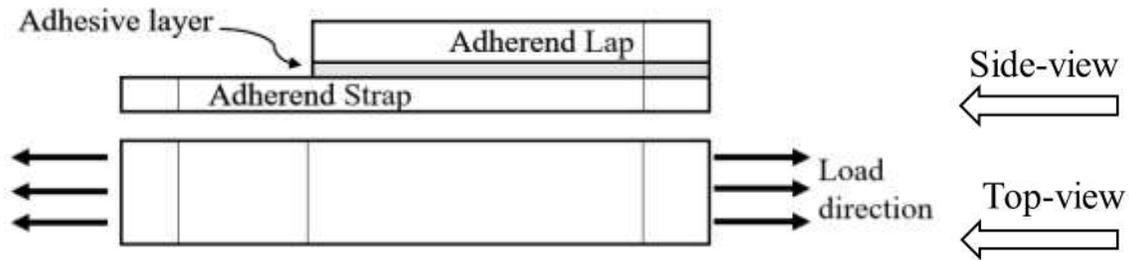
Figure 5-1 A schematic of metal/composite single strap joint.

The objective of this work is to establish the most optimal fiber orientation in order to minimize the effect of thermal fatigue on the ABJ. It should be noted that in order to maintain an unbiased comparison, the ply sequence was not considered as the optimization objective. That is because all FRP adherends had to have the same flexural stiffness, so that a consistent and unbiased comparison could be made. Moreover, the influence of ply sequencing on the transfer of stress to adhesive is negligible for the reasons that will be discussed in detail in the following section. Therefore, FRP adherends with various fiber orientations were designed such that all had similar flexural stiffness. The fiber orientations were selected to produce FRP adherends with varying coefficient of mutual influence (CMI) and Poisson's ratio (PR) (which will be introduced later). This was done so that the difference in the aforementioned parameters (optimization objectives) would vary from a minimum value to a maximum. Subsequently, the ABJs made of these adherends were numerically analyzed, using ABAQUS, a widely used commercially available FEA software to establish stresses. The optimal performing FRP adherend fiber orientation was established based on the values of the peel and shearing stresses developed along adherend/adhesive interface and within the adhesive.

5.3 Optimization using Lamination Parameters

5.3.1 A brief review of various optimization techniques

As briefly stated earlier, several researchers have proposed various optimization strategies for establishing the optimal stacking sequence and lamination thickness of composite structures. Ghiasi et al. (2010, 2009) reviewed these optimization techniques and classified them into two categories: (i) constant stiffness design, and (ii) variable stiffness design. The former category

considers composite laminates with uniform stacking sequence, while the latter technique uses different parameterization and optimization algorithms that produce variable sequencing.

Typical constraints considered in most optimization problems have been the laminate's stiffness, or strength under static, buckling or thermal loadings. For example, Ghugal and Kulkarni (2013) studied the flexural response of symmetric cross-ply laminated plates subjected to uniformly distributed linear and nonlinear thermo-mechanical loads using the trigonometric shear deformation theory. Their results were compared with those obtained by the classical plate theory, first-order shear deformation theory and the higher-order shear deformation theory. Moreover, Raju and Kumar (2011) developed an analytical procedure to investigate the thermal characteristics of laminated composite plates under thermal loading based on a higher-order displacement model with the zig-zag function (ZZF), without enforcing zero transverse shear stresses on the top and bottom faces of the laminated plates. In this regard, Ghomshei and Mahmoud (2010) studied thermal buckling analysis of cross-ply laminated rectangular plates under non-uniform temperature distribution using the differential quadrature approach (DQM). Two steps were included in this method; the first one was solving the problem of in-plane thermo-elasticity to obtain the in-plane force resultants and the second was resolving the buckling problem under the force distribution achieved in the previous step. Fares et al., (2005) presented a multi-objective design and control optimization for achieving the minimum thermal post-buckling dynamic response of laminated composites and maximizing the temperature that would cause their instability. Moreover, Fares et al. (2004a) studied the design and control optimization of laminated composite truncated conical shells to attain the optimal dynamic response. In another study, Fares et al. (2004b) presented a multi-objective optimization problem to determine the optimal layer thickness and optimal closed loop control function for asymmetric cross-ply laminate subjected to thermomechanical loadings. Their optimization procedure aimed at maximizing the critical combination of the applied edge loads and temperature levels and to minimize the laminate dynamic response subject to constraints on the thickness and control energy.

5.4 A simple approach to optimize FRP adherend in ABJs

It is hypothesized that the mismatch in the PR of the two adherends (i.e., FRP and steel) and/or the mismatch of adherends' CMI are the parameters responsible for increasing the peel and shear stresses in ABJs. This hypothesis follows the argument presented by Herakovich (1981) who claimed the variation in mismatch of plies PR and CMI were responsible for maximizing the interlaminar shearing stresses. More details on the mismatch considerations of the CMI ($\delta\eta_{xy}$) and (δv_{xy}) are provided in the next section. It should be noted that the FRP adherend of the single lap-strap joint has a symmetric layup. The stress components that would be critical ABJs are customarily monitored are the peel (S_{zz}) and shear (S_{xz}) stresses under the axial loading applied along the x-direction. Figure. 5-2 illustrates the stress components developed in the adhesive layer of a a typical bonded joint.
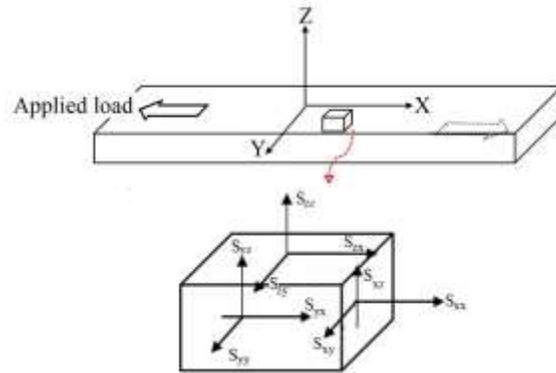
Figure 5-2 Distribution of the stresses in the adhesive of a typical bonded joint subjected to axial loading

The main objective of this part of the study is to examine the integrity and applicability of the aforementioned hypothesis. The successful outcome of this objective would enable one to establish the optimal fiber orientation of the FRP adherend that would produce the least magnitude of peel and shear stresses within ABJs formed with dissimilar adherends that are subjected to a combined cyclic thermal and mechanical loadings.

5.4.1 Mismatch Considerations

CMI also known as the shear coupling coefficient was first identified by Lekhnitskii (1963), as the parameter that results from coupling of the normal and shear stresses. It should be noted that the coefficient can be created due to an applied shear stress or an applied normal stress, each being the ratio of the associated strain to the applied strain for the given stress state, (Lee and Suh 2005). In this work, the CMI ($\eta_{xy(x)}$) is calculated as the ratio of the shear strain γ_{xy} to the axial strain ε_{xx}, with CMI defined as follows:

$$\eta_{xy\,(x)} = \frac{\gamma_{xy}}{\varepsilon_{xx}}$$

5-1

Where γ_{xy} is the in-plane shear strain and ε_{xx} is the normal strain in x direction.

PR is defined as the ratio of the induced lateral strain ε_{yy} due to an axial strain ε_{xx} caused by the application of an axial stress; mathematically it is represented as:

$$\nu_{xy} = -\frac{\varepsilon_{yy}}{\varepsilon_{xx}}$$

5-2

Several different combinations of plies having different fiber orientations were considered. The combinations would have varying PR and CMI, but all would have similar (equivalent) flexural stiffness. Two different reinforcing fibers were selected (i.e., carbon and E-glass). The same room-cured two-part structural epoxy (West System (Bay City, MI)) was used as the matrix. The mechanical properties of the two FRP are reported in Table 5-1. Note that the longitudinal and transverse modulus of elasticity of E-glass-epoxy were evaluated in-house, while the other properties were either adopted from the textbook by Mallick (2007) or calculated based on the mechanics of materials approach.

Table 5-1 Material properties of the FRP adherends

Materials	Modulus of elasticity (GPa)		Poisson's Ratio**		Shear Modulus (GPa)*		Thermal expansion coefficient ** $(10^{-6}/\,°C)$	
	E_1	$E_2 = E_3$	$\upsilon_{12} = \upsilon_{13}$	υ_{23}	$G_{12} = G_{13}$	G_{23}	α_1	$\alpha_2 = \alpha_3$
Glass/epoxy adherends	23.5	5.6	0.25	0.428	3.7	3.28	6.34	23.3
	Ply thickness = 0.4375 mm							
Carbon/epoxy adherends	181**	10.28**	0.28	0.38	12.96	12.96	18	0.223
	Ply thickness = 0.22 mm							
Epoxy adhesive	3.5		0.35		0.4		85	

Directions: 1- along the fiber, 2- orthogonal to the fiber, 3- through-thickness
* Calculated data, ** data adopted from the textbook of Mallick (2007)

As stated earlier, for an unbiased analysis, the laminates with varying PR and CMIs were designed such to have the same flexural stiffness (i.e., same D_{11}), using the following standard equations (Mallick, 2007).

$$A_{ij} = \sum_{k=1}^{n} \int_{Z_k}^{Z_{k+1}} \overline{Q_{ij}^k}\, dZ = \sum_{k=1}^{n} \overline{Q_{ij}^k}\,(Z_k - Z_{k-1}) \qquad \text{5-3}$$

$$B_{ij} = \sum_{k-1}^{n} \int_{Z_k}^{Z_{k+1}} \overline{Q_{ij}^k}\, Z \ dZ = \frac{1}{2}\sum_{k=1}^{n} \overline{Q_{ij}^k}\,(Z_k^2 - Z_{k-1}^2) \qquad \text{5-4}$$

$$D_{ij} = \sum_{k-1}^{n} \int_{Z_k}^{Z_{k+1}} \overline{Q_{ij}^k}\, Z^2 dZ = \frac{1}{3}\sum_{k=1}^{n} \overline{Q_{ij}^k}\,(Z_k^3 - Z_{k-1}^3) \qquad \text{5-5}$$

where A_{ij}, B_{ij} and D_{ij} are the in-plane, axial-bending and bending stiffness matrices; $\overline{Q}$ is the transformed stiffness matrix of each ply; Z_k and Z_{k-1} refers to the distance measured from bottom and top of each ply to the mid-plane, respectively, and k and n refer to the individual ply number and total number of plies in the laminate, respectively, and finally, i and j =1, 2, 6. Note that the thickness of each layer of glass-epoxy and carbon-epoxy was taken as 0.4375 mm and 0.22 mm, respectively. In addition, the lay-ups were kept symmetric. Table 5-2 reports the values of the equivalent D_{11} and A_{11} for the considered FRP layup combinations.

The difference or mismatch of CMI and PR was calculated by considering properties of the adhesive and ply layer adjacent to it, using the following equations, respectively:

$$\left|\delta\eta_{xy(x)}\right| = \left|\eta_{xy,x}(adj\ ply) - \eta_{xy,x}(adh)\right| \qquad \text{5-6}$$

$$\left|\delta v_{xy}\right| = \left|v_{xy}(adj\ ply) - v_{xy}(adh)\right| \qquad \text{5-7}$$

where (*adh*) and (*adj ply*) refer to the adhesive and adjacent ply, respectively. The mismatch in CMI ($\eta_{xy(x)}$) and PR (v_{xy}) properties of the selected laminates are listed in Table 5-3 and Table 5-4, respectively. For the sake of comparison, two mismatch values are reported for each FRP layup. First, the one associated with the mismatch of CMI of the entire FRP adherent with respect to adhesive is reported, and then the mismatch of CMI of the FRP ply that is adjacent to the adhesive, with respect to adhesive is reported.

Table 5-2 The flexural stiffness of the selected layup stacking sequences

Layup designation				A_{11} 10^6 (Pa-m) Equation 5-3	D_{11} (Pa-m^3) Equation 5-5
FRP type	Layup ID	Composite layup orientation	Number of composite plies		
Glass-epoxy	G1	$[0]_8$	8	83.49	85.23
	G2	$[(0/15)_2]_s$	8	80.06	83.04
	G3	$[0/15/0/30]_s$	8	75.85	82.77
	G4	$[(\pm45)_2/45]_s$	10	51.61	82.31
	G5	$[0/\pm15/0]_s$	8	80.06	82.38
	G6	$[(\pm11.5)_2]_s$	8	79.38	81.03
	G7	$[(0/11.5)_2]_s$	8	81.43	83.92
	G8	$[(\pm45)/0/\pm15]_s$	10	79.81	99.54
	G9	$[11.5]_8$	8	79.38	81.03
	G10	$[22]_{10}$	10	86.94	138.7
	G11	$[10]_8$	8	80.36	82.03
	G12	$[(\pm10)_2]_s$	8	80.36	82.03
	G13	$[(\pm15)_2]_s$	8	76.63	78.23
	G14	$[15]_8$	8	76.63	78.23
Carbon-epoxy	C1	$[0]_8$	8	319.98	82.59
	C2	$[(\pm35)_2/35]_s$	10	210.54	84.91
	C3	$[10]_{10}$	10	379.9	153.25
		$[(0/15)2]s$	8	303.48	79.77
	C5	$[(\pm11.5)2]s$	8	298.9	77.17
	C6	$[11.5]_8$	8	298.95	77.17
	C7	$[(\pm35)_2/0]_s$	8	248.43	85.52
	C8	$[22]_{10}$	10	311.34	125.57
	C9	$[(35)_4/0]_s$	10	248.43	85.52
	C10	$[15]_8$	8	284.97	73.56

Table 5-3 Values of mismatch in CMI for the selected FRP layup stacking sequences

Adherend	Layup ID	$\eta_{xy(x)}$ of FRP Equation 5-1	$\left\|\delta\eta_{xy(x)}\right\|$ (FRP/adhesive)	Ply angle of adjacent ply to adhesive (degree)	$\eta_{xy(x)}$ of adjacent ply to adhesive	$\left\|\delta\eta_{xy(x)}\right\|$ (adjacent ply/adhesive) Equation 5-6
Glass-epoxy	G1	0.00	0.00	0	0.00	0.00
	G2	-0.4046	0.4046	0	0.00	0.00
	G3	-0.4374	0.4374	0	0.00	0.00
	G4	-0.0863	0.0863	45	-0.4824	0.4824
	G5	0.00	0.00	0	0.00	0.00
	G6	0.00	0.00	11.5	-0.5342	0.5342
	G7	-0.3387	0.3387	0	0.00	0.00
	G8	0.00	0.00	45	-0.4824	0.4824
	G9	-0.6441	0.6441	11.5	-0.5342	0.5342
	G10	-0.8338	0.8338	22	-0.8354	0.8354
	G11	-0.5844	0.5844	10	-0.4826	0.4826
	G12	0.00	0.00	10	-0.4826	0.4826
	G13	0.00	0.00	15	-0.6273	0.6273
	G14	0.00	0.00	15	-0.6273	0.6273
Carbon-epoxy	C1	0.00	0.00	0	0.00	0.00
	C2	-0.1302	0.1302	35	-0.9864	0.9864
	C3	-1.4860	1.4860	10	-1.1648	1.1648
	C4	-0.9861	0.9861	0	0.00	0.00
	C5	0.00	0.00	11.5	-1.2459	1.2459
	C6	-1.5800	1.5800	11.5	-1.2459	1.2459
	C7	0.00	0.00	35	-0.9864	0.9864
	C8	-1.6529	1.6529	22	-1.3173	1.3173
	C9	-1.0980	1.0980	35	-0.9864	0.9864
	C10	-1.6927	1.6927	15	-1.3487	1.3487

Table 5-4 Values of mismatch in Poisson's ratio for the selected FRP layup stacking sequences

Adherend type	Layup ID	v_{xy} of FRP Equation 5-2	$\|\delta v_{xy}\|$ (FRP/adhesive)	Ply angle of adjacent ply to adhesive (degree)	v_{xy} of adjacent ply to adhesive	$\|\delta v_{xy}\|$ (adjacent ply/adhesive) Equation 5-7
Glass-epoxy	G1	0.2500	0.1000	0	0.2966	0.0534
	G2	0.2693	0.0807	0	0.2966	0.0534
	G3	0.2770	0.0730	0	0.2966	0.0534
	G4	0.3660	0.0160	45	0.2254	0.1246
	G5	0.3029	0.0471	0	0.2966	0.0534
	G6	0.3159	0.0341	11.5	0.2928	0.0572
	G7	0.2628	0.0872	0	0.2966	0.0534
	G8	0.3495	0.0005	45	0.2254	0.1246
	G9	0.2386	0.1114	11.5	0.2928	0.0572
	G10	0.2153	0.1347	22	0.2810	0.0690
	G11	0.2413	0.1087	10	0.2937	0.0563
	G12	0.3008	0.0492	10	0.2937	0.0563
	G13	0.3515	0.0015	15	0.2898	0.0602
	G14	0.232	0.1182	15	0.2898	0.0602
Carbon-epoxy	C1	0.2800	0.0700	0	0.3317	0.0183
	C2	0.9283	0.5783	35	0.1873	0.1627
	C3	0.0948	0.2552	10	0.2989	0.0511
	C4	0.3122	0.0378	0	0.3317	0.0183
	C5	0.6682	0.3182	11.5	0.2908	0.0592
	C6	0.0558	0.2942	11.5	0.2908	0.0592
	C7	0.8405	0.4905	35	0.1873	0.1627
	C8	-0.1285	0.4785	22	0.2372	0.1128
	C9	0.0238	0.3262	35	0.1873	0.1627
	C10	-0.0252	0.3752	15	0.2718	0.0782

It should be noted that because $\eta_{xy,x}(adh)$ of the adhesive layer is equal to zero, therefore the mismatch of CMI, $|\delta\eta_{xy(x)}|$ will be equal to $|\eta_{xy,x}(adj\ ply)|$. Moreover, the variations in mismatches in CMI and PR of the carbon-epoxy and glass-epoxy adherends as a function of fiber orientations of the ply adjacent to adhesive layer are illustrated graphically in Figure 5-3.

(a)   (b)
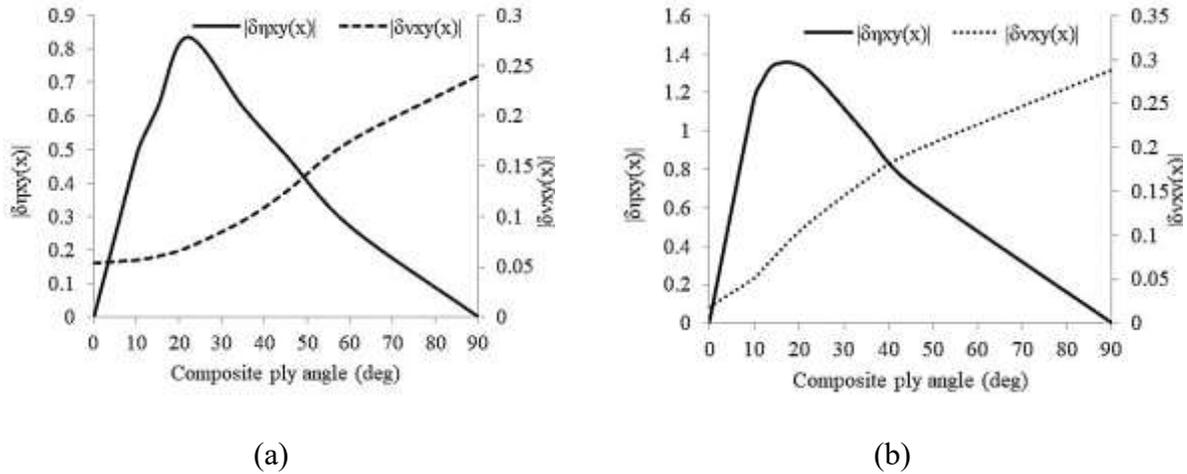
Figure 5-3 Variation in mismatch of the CMI and PR of adhesive and its adjacent ply (a) glass-epoxy adherend and (b) carbon-epoxy adherend

The curves in Figure 5-3 shows the mismatch in CMIs, $|\delta\eta_{xy(x)}|$, attain higher values than the mismatch in maximum differences in PRs, $|\delta v_{xy}|$. Moreover, no CMI mismatch exists for the cases when the adhesive adjacent layer's fiber-orientation is either $0°$ or $90°$ (angles with respect to the longitudinal direction of the joints), since $\delta\eta_{xy(x)}$ of the adhesive attains a zero value, therefore $|\delta\eta_{xy(x)}|$ will be equal to $|\eta_{xy(x)}|$. In addition, the mismatch values in CMIs are greater when the adherend is carbon-epoxy composite compared to glass-epoxy. For the glass-epoxy adherends, the largest mismatch is observed to be $|\delta\eta xy(x)|=0.835$ when the fiber orientation of the adjacent ply to the adhesive is $\theta=22°$, and the next largest value being $|\delta\eta xy(x)|=0.627$ when the ply takes $\theta=15°$ orientation. In comparison, for the carbon-epoxy adherends, the two largest values of mismatch of $|\delta\eta xy(x)|$ are 1.348 and 1.317, when the fiber orientation of their adjacent ply to adhesive takes angles of $\theta=15°$ and $22°$, respectively. The difference in PR mismatches is not as noticeable when considering the adherends. The largest mismatch value among the glass-epoxy

adherends is observed to be $|\delta v_{xy}|=0.124$ when the adjacent ply to adhesive takes fiber orientation of $\theta=45^{\circ}$; the value becomes 0.163 for the carbon-epoxy adherends at the angle of $\theta=35^{\circ}$. It should be noted that for the combinations considered in this study, the maximum values of PR mismatch, as shown in Figure 5-3 are 0.124 and 0.163 when the adjacent ply to adhesive take fiber orientations of $\theta=45^{\circ}$ and $\theta=35^{\circ}$ for the glass-epoxy and carbon-epoxy adherends, respectively.

In summary, the larger mismatch in CMI occurs in the glass-epoxy when the fiber orientation of the adjacent ply to adhesive hovers between 10-45°, and between 10-35° for the carbon epoxy. These values corroborate with the values reported by Herakovich (Herakovich, 1981), when he considered the evolution of interlaminar shear values in various composite layups. Therefore, the admissibility of the hypothesis, with respect to minimizing the stresses in the lap strap ABJs that were subjected to various numbers of thermal cycles and subsequent mechanical loading, will be considered and discussed in detail in the following sections.

5.5 Experimental Investigation

This section reports details of the experimental investigation that was designed and undertaken to study the effect of thermal fatigue and mechanical loading on a lap-strap joint. Appropriate size specimens were fabricated and tested in-house.

5.5.1 Specimen preparation

The composite adherends of the lap-strap specimens were fabricated using the hand layup technique. The composite plates were formed with eight layers of unidirectional fiberglass fabric and the West System (Bay City, MI) room-cured two-part epoxy resin system (i.e., 105 resin and 206 hardener). The plates were then mated with steel plate using the same resin used in fabricating the adherends, with controlled thickness of 0.2 mm. Two groups of lap-strap joints were fabricated. One group had intact joint (joints with no cracks), and the other group had a 25 mm long intentional crack within the beginning portion of the overlap region (see Figure 5-4(a)), running across the full-width each speciemn. The crack was generated using a 25 μm thick Teflon film with a width of 25 mm. The assembled plates were left to cure at room temperature, under 20 kg of distributed

weight, for at least four days. The assembled plates were then cut to appropriate size and tabbed, ready for testing, as illustrated in Figure 5-4 (b).

It should be mentioned that several FE simulations of lap-strap joints with various lengths (i.e., various lengths of steel and FRP adherends) were conducted to establish the dimension of the joint, as shown in Figure 5-4(a).
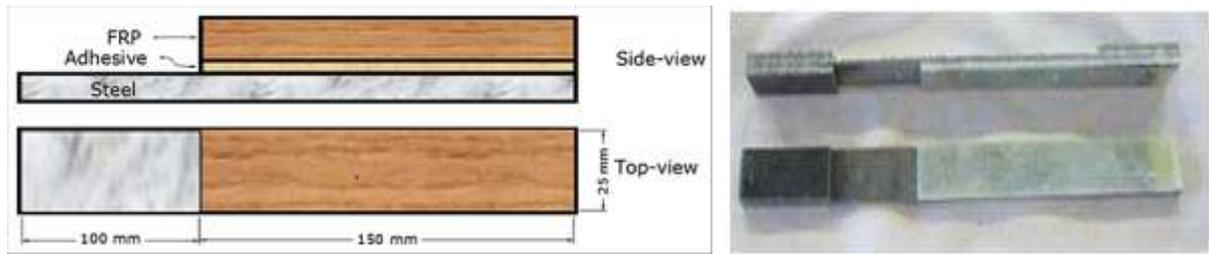
(a)   (b)
Figure 5-4 Lap-strap joint; (a) dimensions (drawings not-to-scale) and (b) actual specimens

5.5.2 Cyclic thermal fatigue test procedure

The specimens were first subjected to a certain number of thermal cycles, as explained in Chapter 3. In total, eight groups of specimens were tested, with each group have been subjected to specific thermal cycles, as reported in Table 3-1. The specimens were subsequently subjected to a tensile loading. Note that group No.1 includes the "virgin" or the baseline specimens that were not subjected to thermal cycling and were only loaded monotonically.

5.5.3 Mechanical test procedure

The tensile loading was applied using an electronically controlled Instron servo-hydraulic test machine (model 8500+), with a 100 kN load cell. The applied load was recorded by the machine, while the strain in a certain portion of each specimen was monitored using a laser extensometer, whose data was acquired through a data-acquisition system (DAQ) and stored in a personal

computer. The tests were conducted under the displacement-control regime, at a displacement rate of 2 mm/min and sampling rate of 0.05 kHz. Figure 5-5 show the test setup.
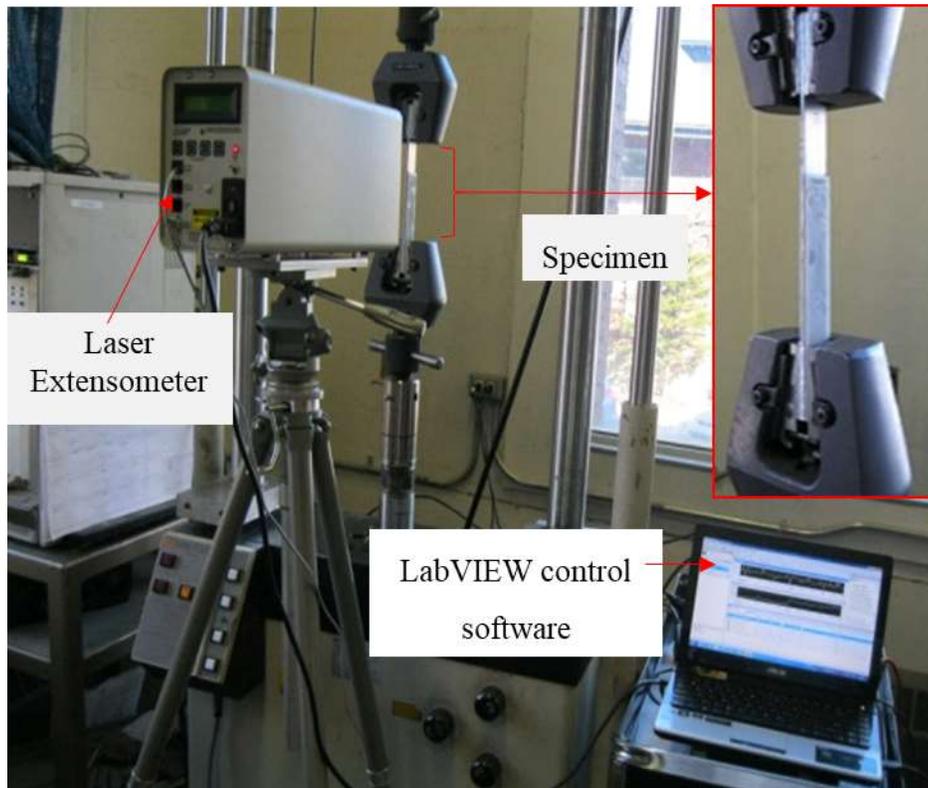
Figure 5-5 Overview of the experimental setup

5.5.4 Experimental results

Figure 5-6 shows typical load-deflection curves of the lap-strap joint specimen. As illustrated, the load varies relatively linearly as a function of the axial displacement until the first crack occurs, after which the load carrying capacity is reduced significantly, leading to the final failure (debonding of the adherends). Of course, the steel adherend endured additional applied load; however, that portion of the loading is not included in the graph. This is because as the loading continued, it became evident that only steel carried the additional load.
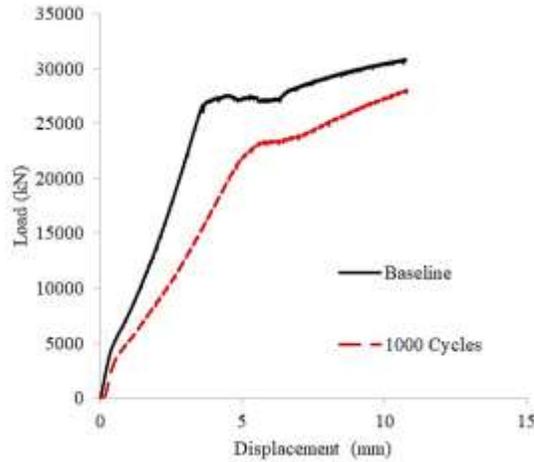
Figure 5-6 Typical load-displacement curves of the tested lap-strap joint specimens

5.5.5 Fracture toughness evaluation method

A closed-form solution was used to establish the fracture toughness of each group of specimens. The solution was developed based on the beam theory by Brussat et al. (1977). According to the solution, the fracture toughness G_T of the lap-strap joint specimens with dissimilar adherends can be calculated using the following equation:

$$G_T = \frac{P^2}{2b^2}\left[\frac{1}{E_s t_s} - \frac{1}{E_s t_s + E_l t_l}\right] \qquad \text{5-8}$$

where P is the applied load, b is the specimen width, E_s is the elastic modulus of the strap part of the joint (in this case, the steel adherend), t_s is the strap adherend's thickness, E_l is the elastic modulus of the intact portion of the joint (i.e., of the combined steel/FRP adherends), with t_l being the thickness of that section. The comparison of calculated G_T of the tested groups of specimens is illustrated in Figure 5-7.

92
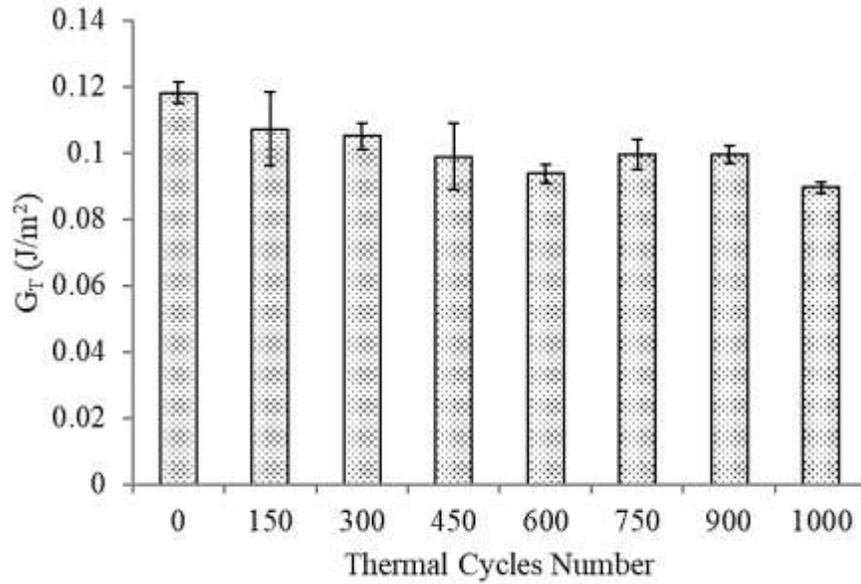
Figure 5-7 Comparison of the fracture toughness (G_T) values of the tested groups of lap-strap joint specimens

5.6 Computational Investigation

5.6.1 Simulation framework

Lap-strap joints were modeled using ABAQUS/Standard. The three parts of the joint (i.e., steel, adhesive and FRP) were modeled using C3D20R 20-node quadratic brick element with reduced integration and hourglass control. To increase the accuracy of the results within the adhesive layer (the subject of our interest), it was modeled by seven layers of solid elements through its thickness. The analysis included nonlinear geometry, as well as incorporation of the piecewise nonlinear elastoplastic material model that captured the response of the steel and adhesive materials. The FRP plies were modeled as "solid composite" with three integration points for each ply. The material properties of the constituents are reported in Table 5-1. The stress-strain data for the steel and adhesive were obtained experimentally in-house, as illustrated in Figure 5-8.

93

(a)   (b)
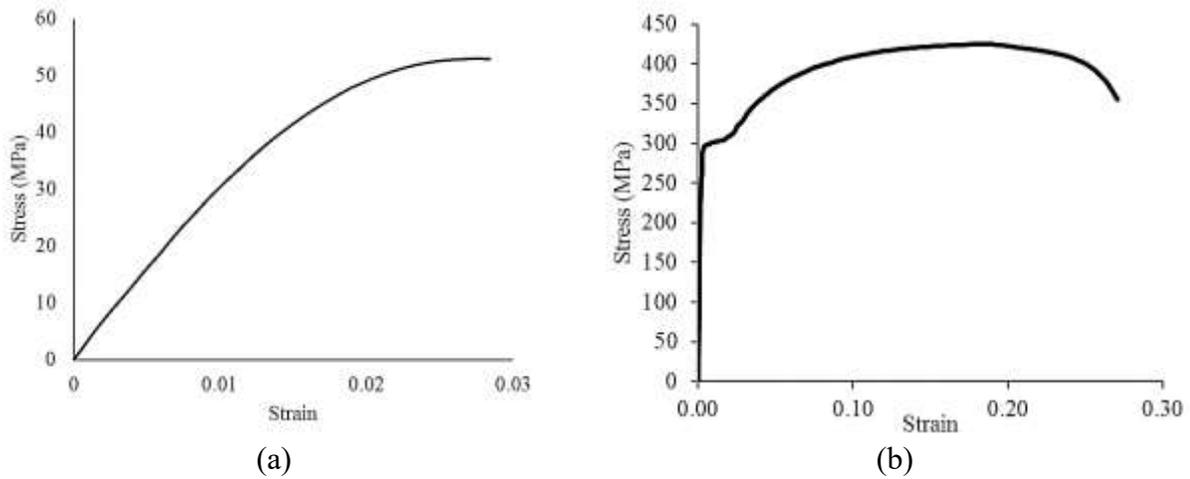
Figure 5-8 Stress-strain curves of (a) adhesive and (b) steel

All degrees of freedom of the nodes falling within the grip region on one end of the specimen (the right-end of the specimen shown in Figure 5-9) were considered to be fully restrained. On the left-end, all degrees of freedom of the nodes within the grip region were restrained, with the exception of the axial displacement degree-of-freedom, which was allowed to displace. Both the uncracked and cracked specimens were modeled.
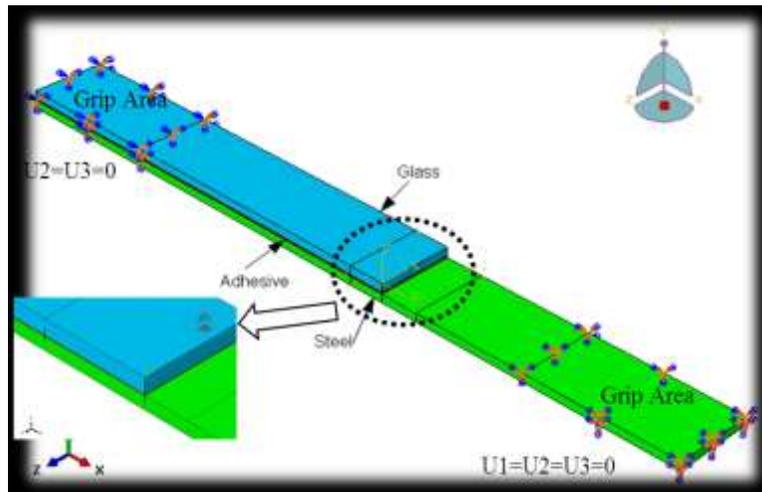
Figure 5-9 The boundary conditions for lap-strap joint model

5.6.2 Mesh convergence study

It is important to use a sufficiently refined mesh to ensure that the results from the simulation are fairly accurate, yet the analysis time is moderate. Four different mesh densities were used to model the specimen with the unidirectional ($[0]_8$) glass-epoxy adherend. The number of elements for meshes one to four were 5712, 6608, 13496 and 20384, respectively. The densities were locally refined (on the regions where the stress concentrations would be maximum (see the zoomed region shown in Figure 5-10). Moreover, a finer mesh was used to model the regions close to the free edges. The influence of mesh densities was examined by monitoring the resulting variations in the stresses through a path running axially at the mid-thickness of the adhesive. Figure 5-11 shows the comparison of variations in the peel (σ_{zz}) and shear (σ_{xz}) stresses along the beginning 15 mm portion of the path explained above and illustrated in Figure 5-10. As seen, the stress variations become relatively constant after 7 mm into the path. Since variation in the stresses produced by meshes 3 and 4 were very similar, hence, mesh 3 was selected as the effective mesh for conducting the remining analyses.
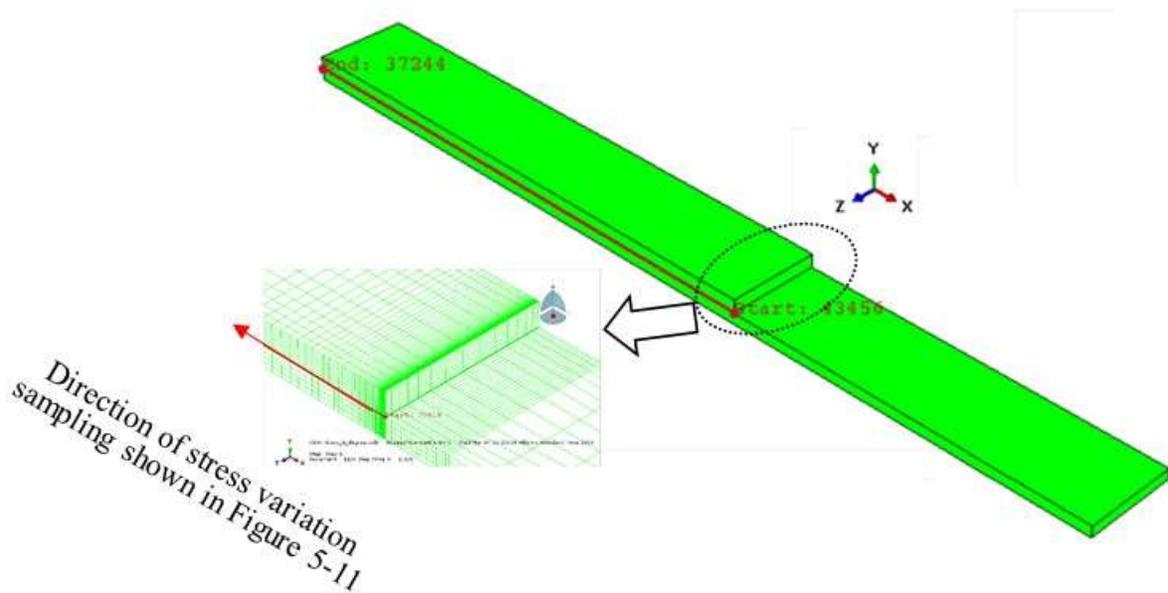
Figure 5-10 The path along which the variation of stresses was monitored

(a)   (b)
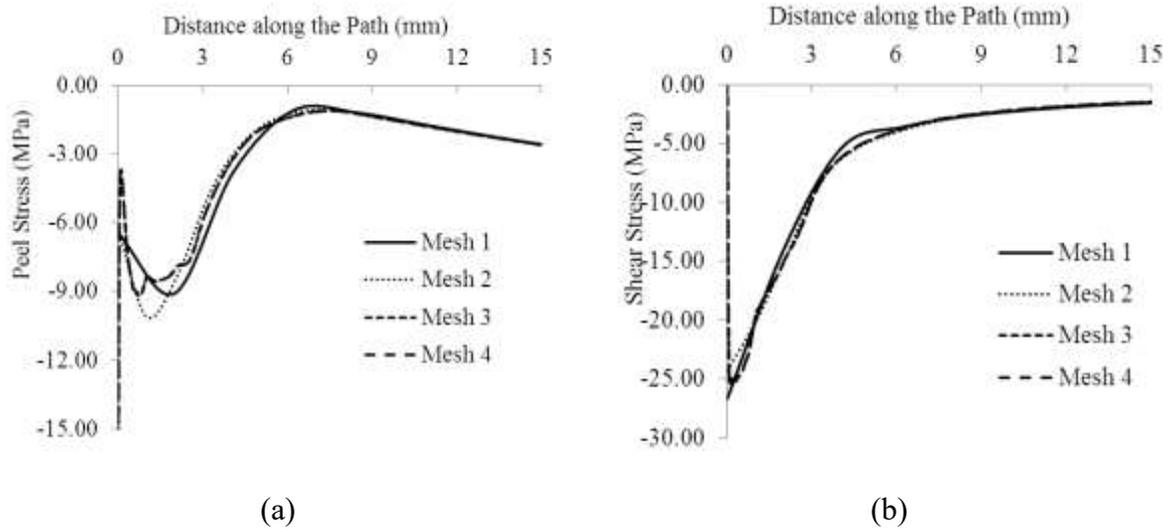
Figure 5-11 Variation in the (a) peel and (b) shear stresses within the first 15 mm portion along the specified path obtained by the models having different mesh densities

5.6.3 Results of the parametric studies

5.6.3.1 Discussion of the results of the intact lap-strap joints

The main purpose of the parametric study was to investigate the influence of FRP adherend layup fiber orientation on the peel and shear stresses developed within the adhesive layer and at the adherends/adhesive interfaces. The aim was (i) to determine whether the mismatches in the CMI and PRs would affect the resulting stress magnitudes, and (ii) if so, what remedy one could apply to reduce the stresses. The results discussed below are obtained when the joint was subjected to a total strain of 0.67%.

Figure 5-12 illustrates the variation in peel and shear stresses along the beginning portion of a path running at three elevations within the adhesive (a) at the top plane of the adhesive (i.e., at the FRP/adhered interface), (b) at the mid-plane within the adhesive and (c) at the bottom plane of adhesive (i.e., at the adhesive/steel interface) for the lap-strap joints with various lay ups of carbon-epoxy adherends. Similar variations are shown for the ABJs having glass-epoxy in Figure 5-13. Note that the illustrated variations in stresses were taken along a path running at the mid-width of the adhesive layer. The variation of the stresses taken along the edge follows a very similar trend.
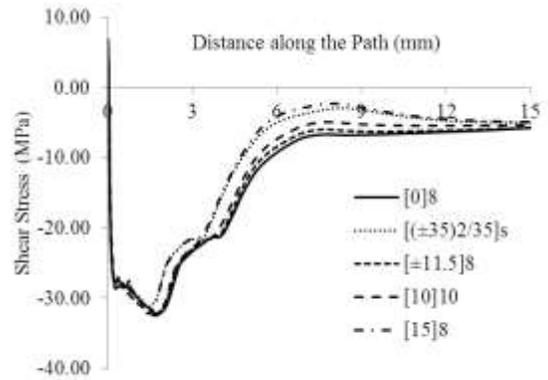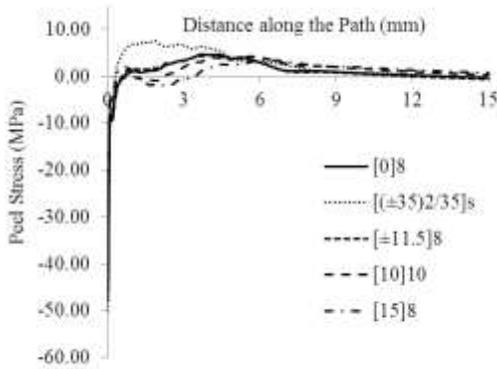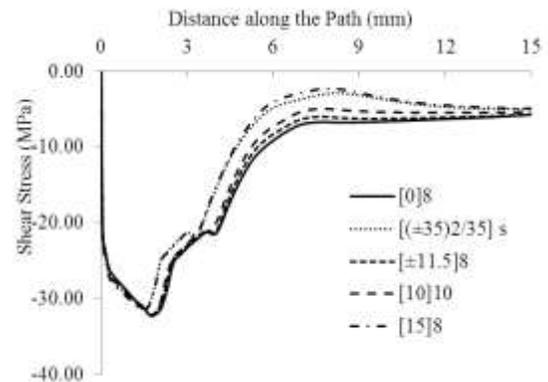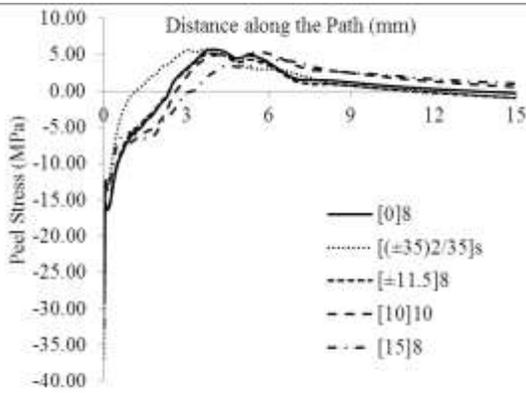
96

The path running at the interface of FRP and adhesive

The path running at the mid-thickness of the adhesive
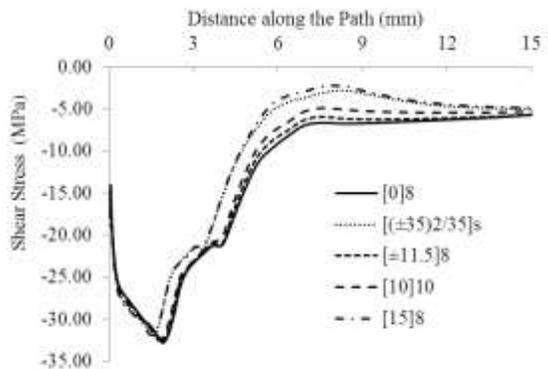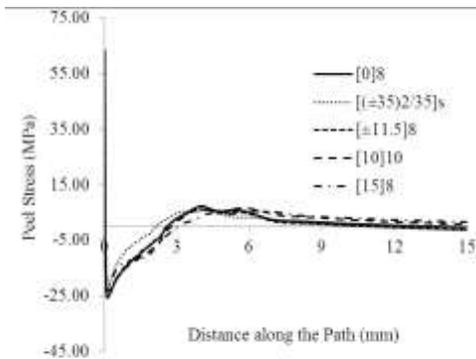
The path running at the interface of steel and adhesive

Figure 5-12 Variation of the peel and shear stresses along the 15 mm distance within the mid-thickness and the two interfaces of the carbon-epoxy/steel lap-strap joint
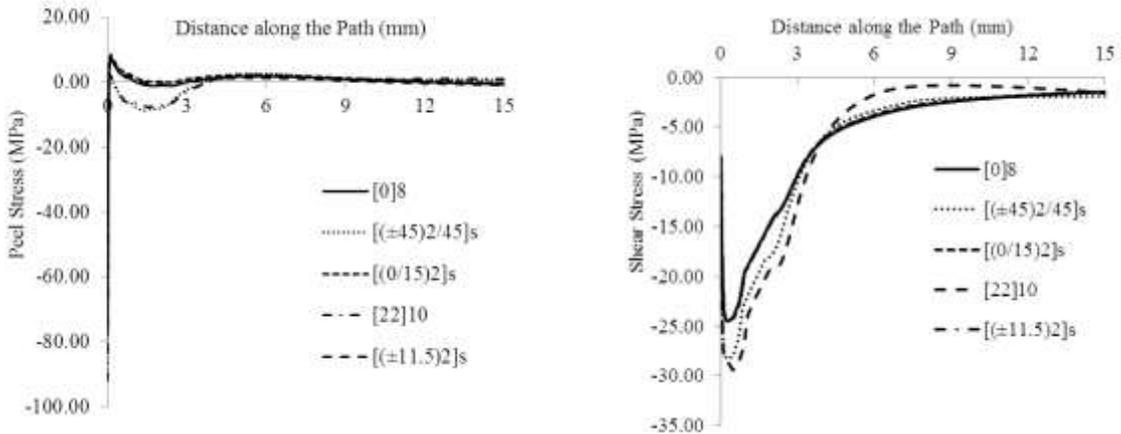
The path running at the interface of FRP and adhesive
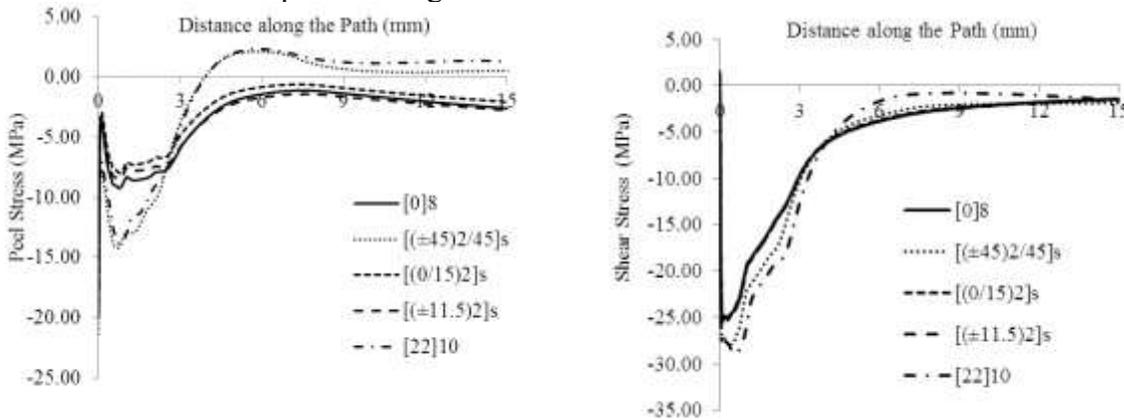
The path running at the mid-thickness of the adhesive
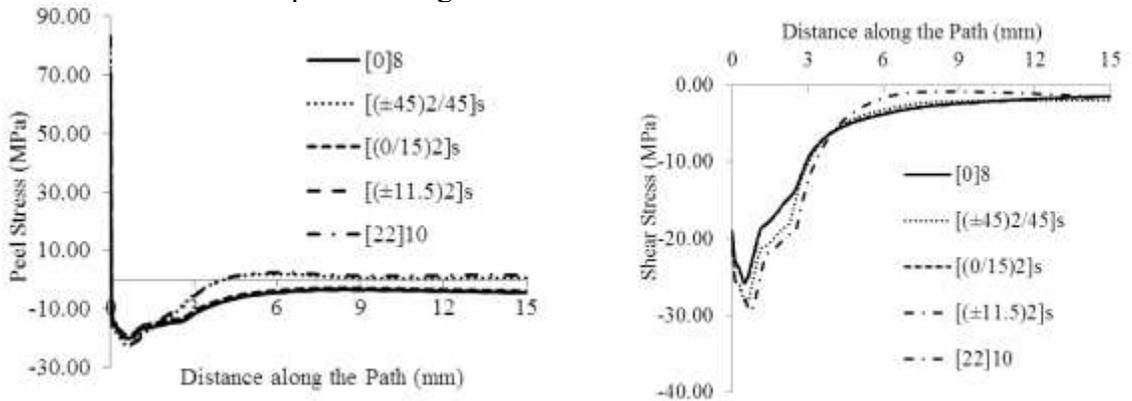
The path running at the interface of steel and adhesive

Figure 5-13 Variation of the peel and shear stresses along the 15 mm distance within the mid-thickness and the two interfaces of the glass-epoxy/steel lap-strap joint

As can be seen, at this relatively moderate level of applied loading, the peel stress is compressive in almost all regions within the adhesive and interfaces; however, it becomes tensile with an alarming magnitude, right at the start of the joint (at the stress concentration region), which exceed the tensile strength of the adhesive. Moreover, the influence of adjacent ply fiber orientation becomes significant for some of the selected fiber orientations.

In joints with carbon-epoxy adherends, those with the layups of $[(\pm35)_2/35]_s$ and $[22]_{10}$ exhibited comparable values. When comparing the stress distribution of the joint with unidirectional layup ($[0]_8$) with the aforementioned layups, one can see that the unidirectional adherend exhibited lower overall peel stress, but greater shear stress. In addition, the influence of mismatches of CMI and PR of the tried stacking sequences are quite apparent from the results presented in the figures. Interestingly, when comparing the shear stress values, while the unidirectional adherend generates the greatest stresses in joints with carbon-epoxy adherends, that lay up would develop the lowest shear stress in joints with glass-epoxy adherend. However, when considering the peel stress, the carbon-epoxy and glass-epoxy with $[(\pm35)_2/35]_s$ and $[(\pm45)_2/45]_s$ layup respectively, generate very large tensile peel stresses.

Moreover, larger stresses are observed to have been developed on the FRP/adhesive interface in comparison to steel/adhesive interface, regardless of the stacking sequence.

In addition, Figure 5-14 and Figure 5-15 show the distributions of peel and shear stresses through thickness of the adhesive layer for the joints with carbon-epoxy and glass-epoxy adherends, respectively, at the free edge (note that steel adherend is below the composite adherend in these figures).
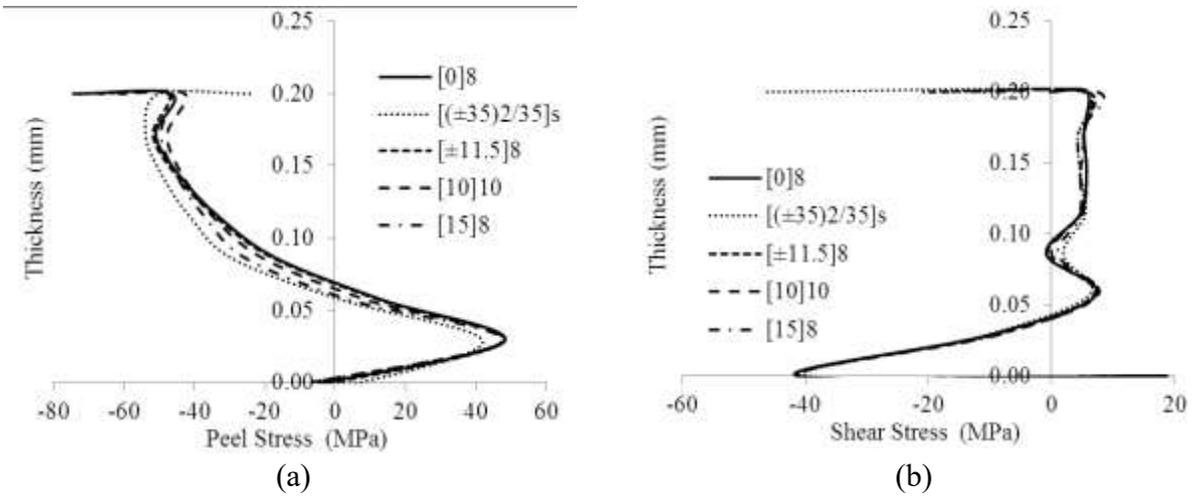
Figure 5-14 Distributions of the (a) peel and (b) shear stresses through the thickness of the adhesive layer in joints with carbon-epoxy adherends
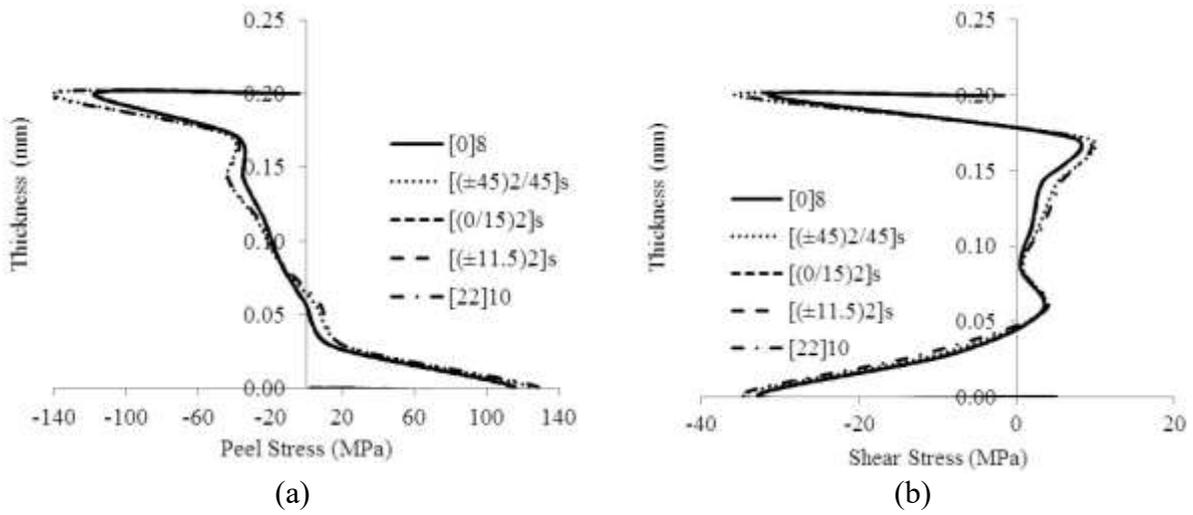
Figure 5-15 Distributions of the (a) peel and (b) shear stresses through the thickness of the adhesive layer in joints with glass-epoxy adherends

Figure 5-16 illustrates the distribution of the von Mises stress at a plane running in the mid-plane of the adhesive, as well at the interfaces in the joint with glass epoxy.
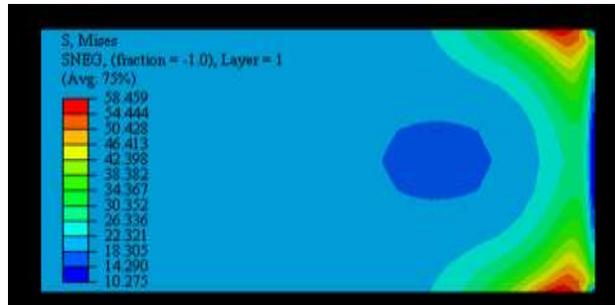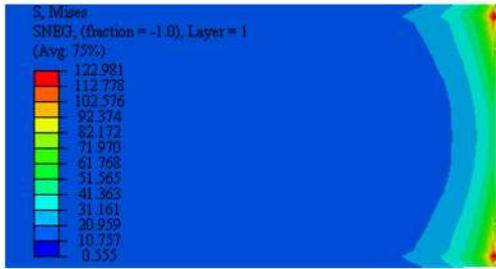
Plane at the interface of GFRP and adhesive

Plane at the mid-plane of adhesive
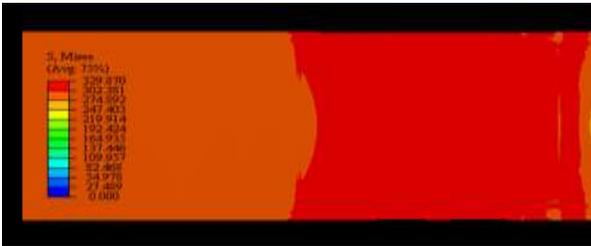
Plane at the interface of steel and adhesive

Joint with $[0]_8$ adherend   Joint with $[22]_{10}$ adherend

Figure 5-16 Contour distribution of von Mises stress within the adhesive at three different planes of joints made with glass-epoxy adherend

Note that the effect of the thermal cycling was not accounted for in the specimens whose results were presented above. In other words, the stress contours were as a result of mechanical loading, only, basically comparing the performances of two "virgin" or baseline lap-strap joint specimens having FRP adherends with different layups. In contrast, the results for the specimens that underwent thermal cyclic loading prior to being subjected to the mechanical (tensile) loading are shown in the following figure. Note that details of how the actual loadings were applied within ABAQUS' environment were reported in Chapter 4. Figure 5-17 and Figure 5-18 show the stress

distributions along a path running at the mid through-thickness plane of the adhesive, along the axial direction, as well as along an axial path running at the adhesive/carbon-epoxy and adhesive/glass-epoxy interfaces, respectively.

It is believed that mismatch in the thermal expansion coefficients, CMI and PR of the adhesive and adherends, all contribute in formation of significant levels of residual stresses within the interfaces. As seen, the variations in the peel and shear stresses caused by the thermal loads exhibit similar general trends as observed in the case of the baseline specimens. Moreover, comparing the results of the joints with carbon-epoxy and glass-epoxy adherends, one can see that the stresses caused by the thermal cycles were comparatively less in the specimens with carbon-epoxy adherends as opposed to those with glass-epoxy adherends.
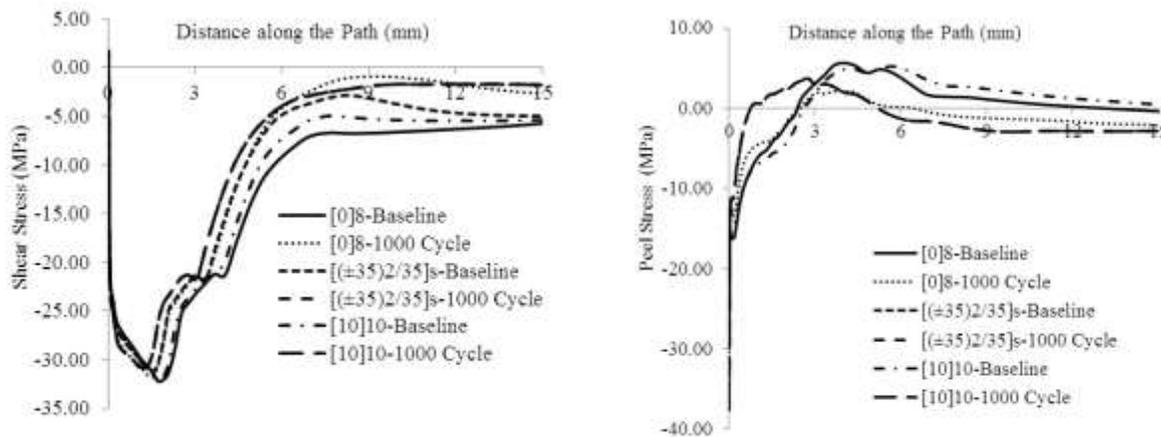
The path running at the mid-thickness of the adhesive

Figure 5-17 Comparison of the variation of the peel and shear stresses of the carbon-epoxy/steel lap-strap joints for both baseline specimens and those that were first subjected to cyclic thermal load and subsequently to mechanical load
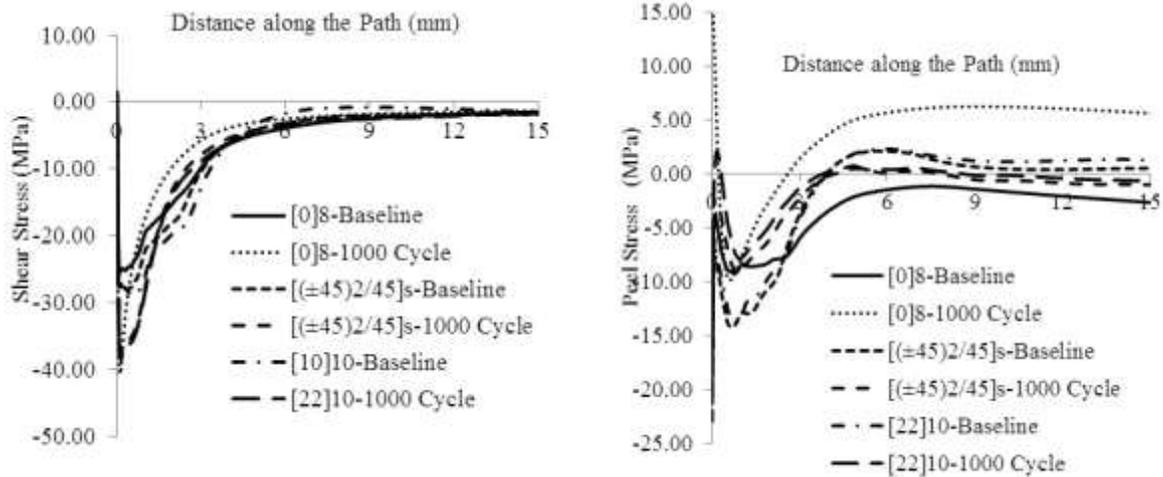
The path running at the mid-thickness of the adhesive

Figure 5-18 Comparison of the variation of the peel and shear stresses of the glass-epoxy/steel lap-strap joints for both baseline specimens and those that were first subjected to cyclic thermal load and subsequently to mechanical load

An interesting observation is made when a uniaxial (0°) ply was added at the FRP/adhesive interface for the FRP layups considered earlier. In such FRP adherends, the value of CMI becomes nullified; as a result, the shear stress distribution within the adhesive of the joints made with such adherends becomes identical. This phenomenon is shown in Figure 5-19. The figure illustrates the variation of the shear stresses along the 15 mm path running through the mid-thickness of the adhesive of the glass-epoxy/steel lap-strap joints with FRP. As can be seen, all curves lay on top of one another. This indicates that CMI has a direct and significant influence on formation of shear stresses within the adhesive in such asymmetric FRP/metal joints.
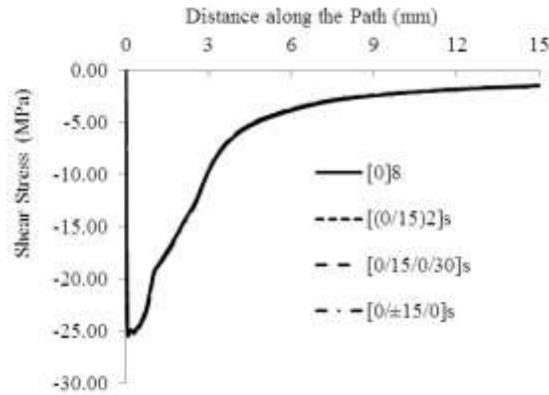
Figure 5-19 Variation of the shear stresses along a path running within the mid-thickness of the adhesive of glass-epoxy/steel lap-strap joints with various FRP layups

5.6.3.2 Discussion of results for lap-strap joints hosting a crack

A CZ modeling approach was also used to account for the presence of the crack that was intentionally created within the specimens, using a 3D-model consisted of three parts (steel, adhesive, and FRP). The adhesive layer was modeled by the cohesive element. To conduct a fairly accurate, yet CPU efficient analysis, a bilinear traction-separation model was used to represent the adhesive's debonding (or decohesion) response. Figure 5-20 shows the variation in the scalar stiffness degradation (SDEG), hereafter referred to as "damage index", for the baseline specimen, along an axial path running within the adhesive for the strap-lap joint with two different ply-sequences of glass-epoxy adherend. The difference in CMI mismatches for the unidirectional adherend is zero, while it is 0.5786 for the [(±45)$_2$/45]$_s$ adherend. The curves clearly show the significance of CMI mismatch in increasing the shear stress within the adhesive.

In addition, the pictorial distributions of the damage index at the mid-plane of adhesive in four joint configurations (two with glass-epoxy adherends with different layups and the other two with carbon-epoxy adherends) are illustrated in Figure 5-21. It can be clearly seen that larger damage indices are developed in joints with glass-epoxy adherents, and that the damage increases in joints whose adherends have greater CMI mismatches.

104
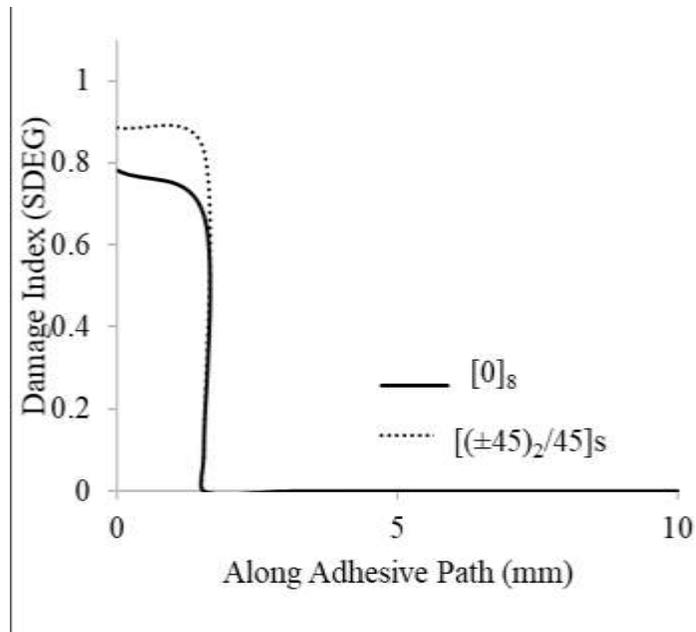
Figure 5-20 Variation in the ABAQUS damage index (SDEG) along mid-plane of the adhesive for joints with glass-epoxy adherends with two different ply-sequences
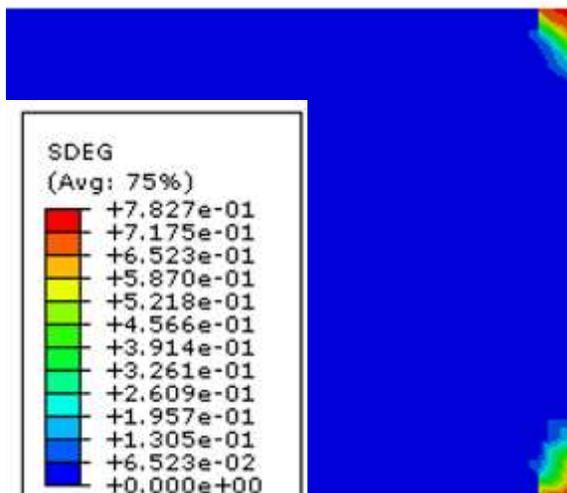
[0]$_8$ glass-epoxy adherend
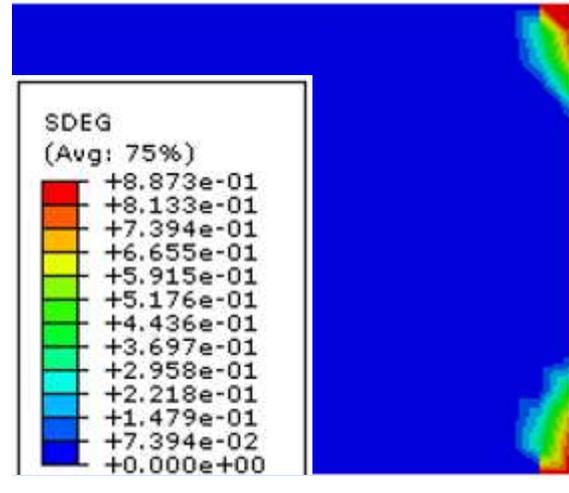
[($\pm$45)$_2$/45]$_s$ glass-epoxy adherend
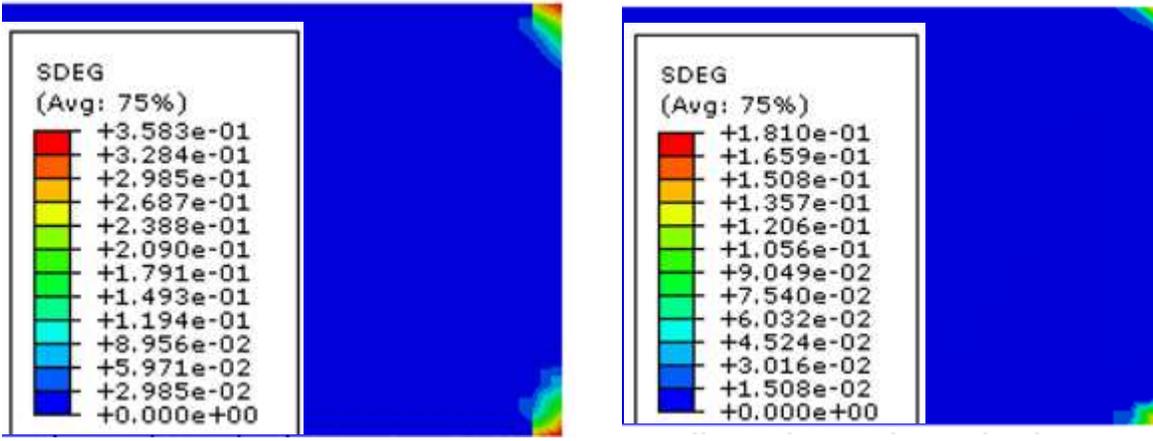
[0]$_8$ carbon-epoxy adherend   [($\pm$35)$_2$/35]$_s$ carbon-epoxy adherend

Figure 5-21 Distribution of SDEG (damage indices) within the adhesive layer of the joint with glass-epoxy and carbon-epoxy adherends having different layups

5.6.4 Effect of thermal loads

As shown in Figure 5-12 and Figure 5-13, degradation in stresses are generated due to the mismatch of the thermal expansion coefficients of the materials forming the joints. Among the carbon-epoxy layups, the unidirectional layup ([0]$_8$) developed the least amount of stress under the thermal cycles. Also, the unidirectional layup generated the least amount of stress under thermal cycles in joints with glass-epoxy adherend. It should be noted that since the thermal expansion coefficient of carbon epoxy is relatively quite small, therefore, the stress due to thermal loads would also be small.

5.7 Summary and Concluding Remarks

The response of fiber-reinforced polymer composite (FRP)/metal lap strap joints made with different FRP adherends and stacking sequences, subjected to various numbers of thermal cycles and the subsequent monolithic tensile load, was experimentally and numerically studied. The influences of several parameters that could affect the performance of the joints (i.e., composite adherends' properties, stacking sequence, and thermal cycles), were investigated. For the

numerical simulation, appropriate mesh density was established using a mesh convergence study. The results can be summarized as follows:

i. Stacking sequence had a significant effect on the stress distribution within the adhesive and at the adhesive/adherend interfaces.

ii. In joints with carbon-epoxy adherend, the maximum values of peel and shear stresses were observed in the adhesive of the joints having unidirectional FRP adherends. However, while the peel stress was maximum in joints with unidirectional glass-epoxy adherends, the maximum value of shear stress was observed in the joint with $[22]_{10}$ glass-epoxy adherend.

iii. Comparatively, it appears that joints with carbon-epoxy adherends would outperform joints with equivalent glass-epoxy adherends when subjected to high thermal cycling (i.e., harsh environment). This is attributed to the overall stiffness of the joint, and reduction in the resulting eccentric loading when the cycled joints were subjected to the subsequent tensile loading.

iv. It was demonstrated that once a unidirectional ply is included adjacent to the adhesive with any of the layups tried in the study, the addition of the ply helped to reduce the resulting peel and shear stresses significantly. Therefore, it is strongly recommended to include the above remedy when fabricating joints with angle-ply adherends.

Chapter 6 Influence of Graphene Nanoplatelets (GNPs) on Mode I Fracture Toughness of an Epoxy Adhesive under Thermal Fatigue

6.1 Introduction

As stated earlier, the ever-growing applications of ABJs in different structural elements have encouraged the development and use of new materials and technologies to ensure their durability and safe performance (He, 2011). Enhancement of ABJs' strength and performance, especially when they are intended for use under harsh environmental loading conditions, has absorbed considerable attention in recent years. A large number of research articles have shown that inclusion of nanoparticles into a polymeric matrix could enhance the strength, stiffness and the fracture toughness of the ABJs that are made by the resulting reinforced matrix (adhesive). Several new materials and techniques have been developed, and are currently being worked on, and nanoparticle-reinforced adhesives are some of the most notable developments in recent years. Various aspects of nano-reinforced adhesives, such as the type of nanoparticles and their properties, their dispersion methods, functionalization and cost, must all be taken into consideration for a given application (Domun et al., 2015). Various types of nanoparticles such as carbon nanotubes (CNTs), carbon nanofibers (CNFs), GNPs, graphene nanosheets (GNSs), nanoclays and nanosilicas, are some examples that have been incorporated into adhesives in an attempt to improve their mechanical properties and performance (Bernardo et al., 2016; Kamar et al., 2015; Manjunatha et al., 2015; Shadlou et al., 2014).

GNPs are a relatively new class of carbon nanoparticles, with multifunctional properties (Geim and Novoselov, 2007). The superior characteristics of GNPs in comparison to other nanocarbon particles (such as their large aspect ratio and lower cost), have rendered them as effective reinforcing agents for various types of adhesives. Graphene is formed by a flat monolayer of carbon atoms, tightly packed into a two dimensional (2D) honeycomb lattice, and is a basic building block for graphitic materials of all other dimensionalities (Geim and Novoselov, 2007;

Geng et al., 2009; Yasmin and Daniel, 2004). Unlike most carbon nanoparticles, GNPs have large aspect ratios, with thickness of approximately 1 nm and lateral dimensions varying from 25 nm to a micron.

When considering the improvement in the fracture toughness of resins, if one compares two adhesives that host the same weight content of CNTs and GNPs, one would find that the latter provides more significant degree of enhancement (Ahmadi-Moghadam et al., 2015; Ahmadi-Moghadam and Taheri, 2014b). Billaudeau (2010) found that the GNPs' level of enhancement in fracture toughness was approximately twice that gained by CNTs. The more superior enhancement gained by using GNPs as reinforcing agents in comparison to CNTs has also been reported in several research articles (see for instance, Ahmadi-Moghadam et al., 2015; Ahmadi-Moghadam and Taheri, 2014b; Billaudeau, 2010; Geng et al., 2009; Shokrieh et al., 2014; Yasmin and Daniel, 2004).

The lower cost of natural graphite enables mass production of graphene in comparison to CNT production has rendered GNPs as more attractive candidates for next-generation applications (Geng et al., 2009). It has also been demonstrated that inclusion of GNPs in epoxy could produce more improvement in both strength and fracture toughness properties when compared with their graphene nanosheet counterparts (Shokrieh et al., 2014). From the loading perspectives, ABJs are known to be susceptible to cyclic thermal loading (Abdel Wahab, 2012; Banea and da Silva, 2009; Yu et al., 1993). When a solid is restrained such that it cannot expand or contract freely, any temperature change within it would cause internal deformation, and consequently, stresses. This phenomenon becomes further exacerbated if the temperature of the solid fluctuates repeatedly.

As briefly stated earlier, thermal cycling, as a source of damage in material systems, has been reported as one of the significant causes of failure in a wide variety of structural elements (e.g., in solder joints, thermal barrier films, ABJs, bridge decks, large storage tanks, and oil and gas pipelines). The resulting phenomenon is often referred to as "thermal fatigue". When a body undergoes thermal fatigue, it would also experience mechanical strains. These strains may be purely elastic, or could extend into the plastic regime (Carden, 1963). Therefore, it is worthwhile

to investigate whether the inclusion of relatively inexpensive GNPs within adhesives that are used to form ABJs that become subjected to thermal fatigue, may indeed relieve some of the imposed strains/stresses. This is one of the objectives of this part of the study. In addition, accurate simulation of the response of such ABJs subject to such a combined and complex loading state, that is, the combination of thermal fatigue and mechanical loading would be a desirable outcome.

As demonstrated in a previous section of this dissertation, the CZM technique can be effectively used to simulate the response of ABJs. This chapter will briefly outline the application of the CZM technique (which was explained in detail in an earlier chapter) to model the response of GNP reinforced ABJs subjected to the combined loading stated earlier. A few researchers have incorporated the finite element method to better understand the effect of GNPs on CZM parameters, and to develop the appropriate relationship that could be used to adjust the parameters used in CZM as a function of nanoparticle weight content (Borowski et al., 2015; Jia and Yan, 2014; Jiang, 2010; Safaei et al., 2015).

Therefore, the two main objectives of the work presented in this chapter are: (i) to investigate the influence of GNP weight content on Mode I interlaminar fracture toughness of the host epoxy resin/adhesive, so as to establish the optimum GNP content and (ii) to examine the integrity and feasibility of a relatively simple CZ finite element framework in characterizing the performance of ABJs formed by the GNP-reinforced adhesives subject to thermal fatigue and subsequent mechanical loading. In doing so, DCB specimens were fabricated using unidirectional E-glass-epoxy adherends, bonded together by the same widely-used room-cured epoxy resin introduced earlier, reinforced with four different weight percentages of GNPs (i.e. 0.0 wt%, 0.25 wt%, 0.5 wt% and 1 wt%). These specimens were subjected first to various numbers of thermal cycles, and subsequently were tested under Mode I fracture monotonic loading. Moreover, the response of the specimens was simulated by CZM using the ABAQUS FE code. The same linear elastic/linear softening (bilinear) CZM that was introduced earlier, which is relatively the simplest and most commonly used model, will be used in this investigation.

6.2 Experimental Investigation

Details of the experimental investigation undertaken to establish the optimum weight content of GNP in adhesive subject to thermal fatigue will be explained in this section. Moreover, values of the parameters required for the computational modelling of ABJs response using the CZM will also be established. Appropriate size DCB specimens are fabricated and tested. The related details are discussed next.

6.2.1 Preparation of GNP-reinforced adhesive

GNPs (GNP-M-25) with average diameter, D, of 25 μm, thickness, t, of 7 nm, and surface area of 100 m^2/g were acquired from XG Science Ltd. (Lansing, MI, USA); see Figure 6-1 and Table 6-1 (see also appendix C for more details). The uniform dispersion of the nanoparticles within the adhesive is the key to achieve the desired mechanical properties.

(a)   (b)
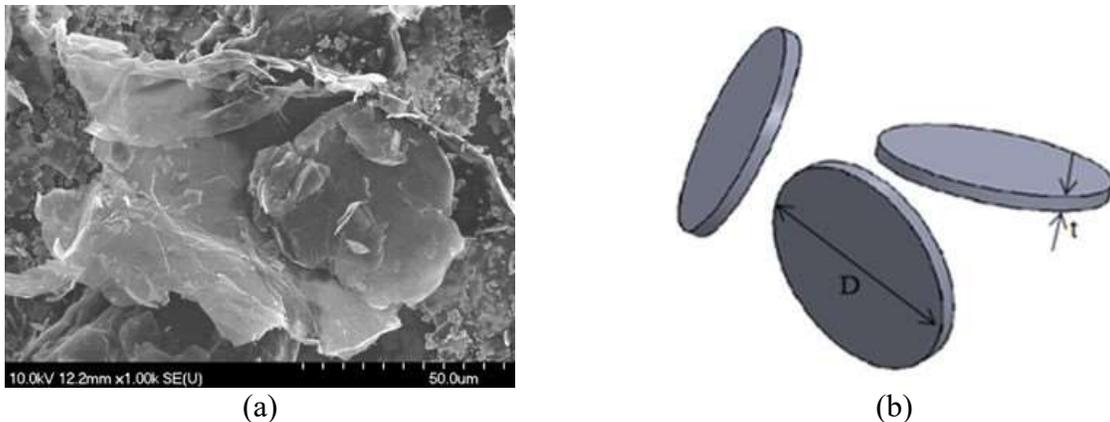
Figure 6-1 X-GnP-25 (a) SEM image; (b) schematic of the idealized GNP (Ahmadi-Moghadam and Taheri, 2014a)

Table 6-1 Characteristics of the bulk GNP powder ("www.xgsciences.com," 2017)

Appearance	Black granules
Bulk Density	0.03-0.1 g/cc
Oxygen Content	< 1%
Residual Acid Content	< 0.5 wt%
Thermal Expansion (CTE)	4.6×10^{-6}
Tensile Strength (GPa)	5
Tensile Modulus (GPa)	1,000

The following procedure, which was demonstrated to be very effective by other researchers (Ahmadi-Moghadam et al., 2015; Ahmadi-Moghadam and Taheri, 2014a; Soltannia et al., 2013b; Soltannia and Taheri, 2015), was used for uniformly dispersing GNPs into resin. First, the appropriate amount of GNP was weighed (i.e., 0.25%, 0.5% and 1.0%), and added to the West System 105 resin. This mixture was stirred using a mechanical stirrer, starting with slow speed of 40 rpm for 2 min, then 400 for 4 min, and finally 2000 rpm for 10 to 15 minutes. In the next step, a three-roll mill machine (Torrey Hill Technology, San Diego, CA) was used. The procedure started with carefully cleaning the machine and setting the rollers gap at 40 μm using a feeler gauge. The GNP/resin slurry was then slowly poured over the feed-roller of the three-roll mill (see Figure 6-2(a)) to calender the mixture (see Figure 6-2(b)). This procedure was repeated seven times as per (Ahmadi-Moghadam and Taheri, 2014a). Then, West System 206 hardener was added to the final mixture, and the new mixture was stirred at a speed of 400 rpm for 3 minutes. The entrapped air from the slurry was removed by a vibration technique, applied for five minutes. At this stage, the mixture would be ready for using to bond the two adherends of the DCBs.

| (a) | (b) | (c) |
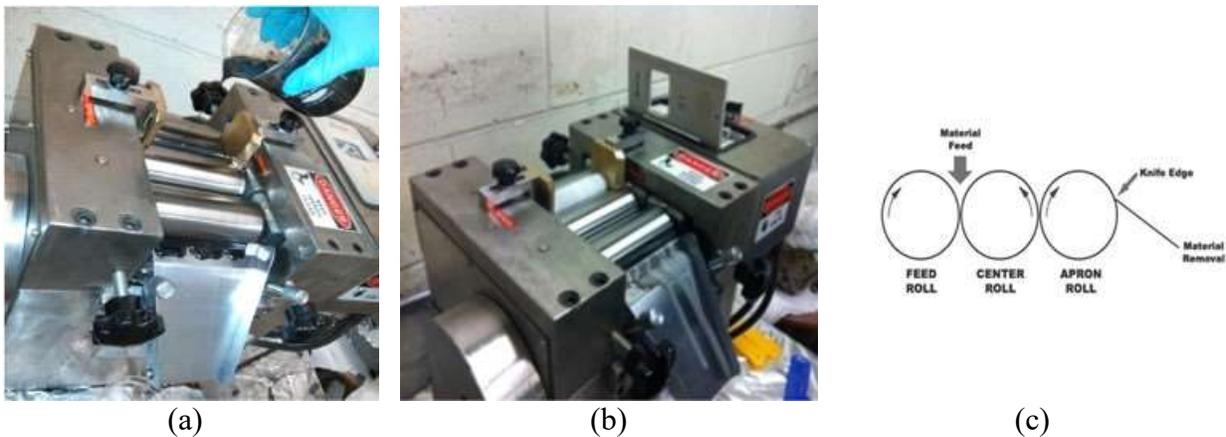
Figure 6-2 (a) and (b) The three-roll mill machine and (c) schematics of its operational mechanism (Soltannia and Taheri, 2013a)

The GNP reinforced-adhesive was used to prepare DCB specimens made using unidirectional glass-epoxy adherends and following the same procedure explained in sub-section 3.3.2.

6.2.2 Cyclic thermal fatigue test

The specimens were subjected to a series of thermal cycles, following the procedure and regime described in sub-section 3.4.4. Details of a heating/cooling cycle and the computer traced image of a 24 h period thermal cycling is shown in Figure 6-3. The specimen-groups identifications are tabulated in Table 6-2.

Table 6-2 Identification of specimen groups that were subjected to various numbers of thermal cycles

Group ID	1	2	3	4	5
Number of thermal cycles	zero (baseline specimens)	300	600	900	1000

Note: Each group has four sub-groups, identified by %wt GNP content (i.e., 0.0%, 0.25%, 0.5% and 1%, respectively.)
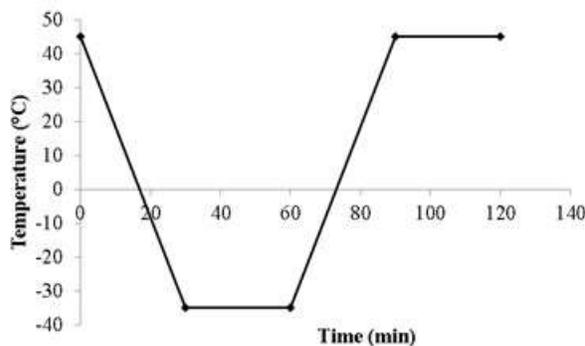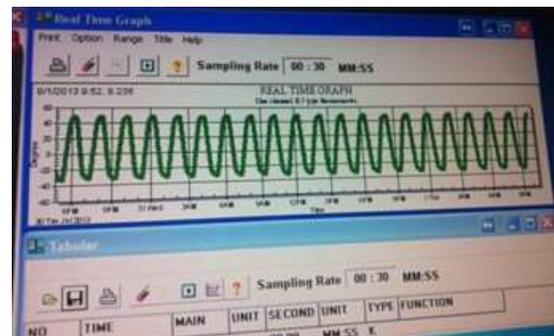
(a)   (b)

Figure 6-4 (a) details of a heating/cooling cycle and (b) computer traced image of a 24 h period thermal cycling

A total of four specimens were tested per specimen sub-group in order to investigate the influence of GNP weight percentages and thermal fatigue on fracture toughness Mode I in DCB. Therefore, in total, 20 groups of specimens were tested, consisting of five different thermal cycle regimes (as noted in Table 6-2), with four different GNP weight percentages (i.e. 0.0%, 0.25%, 0.5% and 1%).

113

6.3 Experimental results

6.3.1 Evaluation of Mode I fracture toughness

As mentioned in Chapter 3, various methods are available to establish an adhesive's fracture energy, G_{IC}, from the data obtained through the DCB test. Here, the MCC method is used for the evaluation (ASTM D5528, 2007). The equation for evaluating G_{IC} is represented by:

$$G_I = \frac{3P^2C^{2/3}}{2A_1 b\, h} \qquad\qquad 6\text{-}1$$

where P is the load corresponding to the defined crack length, C is the compliance, A_1 is the slope of the line on the least-square plot of the crack length (normalized by specimen thickness), as a function of the cube root of the compliance, b and h are specimen's width and thickness, respectively.

6.3.2 Effect of GNPs weight percentages on Mode I fracture toughness

Figure 6-4 shows the load–deflection curve of DCB specimens having different GNPs weight percentages, having been subjected to 0, 300, 600, 1000 and thermal cycles, respectively. Note that each curve (and bar of the bar-chart shown in the subsequent figures) represents the average values of a minimum of three tests in each group. The results presented in Figure 6-4 indicate that resin containing 0.5 wt% GNP produced the optimum performance in comparison to the other specimens.

The average results from each group of DCB tests were also used to establish Mode-I fracture toughness of each group. The results are illustrated in Figure 6-5. As can be seen, thermal fatigue affects the fracture toughness of the ABJs. Moreover, regardless of the amount of GNP content in the resin, the fracture energy values of the GNP reinforced specimens were enhanced in comparison with the baseline group. However, 0.5 wt% GNP content produced the greatest enhancement in reducing the effect of thermal fatigue on the ABJs. Interestingly, the degradation

in the toughness decreases after a certain number of thermal fatigue (here, after 600 thermal cycles). This trend corroborates with the observations of other researchers (see, for instance, Shen et al. (2013); Shokrieh et al. (2014)).
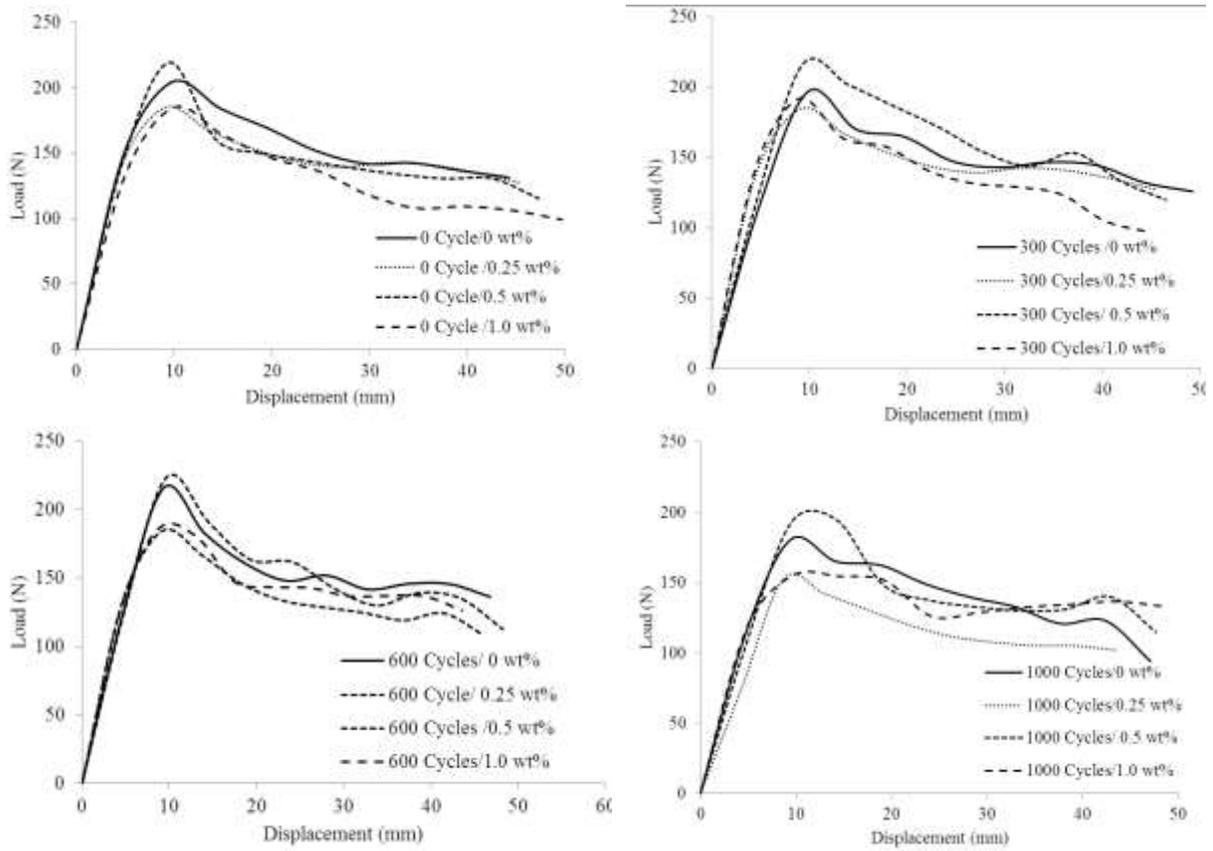
Figure 6-5 Comparison of load–deflection curves of DCB containing various %wt GNP, subjected to thermal cyclic loads
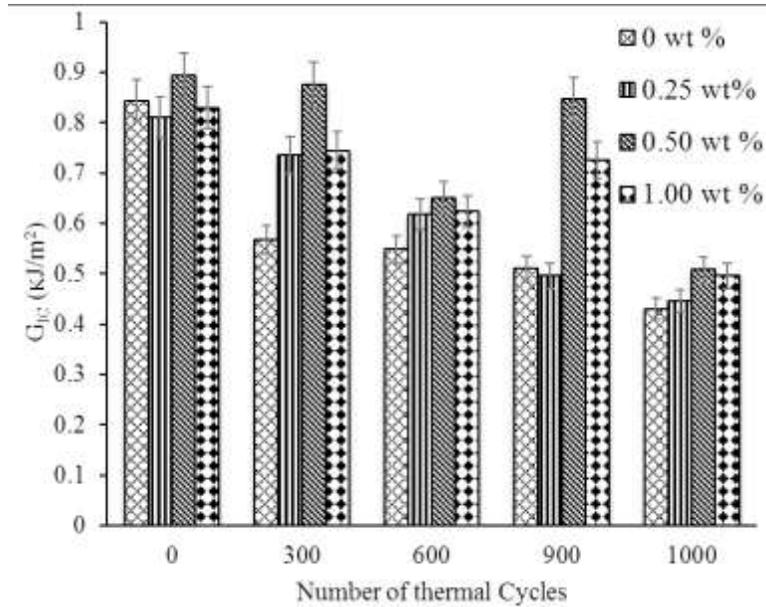
Figure 6-6 Degradation of the critical energy release rate as a function of applied thermal cycles and different GNPs weight percentages

6.3.3 Effect of thermal fatigue

The effect of thermal fatigue is examined by comparison of the results produced by testing of the baseline specimens and the group whose adhesive gained most enhancement because of inclusion of GNPs (i.e., the group with its adhesive containing 0.5 wt% GNP). Some of the curves illustrated in Figure 6-4 are repeated in Figure 6-6 to highlight the influence of GNPs on curtailing the degradation caused by the thermal cycles. In this figure the degradation caused by the maximum number of thermal cycles are seen on the baseline specimens and those reinforced with 0.5 wt% GNP. As can be seen, the enhancing influence of GNPs can be clearly seen on the thermally cycled and non-cycled specimens. Moreover, as the crack-mouth opening becomes greater, the GNP reinforced adhesive performs more favorably than that noted in the baseline specimen, especially when subjected to thermal fatigue.

116

<center>(a)   (b)</center>
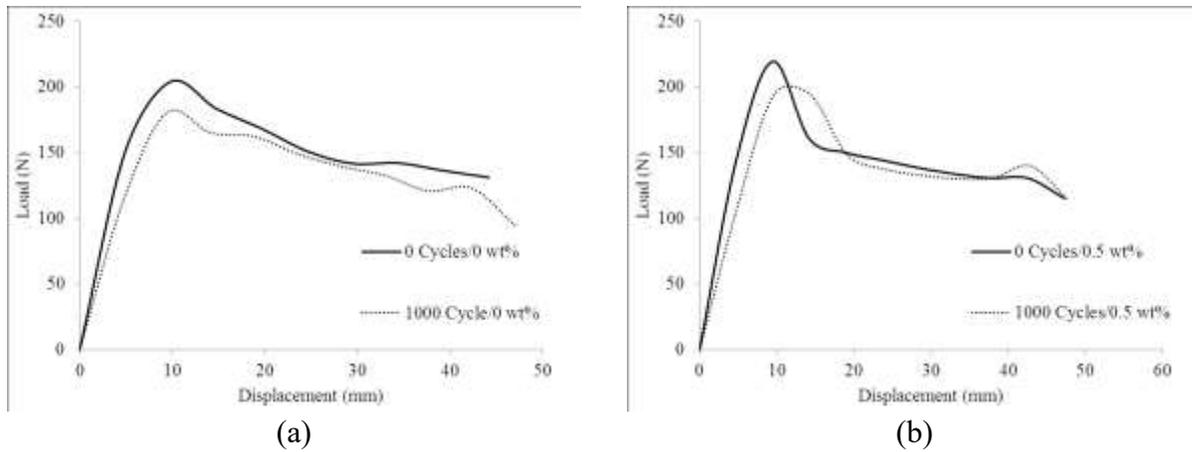
<center>Figure 6-7 Influence of thermal fatigue on the performance of (a) the baseline group and (b)
the group containing 0.5 wt % GNP</center>

6.4 Finite Element Modelling

The objective of this portion of the effort is to determine whether the performance of the GNP reinforced adhesive could be captured by incorporation of the same effective computational framework introduced earlier. Obviously, the successful outcome of such an endeavor would be very practical and useful, in that one could employ the same framework to assess performance of actual bonded structural assemblies (especially those with complex shapes), in a cost-effective and reliable manner. The material properties used in modeling the reinforced joints are reported in Table 6-3.

6.4.1 FE model and input parameters

As described in the earlier trial, ABAQUS (2014) was used to conduct the numerical modelling and capture the response of the GNP-DCB specimens subjected to the cyclic thermal loading scenarios described above. Several two-dimensional (2D) plane strain FE models were constructed to investigate the parameters that influence the fracture response of GNP-DCB specimens. The material properties of the adherend and adhesive are reported in Table 6-3.

<center>117</center>

Table 6-3 Material properties of the adherends and adhesive

Material	Modulus of elasticity (GPa)		Poisson's Ratio		Shear Modulus (GPa)		Thermal expansion coefficient (10^{-6}/ °C)		Layer thickness (mm)
	E_1	$E_2=E_3$	$v_{12}=v_{13}$	v_{23}	$G_{12}=G_{13}$	G_{23}	α_1	$\alpha_2=\alpha_3$	t
E-glass/epoxy adherends	50	15.2	0.254	0.428	4.7	3.28	6.34	23.3	0.125
Epoxy adhesive	3.5		0.35		0.4		85		0.2
GNPs	1000		0.4				4.6		N/A

Notes: the subscripts refer to the local axis used to identify fiber orientation →1- runs along the fibers, 2- runs orthogonal to the fibers, 3- runs through-the-thickness

To conduct an efficient analysis and conserve CPU time, a 2D plane-strain finite element model of the DCB was constructed, as shown in Figure 6-7, since the crack tips on either side of the DCB specimens propagated in equal lengths during the tests. Specifically, ABAQUS' 2D four-node bilinear plane strain quadrilateral element with reduced integration and hourglass options (CPE4R) was used for modelling the adherends. The adhesive portion of the specimen was modeled with a series of four-node cohesive (COH2D4) elements. It should be noted that a convergence analysis was performed by varying the mesh density, and comparing the results, until similar results were obtained between two consecutive FE runs with varying refined meshes. A vertical displacement of 10 mm was applied at the node corresponding to the location where the load/displacement was applied to the actual specimen during each test. This displacement induces Mode I opening type fracture.
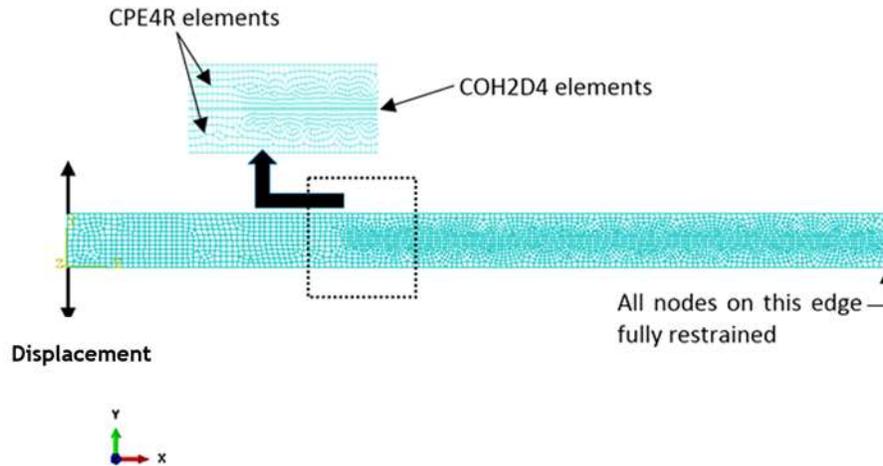
Figure 6-8 The plane-strain mesh configuration and boundary conditions for DCB model

6.4.2 CZM model used and evaluation of its parameters

As explained in Chapter 4, the traction-separation curve (damage initiation and evolution) used in the CZM requires three important parameters that affect the accuracy of the results. These parameters are the stiffness, strength and the fracture energy of the adhesive. Previous experimental investigations conducted by our research group (Ahmadi-Moghadam and Taheri, 2014b; Soltannia and Taheri, 2015) revealed significant increases in the epoxy resins modulus of elasticity, shear strength and toughness as a result of inclusion of an optimal amount of GNP (i.e., 0.5 wt%). Therefore, these properties should be adjusted when nanoparticles are used. The mechanical properties of the adhesive used in our study, obtained experimentally, are reported in Table 6-4.

The damage variable values used in the analysis were established using a simple equation, based on the assumption that the resin's degradation as a function of the thermal cycle follows a relatively linear trend. Although the experimental values reported for 900 thermal cycles violates the said trend (see Figure 6-5), from the practicality perspective, and as the results of the analyses will illustrate, the assumption is admissible. The simple function was obtained by conducting a least-square fit of the experimentally evaluated critical strain energy release rate data, relating the

degradation level, *D,* to the applied thermal cycles, *N,* as noted in Equation 3-5. Please note that this equation is admissible to the case of neat epoxy.

Table 6-4 Summary of the values of CZM parameters calibrated for the neat and GNP-reinforced West System epoxy

Material	Penalty stiffness normal (shear) N/mm³	Tripping traction normal (shear) MPa	Mode-I (mode-II) fracture energy, G_I or G_{II} (kJ/m²)	Initiation criterion	Propagation criterion
Neat epoxy	3500 (1500)	59 (23)	1.5 (2)	Maximum nominal stress	Power Law (with η=2)
Epoxy (0.5 wt% GNP)	3700 (1650)	65 (30)	3 (2.5)		

6.4.3 Numerical results

Comparison of the experimental and numerical results for the DCB specimens is shown in Figure 6-8. The figures show the variation of crack-mouth opening displacement (noted simply as 'displacement' in the Figure) as a function the applied load. As seen, good agreement is seen between the experimental and numerically predicted results. This approach can therefore be used to establish the performance of ABJs formed by mating complex-shaped adherend by neat adhesive or adhesives reinforced by GNPs.

(a)   (b)
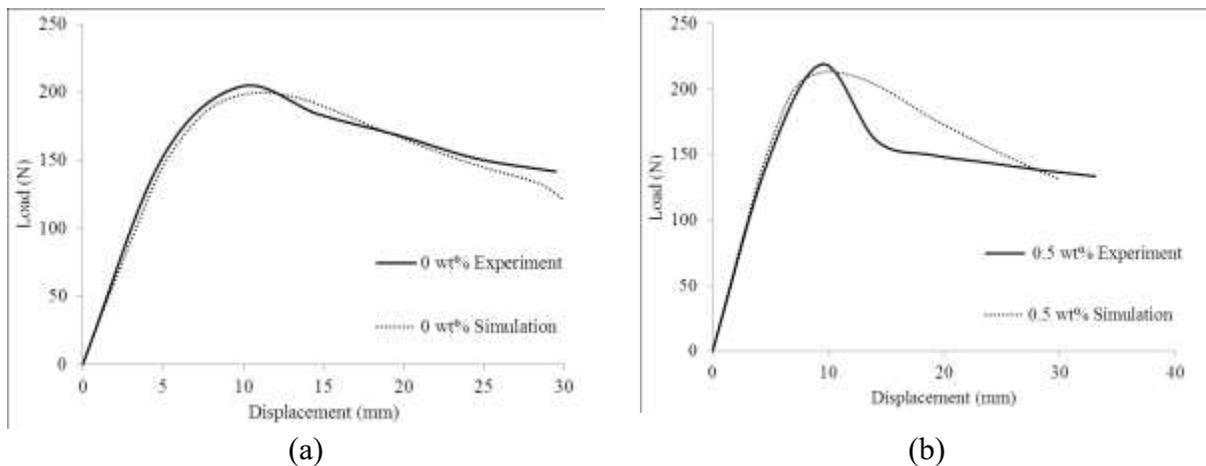
Figure 6-9 Comparison of the experimental and FE simulation results for the joints made with (a) neat resin and (b) 0.5 wt% GNP reinforced resin (not thermally cycled)

6.5 Investigation of the Fracture and Failure Mechanisms

To gain further insight into the influence of GNP and thermal fatigue on the response of the adhesive, the resulting fracture and failure mechanisms within each group of specimens were carefully examined by two techniques. These techniques are: (i) optical microscopy, and (ii) scanning electronic microscopy (SEM).

6.5.1 Optical microscopic evaluation

The failure modes in ABJs were categorized and explained in sub-section 3.5.3. The baseline specimens (i.e., joined with neat epoxy) considered in this part of the study mainly failed in the interfacial mode. Often this failure mode is attributed to inferior surface preparation; however, a careful and standard procedure was followed to prepare the bonding surfaces (i.e., as explained in more detail earlier, the surfaces were grit blasted, followed by removal of dust particles with compressed air). Therefore, it is strongly believed that the mismatches in the mechanical properties of the substrate and those of the adhesive (especially, mismatches in the Poisson's ratios and coefficient of thermal expansions) were the primary cause of the interfacial mode of failure. This hypothesis will be further supported by considering the failure mode of GNP-reinforced specimens.

The failure mode observed in the majority of the specimens formed with GNP-reinforced adhesives was, in contrast, primarily the intralayer type, and only a few specimens experienced interface failure mode. It should be noted that even those specimens that experienced intralayer failure mode, their fracture was initiated cohesively (i.e., within the adhesive); however, after a certain amount of propagation, the fracture diverted into one of the adherend (more specifically, into the first resin layer next to fiber-layers that were in direct contact with the adhesive). This type of fracture is clearly seen in Figure 6-9. Interestingly, those that were not thermally cycled or were subjected to low thermal cycles had relatively unblemished and smooth damaged facture surfaces (see Figure 6-9(a)), while those subjected to high numbers of thermal cycles had much rougher fracture surfaces (see Figure 6-9(c)). These observations were made using a microscope with 50X magnification. It is therefore postulated that the addition of GNPs, which toughened the adhesive,

prevented the crack to grow within the adhesive; instead, it was directed into the weaker (non-GNP reinforced) resin layer, which had weakened due to the applied thermal cycles.

(a) No thermal cycles   (b) After 300 cycles   (c) After 900 cycles
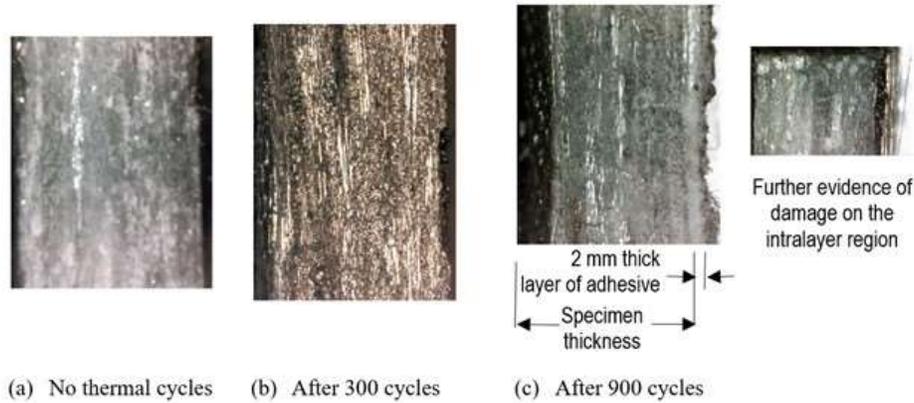
Figure 6-10 Influence of thermal fatigue on the fracture morphology (pictures illustrate the side-view of specimens at location of failure near the initiation front and fracture plane)

The extent of failure and observed resin destruction is due to the degradation of the resin itself resulting from the applied thermal cycles; the degradation was also further aggravated by the mismatches in Poisson's ratios of the GNPs, adhesive and composite substrates.

6.5.2 Scanning electron microscopy (SEM)

Figure 6-11 shows the SEM images of the failed surfaces of the baseline and GNP-reinforced specimen at virgin and final thermal fatigue states. SEM images show a higher resolution of the failure surfaces' topography in comparison to the images illustrated by SOM in the previous figure. Comparison of the failure surfaces of the baseline virgin specimens exhibits relatively smooth surfaces for the virgin baseline specimens, while the baseline specimens that underwent thermal fatigue exhibited rougher surfaces. The failure surfaces of the GNP-reinforced adhesives, whether they had been subjected to thermal cycles or not, are not significantly different. This would indicate that the GNP-reinforced adhesive could better endure the thermal cycles. This is also evidence when considering Figure 6-6 (a) and Figure 6-6 (b). One can see from Figure 6-6 (b) that the curves

are almost similar, indicating that the thermal fatigue was less influential than those exhibited by the curves for the neat adhesive specimens, as shown in Figure 6-6 (a).
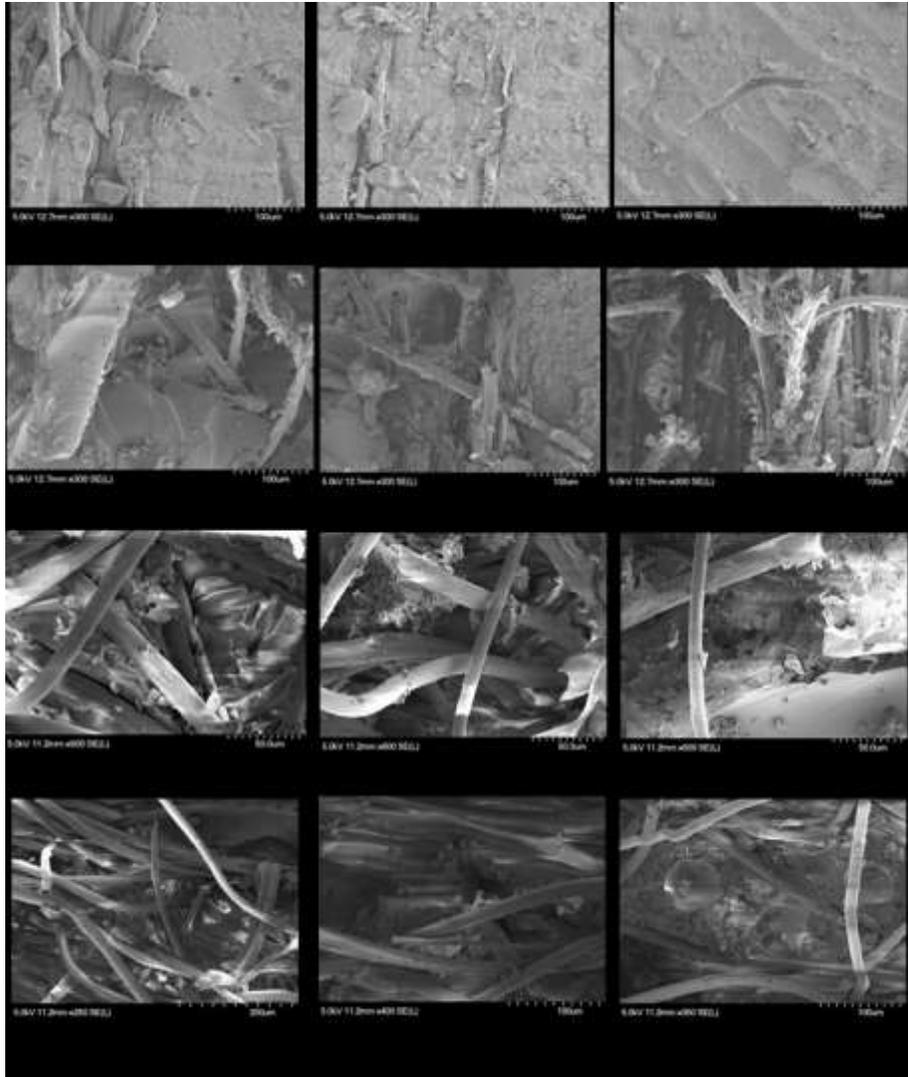
Figure 6-11 SEM images of the fracture surfaces of specimens bonded with the neat epoxy and those with GNP-reinforced adhesive at virgin and final thermal fatigue states
(Note: The scale of images on the third row is slightly different from the other images)

6.6 Concluding Remarks

In this chapter, the influence of thermal cycles on the performance of ABJs, whose adhesive was reinforced with GNPs, was investigated by testing DCB specimens. The influence of GNPs as an economical and effective agent for reinforcing adhesives and enhancing their fracture properties

under the aforementioned condition was examined. The specimens were assembled with a commonly used room-cured epoxy resin (adhesive), in the neat form, as well as having the same adhesive reinforced with four different weight percentages of GNPs (0.25 wt%, 0.5 wt% and 1 wt%). Mode I fracture toughness of the baseline DCB specimens formed by unidirectional glass-epoxy adherends, subject to monotonic loading, were first examined experimentally. The remaining specimens were subjected to various numbers of thermal cycles, and their Mode I fracture toughness values were evaluated after completion of thermal cycles. The resulting degradation of the adhesive's properties as a function of the applied thermal loading cycles was established. The following conclusions are drawn based on the works conducted:

i. The experimental results evidenced a gradual degradation of the bonded region as a function of the applied thermal cycles. Thermal cycling also affected the stiffness and strength of the ABJs.

ii. A transition in the failure mode from cohesive to interfacial failure mechanisms was observed in the neat and reinforced specimens that underwent thermal fatigue, respectively.

iii. The feasibility of simulating the performance of GNP-reinforced joints using the finite element method in conjunction with the CZ modeling technique was established. It was concluded that the adopted numerical framework could be used to analyze the performance of complexly shaped adhesively bonded assemblies subject to thermal loading in a reliable and cost-effective manner.

iv. It was observed that GNPs could enhance the performance of joints that become subjected to thermal fatigue in an economical and effective manner. The maximum enhancement was achieved at 0.5 wt% GNP content. It was also noted that after a certain number of thermal cycles, degradation due to thermal cycles was subsided; however, upon additional thermal cycles, the degradation was resumed.

v. The optical and scanning electron microscopies revealed the positive influence of the GNPs. Much rougher fracture surfaces and some evidence of resin annihilations were

observed on specimens that were subjected a high number of thermal cycles fatigue, especially in those joints that were formed with the neat epoxy.

Chapter 7 Conclusions and Recommendations

7.1 Summary

In this thesis, the response (specifically, the degradation) of dissimilar composite/metallic ABJs subjected to thermal fatigue was investigated by the continuum and FM approaches. Both experimental and numerical approaches were incorporated. The experimental investigation characterized the response of a commonly used epoxy resin that was subjected to various degrees of thermal fatigue and characterized the resin's post-fatigue response under mechanical loading. In addition, the fracture behavior of the thermally fatigued adhesive was also systematically evaluated by characterizing its Mode I, Mode II and mixed mode fracture responses. Furthermore, the mechanical response of ABJs, subjected to thermal fatigue and mechanical loading was also studies. The integrity and reliability of the CZ computational approach for predicting the response of ABJs subject to such complex loading scenarios were also examined and established. Moreover, a coupled experimental and computational optimization analysis was carried out to establish the influence of two material-related parameters that affect the generation of stresses in ABJs. Finally, an attempt was made to improve performance of ABJs that undergo thermal fatigue by addition of relatively inexpensive GNPs.

7.2 Outcomes and Conclusions

The specific outcomes of the investigations are summarized as follows:

i. Thermal cycles were observed to cause a notable degradation in the stiffness and strength of the epoxy resin. The modulus of elasticity and ultimate tensile strength of the resin were degraded by approximately 17% and 8%, respectively, after exposure to 1000 thermal cycles.

ii. While a resin's properties are not supposed to significantly impact the axial strength and stiffness of the unidirectional fiber-reinforced composites that are formed by the resin, that was not the case in this investigation. In fact, mechanical test results revealed degradation levels of 12% and 13%, respectively, in the modulus of elasticity and ultimate tensile

strength of the unidirectional epoxy specimens that were investigated in this study. Interestingly, from the perspective of the effect on the ultimate strain, the FRP was observed to initially show decreased ultimate strain as the number of thermal cycles were increased (up to 300 cycles); however, after that, the ultimate strain increased (by as much as 25%), leading to a significantly softened response as the thermal cycles increased.

iii. The FT-Raman spectra obtained from the resin specimens that were exposed to various numbers of thermal cycles showed similar characteristics. An in-depth investigation conducted on some of the specimens that were tested under various isothermal regimes showed a variation in the intensity of the Raman spectra at lower thermal cycles; however, the intensity in resin specimens that were exposed to 600 and greater numbers of thermal cycles leveled off.

iv. A maximum change in the T_g of 9% was observed in the resin as a result of the applied thermal cycling. The change in T_g as a function of applied thermal cycles was in concert with the observed variation in the stiffness and strength of the resin.

v. The resulting degradation in the resin's fracture toughness as a function of the applied thermal cycles was observed to follow a linear trend. Therefore, a simple equation can be used to estimate the degradation in fracture toughness of such epoxy resins as a function of applied thermal cycles.

vi. The resulting thermal degradation affected the crack propagation path created as a result of the applied mechanical loading. In other words, the initial crack, which started propagating in a cohesive manner, altered its path in joints whose adhesive was degraded by the thermal cycles. As the number of applied thermal cycles increased (i.e., resin degradation increased), the crack further changed its course and, in some cases, traveled into the adjacent plies, since the resin forming the adherends plies was also degraded as a result of thermal fatigue.

vii. Degradation of the resin led to fiber pull-out and fiber-breakage in the ABJs that were first thermally cycled and subsequently subjected to mechanical loading. At times, total disintegration of the resin was also observed through microscope evaluation.

127

viii. The resulting degradation in Mode-I fracture toughness as a function of applied thermal cycles was observed to follow a linear trend. This allowed development of a simple equation that could be conveniently used to establish the degradation in fracture toughness of such epoxy resins.

ix. Similar to the resin's Mode I fracture response, its Mode II fracture toughness was also observed to degrade with a more or less linear variation as function of the applied cycles. However, the mixed-mode fracture toughness degradation started at a relatively slower pace in specimens that were subjected up to 300 cycles. The degradation then followed a linear trend in those specimens that were subject to a greater number of thermal cycles (up to 750 cycles). The degradation trend remained relatively unchanged in specimens that had undergone greater than 750 thermal cycles.

x. The computational strategy, using the CZ modeling technique, proved to be an effective method for assessing the effect of thermal degradation and subsequent mechanical loading on ABJs. It was demonstrated that by using the simplest form of cohesive models (i.e., the bilinear model), one could produce results with an acceptable accuracy and optimal CPU consumption. The finite element simulation results indicated that the incorporated modeling strategy could be used to predict the performance of geometrically complexly configured ABJs subject to various loading conditions with a reasonable degree of confidence.

xi. Stacking sequence had a significant effect on the stress distributions within the adhesive and adhesive/adherend interfaces. In joints with carbon-epoxy adherend, the maximum values of peel and shear stresses were observed in the adhesive of the joints having unidirectional FRP adherends. However, while the peel stress was maximum in joints with unidirectional glass-epoxy adherend, the maximum value of shear stress was observed in the joint with glass-epoxy adherend with 22° fiber orientation.

Comparatively, it was observed that joints with carbon-epoxy adherends would outperform the performance of joints with equivalent glass-epoxy adherends when subjected to high thermal cycling (i.e., harsh environment). This is attributed to the overall stiffness of the

joint, and reduction in the resulting non-concentric loading when the cycled joints were subjected to the subsequent tensile loading.

xii.   It was demonstrated that once a unidirectional ply is included adjacent to the adhesive with any of the layups tried in the study, the addition of the ply helped to reduce the resulting peel and shear stresses significantly. Therefore, it is strongly recommended to include the above remedy when fabricating joints with angle-ply adherends.

7.3 Recommendations for Future Work

The study presented in this thesis highlighted the influence of thermal fatigue on an epoxy resin/adhesive and ABJs formed by such adhesive. However, this was a first step in gaining a better understanding of the performance of epoxy resins under thermal fatigue. It should be noted that ABJs are used to mate various materials, and when considering FRP, various layups sequences are often used to form the adherends. Moreover, often ABJs become subjected to a multiplicity of harsh environments (e.g., combined moisture and thermal cycles). Therefore, the study presented here begins an important step to what should be followed up in the future.

The following sections present some recommendations regarding some of the issues that should be investigated in the future.

7.3.1 Experimental related suggestions:

i.   In the present study, the FRP adherends were made of unidirectional FRP. It was demonstrated numerically that ply orientation had a critical influence on increasing or relieving stresses in ABJs. Therefore, an experimental study should be carried out to characterize the response of joints made with some of the configurations used in our numerical analysis.

ii.   In real world ABJs are usually subject to some degree of restrain. The restrain would amplify the creation of thermally induced stresses in such joints significantly. As a result, the effect of any degradation resulting from application of thermal cycles would become

much more prevalent if restrained ABJs are subjected to thermal cycles. Therefore, it is strongly recommended to conduct a similar investigation in which the response of restrained joints subject to thermal cycles is explored.

iii. Several industries (e.g., boat and pleasure-craft builders) use the same epoxy that is used in forming their various primary and secondary structural components for mating them to one another (e.g., decks to bullheads). However, other industries (i.e., aerospace and automotive), seldom use the same resin that is used for rendering the structural components for bonding them to one another. Therefore, a similar study should be carried out to assess the effect of thermal fatigue on adhesives that are specifically made for mating structural components (i.e., different from the one used to form the adherends). In this way, not only could one monitor the performance of structural adhesives, but at the same time, one could assess the effect of thermal cycles on the resin used to form the adherends, which would be different from that of the adhesive.

iv. Long-term exposure of ABJs to some of the more commonly faced harsh environments (i.e., combined moisture and constant and variable amplitude thermal cycles) should be considered and investigated.

v. Investigation into the effect of stacking sequences on thermally cycled ABJ undergoing various loading rates would be of great value to industrial applications.

vi. Identification of a non-destructive testing (NDT) approach for monitoring the strength and stiffness degradation of ABJs while undergoing thermal fatigue would be of utmost importance.

vii. The above investigation would provide adequate data and framework for generating practical empirical or semi-empirical equations by which practicing engineers would be able to predict the resulting degradation in the service life of ABJs under thermal fatigue.

viii. The future research works should also investigate the effect of cyclic thermal loading on different configurations of ABJs, specifically a joint configuration that would explore the

effect of thermal cycles on the long-term performance of composite patch repaired structural systems in a more direct fashion.

ix.   Investigation into the interfacial properties. Also, consider the change in viscoelastic response under thermal cycling.

x.   Finally, experimental investigation tailored using the design of experiments approach, incorporating a greater number of specimens should be contemplated.

7.3.2 Simulation related suggestions

i.   The experimental results and observations revealed that one of the critical outcomes of the thermal fatigue was diverting the direction of a crack that had initiated cohesively (i.e., within the adhesive layer) in the ABJs into the adjacent FRP adherend's plies. The robust CZ modeling approach incorporated in our study is incapable of tracing a crack that changes its paths. However, the use of the extended finite element method (XFEM), a sophisticated numerical approach that has been gaining significant popularity in recent years could theoretically model such a crack diversion. Therefore, a comprehensive numerical analysis of the ABJs with XFEM is warranted.

ii.   The numerical analysis conducted in the study did not account for the potential damage that could occur within the FRP substrate during thermal cycling and the subsequent mechanical loading. More accurate analysis could be conducted by incorporating an appropriate damage mechanism that could account for the potential damage in the FRP adherends.

iii.   One could also take account of the viscoelastic response and nonlinear behavior of the adhesives by selecting and incorporating appropriate models into the finite element framework.

References

ABAQUS. (2014). Users Manual. Retrieved from Version 6.14 Users Manual. Simulia, RI, USA.

Abdel Wahab, M. M. (2012). Fatigue in adhesively bonded joints: a review. *ISRN Materials Science*, *2012*.

Adams, R. D. (2005). *Adhesive bonding: science, technology and applications*. CRC press. Boca Raton, FL, USA.

Ahmadi-Moghadam, B., Sharafimasooleh, M., Shadlou, S. and Taheri, F. (2015). Effect of functionalization of graphene nanoplatelets on the mechanical response of graphene/epoxy composites. *Materials & Design*, *66*, 142–149.

Ahmadi-Moghadam, B. and Taheri, F. (2014a). Effect of processing parameters on the structure and multi-functional performance of epoxy/GNP-nanocomposites. *Journal of Materials Science*, *49(*18*)*, 6180–6190.

Ahmadi-Moghadam, B. and Taheri, F. (2014b). Fracture and toughening mechanisms of GNP-based nanocomposites in modes I and II fracture. *Engineering Fracture Mechanics*, *131*, 329–339.

Ajiboye, G. I. (2012). *Industrially relevant epoxy-acrylate hybrid resin photopolymerizations*. Master thesis, Department of Chemical and Biochemical Engeneering. The University of Iowa, Iowa city, USA.

Alfano, G. (2006). On the influence of the shape of the interface law on the application of cohesive-zone models. *Composites Science and Technology*, *66*(6), 723–730.

Alfano, M., Furgiuele, F., Leonardi, A., Maletta, C. and Paulino, G. H. (2007). Fracture analysis of adhesive joints using intrinsic cohesive zone models. In *Convegno IGF XIX Milano, Italy,*

2-4 July 2007.

Alfano, M., Furgiuele, F., Leonardi, A., Maletta, C. and Paulino, G. H. (2009). Mode I fracture of adhesive joints using tailored cohesive zone models. *International Journal of Fracture*, *157*(1), 193–204.

Al-Ramahi, N. (2018). Numerical stress analysis in hybrid adhesive joint with non-linear materials. Doctoral thesis, Department of Engineering Sciences and Mathematics University of Technology Luleå, Sweden.

Anderson, T. L. (2017). *Fracture mechanics: fundamentals and applications*. CRC press. Boca Raton, FL, USA.

Ashcroft, I. A., Casas-Rodriguez, J. P. and Silberschmidt, V. V. (2008). Mixed-mode crack growth in bonded composite joints under standard and impact-fatigue loading. *Journal of Materials Science*, *43*(20), 6704–6713.

Ashcroft, I. A., Shenoy, V., Critchlow, G. W. and Crocombe, A. D. (2010). A comparison of the prediction of fatigue damage and crack growth in adhesively bonded joints using fracture mechanics and damage mechanics progressive damage methods. *The Journal of Adhesion*, *86*(12), 1203–1230.

Ashcroft, I. A., Wahab, M. M. A., Crocombe, A. D., Hughes, D. J. and Shaw, S. J. (2001). The effect of environment on the fatigue of bonded composite joints. Part 1: testing and fractography. *Composites Part A: Applied Science and Manufacturing*, *32*(1), 45–58.

ASTM D5528. (2007). *Test Method for mode I Interlaminar Fracture Toughness of Unidirectional Fiber-Reinforced Polymer Matrix Composites*. Annual Book of ASTM Standards, Vol. 15.03, ASTM International, W. Conshohocken, Philadelphia, USA.

ASTM, D638-14. (2014). *Standard Test Method for Tensile Properties of Plastics*. Vol. 08.01, ASTM International, West Conshohocken, Pennsylvania, USA. 1–17.

ASTM E1356-08. (2014). *Standard Test Method for Assignment of the Glass Transition Temperatures by Differential Scanning Calorimetry*. Vol. 14.05, ASTM International, West Conshohocken, Pennsylvania, USA. 1–4.

Azevedo, J. C. S., Campilho, R., da Silva, F. J. G., Faneco, T. M. S. and Lopes, R. M. (2015). Cohesive law estimation of adhesive joints in mode II condition. *Theoretical and Applied Fracture Mechanics*, *80*, 143–154.

Baftechi, S. (2008). Effect of thermal loading on metal/fiber-reinforced composite interface. *Master's thesis, Department of Civil and Resouce Engineering. Dalhousie University, Halifax, NS, Canada*.

Banea, M. D. and da Silva, L. F. M. (2009). Adhesively bonded joints in composite materials: an overview. *Proceedings of the Institution of Mechanical Engineers, Part L: Journal of Materials: Design and Applications*, *223*(1), 1–18.

Banea, M. D., da Silva, L. F. M. and Campilho, R. (2012). Mode II fracture toughness of adhesively bonded joints as a function of temperature: experimental and numerical study. *The Journal of Adhesion*, *88*(4–6), 534–551.

Banea, M. D., Da Silva, L. F. M. and Campilho, R. (2011). Mode I fracture toughness of adhesively bonded joints as a function of temperature: experimental and numerical study. *International Journal of Adhesion and Adhesives*, *31*(5), 273–279.

Barbosa, A. Q., da Silva, L. F. M. and Öchsner, A. (2015). Hygrothermal aging of an adhesive reinforced with microparticles of cork. *Journal of Adhesion Science and Technology*, *29*(16),

1714–1732.

Barenblatt, G. I. (1962). The mathematical theory of equilibrium cracks in brittle fracture. *Advances in Applied Mechanics*, *7*, 55–129.

Bascom, W. D. and Cottington, R. L. (1976). Effect of temperature on the adhesive fracture behavior of an elastomer-epoxy resin. *The Journal of Adhesion*, *7*(4), 333–346.

Benzeggagh, M. L. and Kenane, M. (1996). Measurement of mixed-mode delamination fracture toughness of unidirectional glass/epoxy composites with mixed-mode bending apparatus. *Composites Science and Technology*, *56*(4), 439–449.

Bernardo, L. F. A., Amaro, A. P. B. M., Pinto, D. G. and Lopes, S. M. R. (2016). Modeling and simulation techniques for polymer nanoparticle composites–a review. *Computational Materials Science*, *118*, 32–46.

Billaudeau, E. (2010). Mechanical behavior of polyurea nanocomposites doped with nanoparticles. Doctoral Dissertation, Civil Engineering Department, Columbia University, New York, USA.

Borowski, E., Soliman, E., Kandil, U. F. and Taha, M. R. (2015). Interlaminar fracture toughness of CFRP laminates incorporating multi-walled carbon nanotubes. *Polymers*, *7*(6), 1020–1045.

Broughton, W. R. and Mera, R. D. (1997). Review of life prediction methodology and adhesive joint design and analysis software. *National Physical Laboratory Report CMMT (A)*, *62,* 1-33.

Broughton, W. R., Mera, R. D. and Hinopoulos, G. (1999). Cyclic fatigue testing of adhesive

joints: environmental effects. *National Physical Laboratory Report CMMT (A)*, *192*, 1–18.

Brussat, T. R., Chiu, S. T. and Mostovoy, S. (1977). *Fracture mechanics for structural adhesive bonds*. Technical Report-77-163, Lockheed-California Corporation, Burbank, CA, USA.

Butkus, L. M. (1997). *Environmental durability of adhesively bonded joints*. Air Force Inst of Tech Wright-Patterson AFB OH.

Cabral-Fonseca, S., Correia, J. R., Rodrigues, M. P. and Branco, F. A. (2012). Artificial accelerated ageing of GFRP pultruded profiles made of polyester and vinylester resins: characterisation of physical–chemical and mechanical damage. *Strain*, *48*(2), 162–173.

Carden, A. E. (1963). *Thermal fatigue-an analysis of the experimental method*. Oak Ridge National Lab, TN, USA.

Campilho, R. D. (2017). Strength Prediction of Adhesively-bonded Joints. CRC press. Boca Raton, FL, USA.

Crawford, A., Silva, E., York, K. and Li, C. (n.d.). Raman spectroscopy: a comprehensive review. *Department of Textile Engineering, Chemistry and Science, North Carolina State University, Raliegh, NC, USA*.

Da Silva, L. F. M. and Adams, R. D. (2005). Measurement of the mechanical properties of structural adhesives in tension and shear over a wide range of temperatures. *Journal of Adhesion Science and Technology*, *19*(2), 109–141.

da Silva, L. F. M., Öchsner, A. and Adams, R. D. (2011). *Handbook of adhesion technology*. Springer Science & Business Media. Heidelberg, Germany.

De Moura, M. (2008). Interlaminar mode II fracture characterization.. *Delamination Behavior of Composites*, A volume in *Woodhead Publishing Series in Composites Science and Engineering*. 310–325. Woodhead Publishing, Sawston, Cambridge. UK.

De Moura, M., Dourado, N., Morais, J. J. L. and Pereira, F. A. M. (2011). Numerical analysis of the ENF and ELS tests applied to mode II fracture characterization of cortical bone tissue. *Fatigue & Fracture of Engineering Materials & Structures*, *34*(3), 149–158.

de Moura, M. and Gonçalves, J. P. M. (2014). Development of a cohesive zone model for fatigue/fracture characterization of composite bonded joints under mode II loading. *International Journal of Adhesion and Adhesives*, *54*, 224–230.

de Moura, M., Gonçalves, J. P. M. and Fernandez, M. V. (2016). Fatigue/fracture characterization of composite bonded joints under mode I, mode II and mixed-mode I+ II. *Composite Structures*, *139*, 62–67.

Dillard, D. A. (2010). *Advances in structural adhesive bonding*. CRC press. Boca Raton, FL, USA.

Dogan, A. and Atas, C. (2016). Variation of the mechanical properties of E-glass/epoxy composites subjected to hygrothermal aging. *Journal of Composite Materials*, *50*(5), 637–646.

Domun, N., Hadavinia, H., Zhang, T., Sainsbury, T., Liaghat, G. H. and Vahid, S. (2015). Improving the fracture toughness and the strength of epoxy using nanomaterials–a review of the current status. *Nanoscale*, *7*(23), 10294–10329.

Du, Z.-Z., Wang, J. and Fan, X. (2006). Direct cyclic method for solder joint reliability analysis. In *ASME 2006 International Mechanical Engineering Congress and Exposition* (229–233). American Society of Mechanical Engineers. Chicago, IL, USA, November 5-10, 2006

Dugdale, D. S. (1960). Yielding of steel sheets containing slits. *Journal of the Mechanics and Physics of Solids*, *8*(2), 100–104.

Duncan, B. (2010). *Developments in testing adhesive joints. In Advances in Structural Adhesive Bonding* (pp. 389-436). A volume in Woodhead Publishing Series in Welding and Other Joining Technologies. Woodhead Publishing, Cambridge. UK.

Dunn, D. J. (2003). *Adhesives and sealants: technology, applications and markets*. iSmithers Rapra Publishing. Shropshire, UK.

Elices, M., Guinea, G. V, Gomez, J. and Planas, J. (2002). The cohesive zone model: advantages, limitations and challenges. *Engineering Fracture Mechanics*, *69*(2), 137–163.

Eslami, S., Taheri-Behrooz, F. and Taheri, F. (2012). Effects of aging temperature on moisture absorption of perforated GFRP. *Advances in Materials Science and Engineering* Volume 2012, Article ID 303014, 7 pages. Hindawi Publishing Corporation, Cairo, Egypt.

Fares, M. E., Youssif, Y. G. and Alamir, A. E. (2004). Design and control optimization of composite laminated truncated conical shells for minimum dynamic response including transverse shear deformation. *Composite Structures*, *64*(2), 139–150.

Fares, M. E., Youssif, Y. G. and Hafiz, M. A. (2004). Structural and control optimization for maximum thermal buckling and minimum dynamic response of composite laminated plates. *International Journal of Solids and Structures*, *41*(3), 1005–1019.

Fares, M. E., Youssif, Y. G. and Hafiz, M. A. (2005). Multiobjective design and control optimization for minimum thermal postbuckling dynamic response and maximum buckling temperature of composite laminates. *Structural and Multidisciplinary Optimization*, *30*(2), 89–100.

Farquharson, S., Bassilakis, R., DiTaranto, M. B., Haigis, J. R., Smith, W. W., Solomon, P. R. and Wallace, J. F. (1994). Measurement of thermal degradation in epoxy composites by Fourier transform Raman spectroscopy. In Proceedings of SPIE. The International Society for Optical Engineering, 2072, 319–332.

Fiedler, B., Hobbiebrunken, T., Hojo, M. and Schulte, K. (2005). Influence of stress state and temperature on the strength of epoxy resins. In *Proceedings of the 11th International Conference on Fracture (ICF 11)*. Turin, Italy. 20-25 March 2005. (2271–2275).

Foulc, M. P., Bergeret, A., Ferry, L., Ienny, P. and Crespy, A. (2005). Study of hygrothermal ageing of glass fibre reinforced PET composites. *Polymer Degradation and Stability*, *89*(3), 461–470.

Geim, A. K. and Novoselov, K. S. (2007). The rise of graphene. *Nature Materials*, *6*(3), 183-191.

Geng, Y., Wang, S. J. and Kim, J.-K. (2009). Preparation of graphite nanoplatelets and graphene sheets. *Journal of Colloid and Interface Science*, *336*(2), 592–598.

Ghiasi, H., Fayazbakhsh, K., Pasini, D. and Lessard, L. (2010). Optimum stacking sequence design of composite materials Part II: Variable stiffness design. *Composite Structures*, *93*(1), 1–13.

Ghiasi, H., Pasini, D. and Lessard, L. (2009). Optimum stacking sequence design of composite materials Part I: Constant stiffness design. *Composite Structures*, *90*(1), 1–11.

Ghomshei, M. M. M. and Mahmoudi, A. (2010). Thermal buckling analysis of cross-ply laminated rectangular plates under nonuniform temperature distribution: A differential quadrature approach. *Journal of Mechanical Science and Technology*, *24*(12), 2519–2527.

Ghugal, Y. M. and Kulkarni, S. K. (2013). Thermal response of symmetric cross-ply laminated

plates subjected to linear and non-linear thermo-mechanical loads. *Journal of Thermal Stresses*, *36*(5), 466–479.

Grammatikos, S. A., Evernden, M., Mitchels, J., Zafari, B., Mottram, J. T. and Papanicolaou, G. C. (2016). On the response to hygrothermal aging of pultruded FRPs used in the civil engineering sector. *Materials & Design*, *96*, 283–295.

Grammatikos, S. A., Jones, R. G., Evernden, M. and Correia, J. R. (2016). Thermal cycling effects on the durability of a pultruded GFRP material for off-shore civil engineering structures. *Composite Structures*, *153*, 297–310.

Grohs, J. W. (2007). Comparing In Situ and Bulk Constitutive Properties of a Structural Adhesive. Master thesis, Department of Mechanical Engineering, Blacksburg, VA, USA.

Gürdal, Z., Haftka, R. T. and Hajela, P. (1999). *Design and optimization of laminated composite materials*. John Wiley & Sons. Toronto, Canada.

Gutwinski, M. and Schäuble, R. (2009). The effect of thermal cyclic loading on CFRP foam core sandwich structures. In Proceedings of *International Conference on Material and Component Performance under Variable Amplitude Loading*. Darmstadt/Germany. 23-26 March 2009. 815–821.

Haftka, R. T. and Gürdal, Z. (1992). *Elements of structural optimization* (Vol. 11). Third Revised and Expanded Edition. Kluwer Academic Publishers, Dordrecht, the Netherlands.

Halford, G. R. and Manson, S. S. (1976). Thermal Fatigue of Materials and Components, ASTM STP 612. *Spera and D. Mowbray, Eds*, 239–254. ASTM International, W. Conshohocken, Philadelphia, USA.

Han, X., Crocombe, A. D., Anwar, S. N. R. and Hu, P. (2014). The strength prediction of adhesive single lap joints exposed to long term loading in a hostile environment. *International Journal of Adhesion and Adhesives*, *55*, 1–11.

Hancox, N. L. (1998). Thermal effects on polymer matrix composites: Part 1. Thermal cycling. *Materials & Design*, *19*(3), 85–91.

Hardis, R., Jessop, J. L. P., Peters, F. E. and Kessler, M. R. (2013). *Cure kinetics characterization and monitoring of an epoxy resin using DSC, Raman spectroscopy, and DEA*. Composites Part A: Applied Science and Manufacturing. 49, 100-108.

Hawileh, R. A., Abu-Obeidah, A., Abdalla, J. A. and Al-Tamimi, A. (2015). Temperature effect on the mechanical properties of carbon, glass and carbon–glass FRP laminates. *Construction and Building Materials*, *75*, 342–348.

He, X. (2011). A review of finite element analysis of adhesively bonded joints. *International Journal of Adhesion and Adhesives*, *31*(4), 248–264.

Herakovich, C. T. (1981). On the relationship between engineering properties and delamination of composite materials. *Journal of Composite Materials*, *15*(4), 336–348.

Heshmati, M. (2017). Durability and Long-term Performance of Adhesively Bonded FRP/steel Joints. Doctoral Thesis, Department of Civil and Environmental Engineering Division of Structural Engineering Steel and Timber Structures, Chalmers University of Technology, Gothenburg, Sweden.

Hillerborg, A. (1991). Application of the fictitious crack model to different types of materials. In *Current Trends in Concrete Fracture Research*. Springer. Netherlands. 51(2),95–102.

Hillerborg, A., Modéer, M. and Petersson, P.-E. (1976). Analysis of crack formation and crack growth in concrete by means of fracture mechanics and finite elements. *Cement and Concrete Research*, *6*(6), 773–781.

Hu, P., Han, X., Da Silva, L. F. M. and Li, W. D. (2013). Strength prediction of adhesively bonded joints under cyclic thermal loading using a cohesive zone model. *International Journal of Adhesion and Adhesives*, *41*, 6–15.

Humfeld Jr, G. R. (1997). Mechanical behavior of adhesive joints subjected to thermal cycling. Master's thesis, Department of Engineering Mechanics, Virginia Polytechnic Institute and State University, Blacksburg, Virginia, USA.

Ishai, O., Krishnamachari, S. and Broutman, L. J. (1988). Structural design optimization of composite laminates. *Journal of Reinforced Plastics and Composites*, *7*(5), 459–474.

Jia, Y. Y. and Yan, W. Y. (2014). Numerical modeling of graphene/polymer interfacial behaviour using peel test. In the proceedings of 11th International Fatigue Congress, At Melbourne, Australia, Volume: 891-892, 1119–1124.

Jiang, H. (2010). Cohesive zone model for carbon nanotube adhesive simulation and fracture/fatigue crack growth. Doctoral Thesis, Mechanical Engineering, University of Akron, OH, USA.

Johnson, W. S. and Butkus, L. M. (1998). Considering environmental conditions in the design of bonded structures: a fracture mechanics approach. *Fatigue & Fracture of Engineering Materials & Structures*, *21*(4), 465–478.

Kamar, N. T., Hossain, M. M., Khomenko, A., Haq, M., Drzal, L. T. and Loos, A. (2015). Interlaminar reinforcement of glass fiber/epoxy composites with graphene nanoplatelets.

Composites Part A: Applied Science and Manufacturing, *70*, 82–92.

Kenane, M. and Benzeggagh, M. L. (1997). Mixed-mode delamination fracture toughness of unidirectional glass/epoxy composites under fatigue loading. *Composites Science and Technology*, *57*(5), 597–605.

Khoramishad, H., Crocombe, A. D., Katnam, K. B. and Ashcroft, I. A. (2010). Predicting fatigue damage in adhesively bonded joints using a cohesive zone model. *International Journal of Fatigue*, *32*(7), 1146–1158.

Khoramishad, H., Hamzenejad, M. and Ashofteh, R. S. (2016). Characterizing cohesive zone model using a mixed-mode direct method. *Engineering Fracture Mechanics*, *153*, 175–189.

Kumar, B. G., Singh, R. P. and Nakamura, T. (2002). Degradation of carbon fiber-reinforced epoxy composites by ultraviolet radiation and condensation. *Journal of Composite Materials*, *36*(24), 2713–2733.

Lee, D. G. and Suh, N. P. (2005). Axiomatic design and fabrication of composite structures-applications in robots, machine tools, and automobiles. Oxford University Press. Inc,New Yourk, USA.

Lee, M. J., Cho, T. M., Kim, W. S., Lee, B. C. and Lee, J. J. (2010). Determination of cohesive parameters for a mixed-mode cohesive zone model. *International Journal of Adhesion and Adhesives*, *30*(5), 322–328.

Lekhnitskii Sergei, G. (1963). *Theory of elasticity of an anisotropic elastic body*. Holden-Day, San Francisco, CA, USA.

Li, S., Thouless, M. D., Waas, A. M., Schroeder, J. A. and Zavattieri, P. D. (2005a). Use of a

cohesive-zone model to analyze the fracture of a fiber-reinforced polymer–matrix composite. *Composites Science and Technology*, *65*(3), 537–549.

Li, S., Thouless, M. D., Waas, A. M., Schroeder, J. A. and Zavattieri, P. D. (2005b). Use of mode-I cohesive-zone models to describe the fracture of an adhesively-bonded polymer-matrix composite. *Composites Science and Technology*, *65*(2), 281–293.

Liljedahl, C. D. M., Crocombe, A. D., Wahab, M. A. and Ashcroft, I. A. (2007). Modelling the environmental degradation of adhesively bonded aluminium and composite joints using a CZM approach. *International Journal of Adhesion and Adhesives*, *27*(6), 505–518.

Maitournam, H., Pommier, B., Comte, F. and Nguyen-Tajan, T. M.-L. (2010). Direct cyclic methods for structures under thermomechanical loading. In *European Conference on Computational Mechanics (ECCM), Paris, 16-21 May 2010*.

Mallick, P. K. (2007). *Fiber-reinforced composites: materials, manufacturing, and design*. CRC press. Boca Raton, FL, USA.

Manjunatha, C. M., Chandra, A. R. A. and Jagannathan, N. (2015). Fracture and Fatigue Behavior of Polymer Nanocomposites—A Review. *Journal of the Indian Institute of Science*, *95*(3), 249–266.

Marques, E. A. S., da Silva, L. F. M., Banea, M. D. and Carbas, R. J. C. (2015). Adhesive joints for low-and high-temperature use: an overview. *The Journal of Adhesion*, *91*(7), 556–585.

Mazumdar, S. (2001). *Composites manufacturing: materials, product, and process engineering*. CRC press. Boca Raton, FL, USA.

McCreery, R. L. (2005). *Raman spectroscopy for chemical analysis* (Vol. 225). John Wiley &

Sons. Toronto, Canada.

Mohamed, M. and Taheri, F. (2017). Influence of graphene nanoplatelets (GNPs) on mode I fracture toughness of an epoxy adhesive under thermal fatigue. *Journal of Adhesion Science and Technology*, *31*(19–20), 2105–2123.

Mohamed, M. and Taheri, F. (2018). Fracture response of double cantilever beam subject to thermal fatigue. The Journal of Strain Analysis for Engineering Design, 53(7), 504-516.

Mohamed, M. Johnson, M. and Taheri, F. (2019). On the Thermal Fatigue of a Room-Cured Neat Epoxy and its Composite. Open Journal of Composite Materials (OJCM), Vol.9 No. 2

Nguyen, T. C., Bai, Y., Zhao, X. L., and Al-Mahaidi, R. (2012). Durability of steel/CFRP double strap joints exposed to sea water, cyclic temperature and humidity. Composite Structures, 94(5), 1834-1845.

Ou, Y., Zhu, D., Zhang, H., Huang, L., Yao, Y., Li, G. and Mobasher, B. (2016). Mechanical characterization of the tensile properties of glass fiber and its reinforced polymer (GFRP) composite under varying strain rates and temperatures. *Polymers*, *8*(5), 196.

Raju, T. D. and Kumar, J. S. (2011). Thermal analysis of Composite Laminated Plates using Higher-order shear deformation theory with Zig-Zag Function. International Journal of Science & Emerging Technologies, 2(2), 53–57.

Ray, B. C. and Rathore, D. (2014). Durability and integrity studies of environmentally conditioned interfaces in fibrous polymeric composites: Critical concepts and comments. Advances in colloid and interface science, 209, 68-83.

Safaei, M., Sheidaei, A., Baniassadi, M., Ahzi, S., Mashhadi, M. M. and Pourboghrat, F. (2015).

An interfacial debonding-induced damage model for graphite nanoplatelet polymer composites. *Computational Materials Science*, *96*, 191–199.

Schwalbe, K.-H., Scheider, I. and Cornec, A. (2013). *Guidelines for applying cohesive models to the damage behaviour of engineering materials and structures*. Springer Science & Business Media. New York, USA.

Shadlou, S., Ahmadi-Moghadam, B. and Taheri, F. (2014). Nano-enhanced adhesives. *Reviews of Adhesion and Adhesives*, *2*(3), 371–412.

Shen, M.-Y., Chang, T.-Y., Hsieh, T.-H., Li, Y.-L., Chiang, C.-L., Yang, H. and Yip, M.-C. (2013). Mechanical properties and tensile fatigue of graphene nanoplatelets reinforced polymer nanocomposites. *Journal of Nanomaterials*, January 2013, Article No. 1, 9 pages.

Shokrieh, M. M., Ghoreishi, S. M., Esmkhani, M. and Zhao, Z. (2014). Effects of graphene nanoplatelets and graphene nanosheets on fracture toughness of epoxy nanocomposites. *Fatigue & Fracture of Engineering Materials & Structures*, *37*(10), 1116–1123.

Silberschmidt, V. V. (2016). *Dynamic deformation, damage and fracture in composite materials and structures*. Woodhead Publishing, Sawston, Cambridge. UK.

Soltannia, B. and Taheri, F. (2015). Influence of nano-reinforcement on the mechanical behavior of adhesively bonded single-lap joints subjected to static, quasi-static, and impact loading. *Journal of Adhesion Science and Technology*, *29*(5), 424–442.

Soltannia, B. and Taheri, F. (2013a). Static, quasi-static and high loading rate effects on graphene nano-reinforced adhesively bonded single-lap joints. International Journal of Composite Materials, 3(6), 181-190.

Soltannia, B., Ahmadi-Moghadam, B.and Taheri, F. (2013b). Influence of tensile impact and strain rate on the response of adhesively bonded single lap joints.ICCM19, Montreal, Canada.

Sonmez, F. O. (2017). Optimum design of composite structures: A literature survey (1969–2009). *Journal of Reinforced Plastics and Composites*, *36*(1), 3–39.

Spera, D. A. (1976). *What is Thermal fatigue*. SIP 612, ASTM International, D.A. Sperz and D.F. Mowbray, Eds., American Society for Testing and Materials. West Conshohocken, PA. USA.

Sugiman, S., Crocombe, A. D. and Aschroft, I. A. (2013a). Experimental and numerical investigation of the static response of environmentally aged adhesively bonded joints. *International Journal of Adhesion and Adhesives*, *40*, 224–237.

Sugiman, S., Crocombe, A. D. and Aschroft, I. A. (2013b). Modelling the static response of unaged adhesively bonded structures. *Engineering Fracture Mechanics*, *98*, 296–314.

Sugiman, S., Crocombe, A. D. and Aschroft, I. A. (2013c). The fatigue response of environmentally degraded adhesively bonded aluminium structures. *International Journal of Adhesion and Adhesives*, *41*, 80–91.

Tabiei, A., and Zhang, W. (2018). Composite laminate delamination simulation and experiment: a review of recent development. Applied Mechanics Reviews,70(3), P 030801.

Turon, A., Davila, C. G., Camanho, P. P., and Costa, J. (2007). An engineering solution for mesh size effects in the simulation of delamination using cohesive zone models. *Engineering Fracture Mechanics*, *74*(10), 1665–1682.

Turon T A. (2006). *Simulation of delamination in composites under quasi-static and fatigue loading using cohesive zone models*. Doctoral Thesis, Department of Mechanical

Engineering, Universitat de Girona, Spain.

Vašková, H., and Křesálek, V. (2011). Raman spectroscopy of epoxy resin crosslinking. In *13th WSEAS International Conference on Automation Control, Modeling & Simulation (ACMOS'11), Lanzarote, Canary Islands, Spain*, 357–361.

Viana, G., Costa, M., Banea, M. D., & da Silva, L. F. M. (2017). Moisture and temperature degradation of double cantilever beam adhesive joints. *Journal of Adhesion Science and Technology*, *31*(16), 1824–1838.

Viana, G., Costa, M., Banea, M. D., and Da Silva, L. F. M. (2017). Behaviour of environmentally degraded epoxy adhesives as a function of temperature. *The Journal of Adhesion*, *93*(1–2), 95–112.

Wahab, M. A. (2015). *Joining Composites with Adhesives: Theory and Applications*. DEStech Publications, Inc. Pennsylvania, USA

Wahab, M. M. A., Ashcroft, I. A., Crocombe, A. D., Hughes, D. J., & Shaw, S. J. (2001). The effect of environment on the fatigue of bonded composite joints. Part 2: fatigue threshold prediction. *Composites Part A: Applied Science and Manufacturing*, *32*(1), 59–69.

Wang, Y., and Williams, J. G. (1992). Corrections for mode II fracture toughness specimens of composites materials. *Composites Science and Technology*, *43*(3), 251–256.

Wicaksono, S., and Chai, G. B. (2013). A review of advances in fatigue and life prediction of fiber-reinforced composites. Proceedings of the Institution of Mechanical Engineers, Part L: Journal of Materials: Design and Applications, 227(3), 179-195.

www.DPNA International. (2017), retrival June 2018.

www.theadhesivesexpert.com. (2018), retrival June 2018.

www.xgsciences.com. (2017), retrival June 2018.

Xie, D., and Waas, A. M. (2006). Discrete cohesive zone model for mixed-mode fracture using finite element analysis. *Engineering Fracture Mechanics*, *73*(13), 1783–1796.

Yang, Q. D., Shim, D. J., & Spearing, S. M. (2004). A cohesive zone model for low cycle fatigue life prediction of solder joints. *Microelectronic Engineering*, *75*(1), 85–95.

Yasmin, A., and Daniel, I. M. (2004). Mechanical and thermal properties of graphite platelet/epoxy composites. *Polymer*, *45*(24), 8211–8219.

Yu, Q., Shiratori, M., and Mori, T. (1993). Nonsteady thermal stress analysis and thermal fatigue strength of metal-CFRP bonded joints. *JSME International Journal. Ser. A, Mechanics and Material Engineering*, *36*(1), 43–49.

Appendices

Appendix A: Copyright Permission Letter for Chapter 6

Dear Sir/Madam

I am the first author of the following paper, while I was working toward my Ph.D. degree. Now, I am preparing my Ph.D. thesis for submission to the Faculty of Graduate Studies at Dalhousie University, Halifax, Nova Scotia, Canada.

I am seeking your permission to include a manuscript version of the following paper in the thesis: Mohamed, M., and Taheri, F. (2017). Influence of graphene nanoplatelets (GNPs) on mode I fracture toughness of an epoxy adhesive under thermal fatigue. Journal of Adhesion Science and Technology, *31*(19–20), 2105–2123. https://doi.org/10.1080/01694243.2016.1264659.

Full publication details and a copy of this permission letter will be included in the thesis.
Best Regards,
Mbarka Mohamed

Thank you for your email.

As an author of the original article you have the right to include the Accepted Manuscript in a thesis or dissertator that is not to be published commercially, provided that publication is acknowledged using the following text:

This is an Accepted Manuscript of an article (Influence of graphene nanoplatelets (GNPs) on mode I fracture toughness of an epoxy adhesive under thermal fatigue) published by Taylor and Francis in Journal of Adhesion Science and Technology on 2017, 31(19–20), 2105–2123, available online: https://doi.org/10.1080/01694243.2016.1264659.

Best wishes,
Sherry Howard
On behalf of Author Services

Appendix B: Copyright Permission Letter for a part of Chapter 4

Dear Sir/Madam

I am the first author of the following paper, while I was working toward my Ph.D. degree. Now, I am preparing my Ph.D. thesis for submission to the Faculty of Graduate Studies at Dalhousie University, Halifax, Nova Scotia, Canada.

I am seeking your permission to include a manuscript version of the following paper in the thesis: Mohamed, M. and Taheri, F. (2018). Fracture response of double cantilever beam subject to thermal fatigue. The Journal of Strain Analysis for Engineering Design, 53(7), 504-516.

Full publication details and a copy of this permission letter will be included in the thesis.

Best Regards,

Mbarka Mohamed

Thank you for your email. I am pleased to report we can grant your request without a fee as part of your thesis.

Please accept this email as permission for your request as detailed below. Permission is granted for the life of the edition on a non-exclusive basis, in the English language, throughout the world in all formats provided full citation is made to the original SAGE publication.

The permission is subject to approval from any co-authors on the original project. Please note approval excludes any graphs, photos, excerpts, etc. which required permission from a separate copyright holder at the time of publication. If your material includes anything which was not your original work, please contact the rights holder for permission to reuse those items.

Best Wishes,

Craig Myles

on behalf of SAGE Ltd. Permissions Team

Appendix C: Technical data sheet 105 System 105/206) Bay City, MI.

www.westsystem.com

General Description

105/206 Epoxy is used for general coating and bonding applications when extended working and cure time are needed or to provide adequate working time at higher temperatures. 105/206 forms a high-strength, moisture-resistant solid with excellent bonding and barrier coating properties. It will wet out and bond to wood fiber, fiberglass, reinforcing fabrics, foam and other composite materials, and a variety of metals. 105/206 Epoxy can be thickened with WEST SYSTEM fillers to bridge gaps and fill voids and can be sanded and shaped when cured. With roller applications, it has excellent thin-film characteristics, allowing it to flow out and self-level without "fish-eyeing." Multiple coats of 105/206 Epoxy create a superior moisture barrier and a tough, stable base for paints and varnishes. It is formulated without volatile solvents resulting in a very low VOC content. It has a relatively high flash point, no strong solvent odor and does not shrink after curing. It is not intended for clear coating natural finished wood.

Handling Characteristics

Mix ratio by volume (300 Mini Pump ratio) .... 5 parts resin: 1-part hardener
by weight 5.36: 1
Acceptable ratio range by weight .... 4.84: 1 to 6.19 :1
Mix viscosity (at 72°F) ASTM D-2393 .... 725 cps
Pot life (100g at 72°F) .... 20 to 25 minutes
Working time, thin film* .... 90 to 110 minutes
Cure to a solid, thin film* .... 10 to 15 hours
Cure to working strength .... 1 to 4 days
Minimum recommended temperature .... 60°F (16°C)

*Epoxy cures faster at higher temperatures and in thicker applications.

Physical Properties of Cured Epoxy

Specific gravity 1.18
Hardness (Shore D) ASTM D-2240 83
Compression yield ASTM D-695 .... 11,500 psi
Tensile strength ASTM D638 ....7,300 psi

Tensile elongation ASTM D-638 .... 4.5%
Tensile modulus ASTM D-638 .... 4.60E+05psi
Flexural strength ASTM D-790 .... 11,800 psi
Flexural modulus ASTM D-790 ....4.50E+05
Heat deflection temperature ASTM D-648....................................... 123°F
Onset of Tg by DSC .... 126°F
Ultimate Tg .... 139°F

Storage/Shelf Life

Store at room temperature. Keep containers closed to prevent contamination. With proper storage, resin and hardeners should remain usable for many years. After a long storage, verify the metering accuracy of the pumps. Mix a small test batch to assure proper curing. Over time, 105 Resin will thicken slightly and will therefore require extra care when mixing. Repeated freeze/thaw cycles during storage may cause crystallization of 105 Resin. Warm resin to 125°F and stirs to dissolve crystals. Hardener may darken with age, but physical properties are not affected by color. Be aware of a possible color shift if very old and new hardener are used on the same project.

Appendix D: Technical data sheet xGnP® Graphene Nanoplatelets, www.xgsciences.com

xGnP® are ultrathin particles of graphite that can also be thought of as short stacks of graphene sheets made through a proprietary manufacturing process. We produce several grades and sizes with thickness ranging from 1 to 20 nanometers and width ranging from 1 to 50 microns. The unique size and platelet morphology of xGnP® makes these particles especially effective at providing barrier properties, while their pure graphitic composition makes them excellent electrical and thermal conductors. Unlike many other additives, xGnP® can improve mechanical properties such as stiffness, strength, and surface hardness of the matrix material. xGnP® are compatible with almost all polymers and can be an active ingredient in inks or coatings as well as an excellent additive to plastics of all types.

### Available as bulk powder or in dispersions:

- xGnP® bulk dry powder
  - Grade C
  - Grade H
  - Grade M
- xGnP® dispersions
  - Aqueous
  - IPA
  - Organic solvents
  - Resins and custom

Potential applications include:

- Ultracapacitor electrodes
- Anode materials for lithium-ion batteries
- Conductive additive for battery electrodes
- Electrically conductive inks
- Thermally conductive films and coatings
- Additive for lightweight composites
- Films or coatings for EMI shielding
- Substrate for chemical and biochemical sensors
- Barrier material for packaging
- Additive for super-strong concrete
- Additive for metal-matrix composites

xGnP® Grade M Product Characteristics xGnP® Graphene

Nanoplatelets are unique nanoparticles consisting of short stacks of graphene sheets having a platelet shape. Grade M particles have an average thickness of approximately 6 to 8 nanometers and a typical surface area of 120 to 150 m²/g. Grade M is available with average particle diameters of 5, 15 or 25 microns.

Raman Spectroscopy of xGnP® Graphene Nanoplatelets
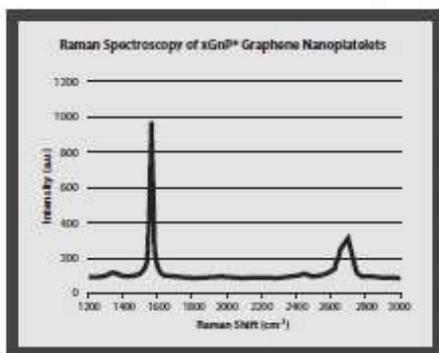
Characteristics of Bulk Powder

Appearance	Black granules
Bulk Density	0.03-0.1 g/cc
Oxygen Content	<1%
Residual Acid Content	<0.5 wt%

	Parallel to Surface	Perpendicular to Surface
Density (g/c³)	2.2	
Carbon Content (%)	>99.5	
Thermal Conductivity (W/mK)	3,000	6
Thermal Expansion (CTE) (m/m/°K)	$4 - 6 \times 10^{6}$	$0.5 - 1.0 \times 10^{6}$
Tensile Modulus (GPa)	1,000	N/A
Tensile Strength (GPa)	5	N/A
Electrical Conductivity (S/m)	10^{7}	10^{2}

155